R91–23

THE IMPLEMENTATION AND VALIDATION OF IMPROVED LANDSURFACE HYDROLOGY IN AN ATMOSPHERIC GENERAL CIRCULATION MODEL

by

Kevin D. Johnson
Dara Entekhabi
and
Peter S. Eagleson

RALPH M. PARSONS LABORATORY

HYDROLOGY AND WATER RESOURCE SYSTEMS

Report Number 334

Prepared under the support of a
National Aeronautics and Space Administration
Grant No. NAG 5–743

The Ralph M. Parsons Laboratory Technical Report Series
is supported in part by a grant from the Ralph M. Parsons Foundation

October 1991

ABSTRACT

New landsurface hydrological parameterizations are implemented into the NASA Goddard Institute for Space Studies (GISS) General Circulation Model (GCM). These parameterizations are: 1) runoff and evapotranspiration functions that include the effects of subgrid scale spatial variability and use physically–based equations of hydrologic flux at the soil surface, and 2) a realistic soil moisture diffusion scheme for the movement of water in the soil column.

A one–dimensional climate model with a complete hydrologic cycle is used to screen the basic sensitivities of the hydrological parameterizations before implementation into the full three–dimensional GCM. Results of the final simulation with the GISS GCM and the new landsurface hydrology indicate that the runoff rate, especially in the tropics, is significantly improved. As a result, the remaining components of the heat and moisture balance show comparable improvements when compared to observations.

The validation of model results is carried from the large global (ocean and landsurface) scale, to the zonal, continental, and finally the finer river basin scales.

(Key words: Climate modeling, Global hydrology)

ACKNOWLEDGMENTS

This work has been supported by the National Aeronautics and Space Administration Grant NAG 5–743. We thank the Climate Group at NASA Goddard Institute for Space Studies for the use of their computational facilities, and Dr. Reto Ruedy for advice and assistance with the computer work. We thank Dr. David Legates for providing surface air temperature data. Finally, we thank Kaye Brubaker and Kelly Hawk of the MIT Ralph M. Parsons Laboratory for their kind assistance with precipitation data analysis.

TABLE OF CONTENTS

Page

Appendix:

LIST OF FIGURES

LIST OF TABLES

Chapter I
Background and Introduction To Model Formulation

A. General Circulation Models

1. Brief Description

The climatic system is exceedingly complex; the interaction of physical processes producing climate cover an enormous range in scale of time and space. The accurate scientific representation of a climate system in full detail is virtually impossible. There is no laboratory in which one may carry out controlled experiments on climate. Furthermore, the sampling density of most key climatic parameters turn out to be, for practical reasons, quite sparse over many climatic regions. Some parameters such as evaporation cannot even be measured directly. Nevertheless the scientific study of climate proceeds in spite of the inherent difficulties.

In light of the controversial threat of global warming, what would most be desired is some means of understanding the effects of changes in the boundary conditions of the climate system. Today, the best analog we have to climate on a global scale, with which we can also perform experiments, is the General Circulation Model (GCM). The following is a very brief and abbreviated description of GCMs. For a fuller treatment, there are several texts available (e.g., Henderson–Sellers and McGuffie, 1987, and Washington and Parkinson, 1986).

The first GCM was pioneered in 1956 by N. A. Phillips. This model had a simple 2–layer atmosphere over the Northern Hemisphere which incorporated quasi–geostrophy and hydrostatic equilibrium. A finite difference scheme solved these equations over a 17 × 16 point gridded area covering 60 million km^2. The model succeeded in producing a jet stream and the 3–celled structure observed in the earth's atmosphere (the Hadley, Ferrel, and polar cells). Since then GCMs have increased in sophistication. Today for instance, numerical solution to the so–called primitive equations (see Table 1.1) has superseded the quasi–geostrophic assumption; the domain has become global instead of hemispheric; detailed radiative transfer schemes have been developed; more realistic boundaries (e.g., topography, albedos, emissivities, etc.) have been added, and atmospheric interactions producing precipitation have been refined. In the late 1960s, S. Manabe pioneered the effort to incorporate a hydrologic cycle. Before this, GCMs were "dry" and the latent heat sources and sinks were parameterized.

There are several GCMs in existence which continue to be improved and refined as new techniques are implemented and as computer capabilities are expanded. Three of the major GCMs in the United States often referenced for their predictions regarding global warming are 1) the National Oceanic and Atmospheric Administrations's (NOAA) Geophysical Fluid Dynamics Laboratory (GFDL) Model in Princeton, NJ, 2) the National Center for Atmospheric Research (NCAR) Community Climate Model (CCM) in Boulder, CO and 3) the National Aeronautic and Space Administration's (NASA) Goddard Institute for Space Studies (GISS) Model in New York, NY. The GISS Model II (i.e., Version II, or 2nd generation, described in Hansen et al., 1983) has been the model used in this research.

For GCMs to be of practical value, they need to be simplified (in terms of the resolution of discretization) in order to meet computational constraints. Thus, typical GCM grid spacing is of the order of hundreds of kilometers to a

Table 1.1 **Fundamental ("Primitive") Equations of the atmosphere used in GCMs (after Hansen et al., 1983). The six unknowns in the atmospheric state vector (ρ, P, T, $\vec{V}$) are numerically solved for, using Equations (T1)–(T6).**

Conservation of Momentum	$\frac{d\vec{V}}{dt} = -2\vec{\Omega} \times \vec{V} - \rho^{-1} \nabla P + \vec{q} + \vec{F}$	(T1,T2,T3)
Conservation of Mass	$\frac{d\rho}{dt} = -\rho\nabla \cdot \vec{V}$	(T4)
Conservation of Energy	$\frac{dU}{dt} = -P \frac{d\rho^{-1}}{dt} + Q$	(T5)
Ideal Gas Law (Equation of State)	$P = \rho RT$	(T6)

where

$\vec{V} = (u_i + u_j + w_k)$	velocity relative to rotating earth
t	time
$\vec{\Omega}$	planet's angular rotation vector
ρ	atmospheric density
$\vec{g}$	apparent gravity [= true gravity $- \vec{\Omega} \times (\vec{\Omega} \times \vec{r})$]
$\vec{r}$	position relative to planet's center
$\vec{F}$	force per unit mass
u	internal energy per unit mass [$= c_v T$]
Q	heating rate per unit mass
R	gas constant
c_v	specific heat at constant volume

grid square side. The grid spacing of the GISS Model II for 8° × 10° grids (it can also be run using 4° × 5° grids) is shown in Fig. 1.1. At this resolution, running time on the IBM mainframe computer requires roughly one hour computing time per simulated month.

GCM grid resolution allows solution of the primitive equations but typically is much too coarse for many of the other important processes. Thus, phenomena such as radiation, moist convection, condensation, cloud formation, boundary layer interaction, and landsurface hydrology must be "parameterized." This term describes the simplification of complex processes to accommodate computational constraints. The simplest of all parameterizations would be to leave out a process altogether. More commonly, a process is represented by simplified empirical relationships having dependence on a greatly reduced number of variables, often only one, as we shall see in the case of current hydrologic parameterizations.

Because of the large amount of simplifications, and the coarse grid spacing, and the lack of understanding of important physical phenomena such as cloud formation, GCMs have been the subject of controversy in scientific circles, particularly in regard to global warming predictions. It has been pointed out (Stone and Risbey, 1990) that a key element critical to the improvement of GCMs continues to be the development of reliable subgrid scale parameterizations. The goal of this work is to show the vast improvements in the GISS landsurface hydrology to be realized by the implementation of the subgrid scale parameterization of Entekhabi and Eagleson (1989a).

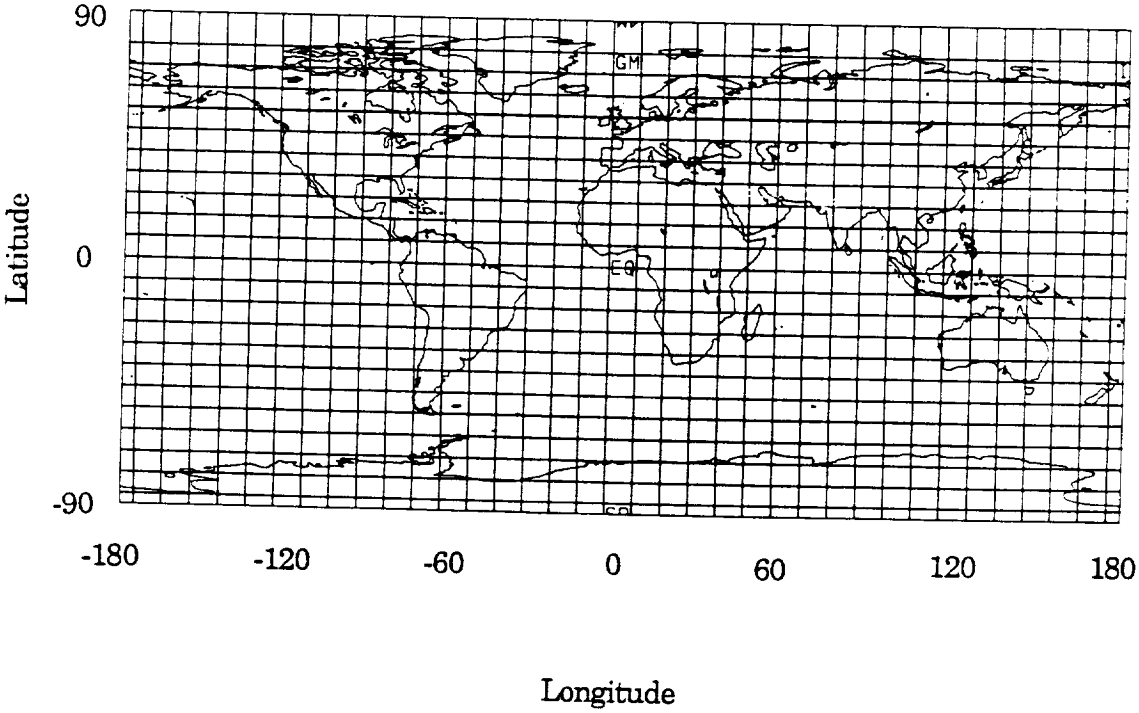

Figure 1.1 Grid discretization of the GISS GCM using 8° × 10° resolution.

2. Improving the Landsurface Hydrological Parameterization in the GISS GCM: An Overview of this Research

Precipitation in GCMs is produced, for each grid and at each time step, according to the physics and thermodynamics of the overlying air column. Similarly the potential evaporation is computed as the surface latent heat flux under conditions of unlimited moisture supply. The task of the landsurface hydrology routine is to partition the incident precipitation into runoff and infiltration and reduce the potential evaporation to the actual value. The partitioning and reducing rates depend on the state of the near–surface soil moisture; therefore the landsurface routine also tracks soil moisture balance.

The current landsurface parameterization in the GISS GCM uses simplified empirical equations; they are chosen for their computational efficiency and adjusted to create reasonable gross estimates of global runoff while also maintaining reasonable surface temperatures over continental regions: " ... [the Model II runoff scheme] yielded 24 cm year^{-1} global runoff and summer continental temperatures about 2–3°C cooler than observed. This intermediate runoff is used in Model II, primarily for its effect on summer temperatures", (Hansen et al., 1983). As will be discussed in detail in Chapter III, there are many shortcomings of this current hydrological parameterization, particularly in runoff and evaporation over tropical regions.

As an improvement on GCM hydrological parameterizations in general, Entekhabi and Eagleson (1989a) developed new formulations for runoff and evaporation. The technique is based on reasonable spatial probability distributions of rainfall and soil moisture; the model updates these variables using the means (first moments) of the distributions. As is illustrated in Fig. 1.2, the probability density function (pdf) for precipitation intensity P in

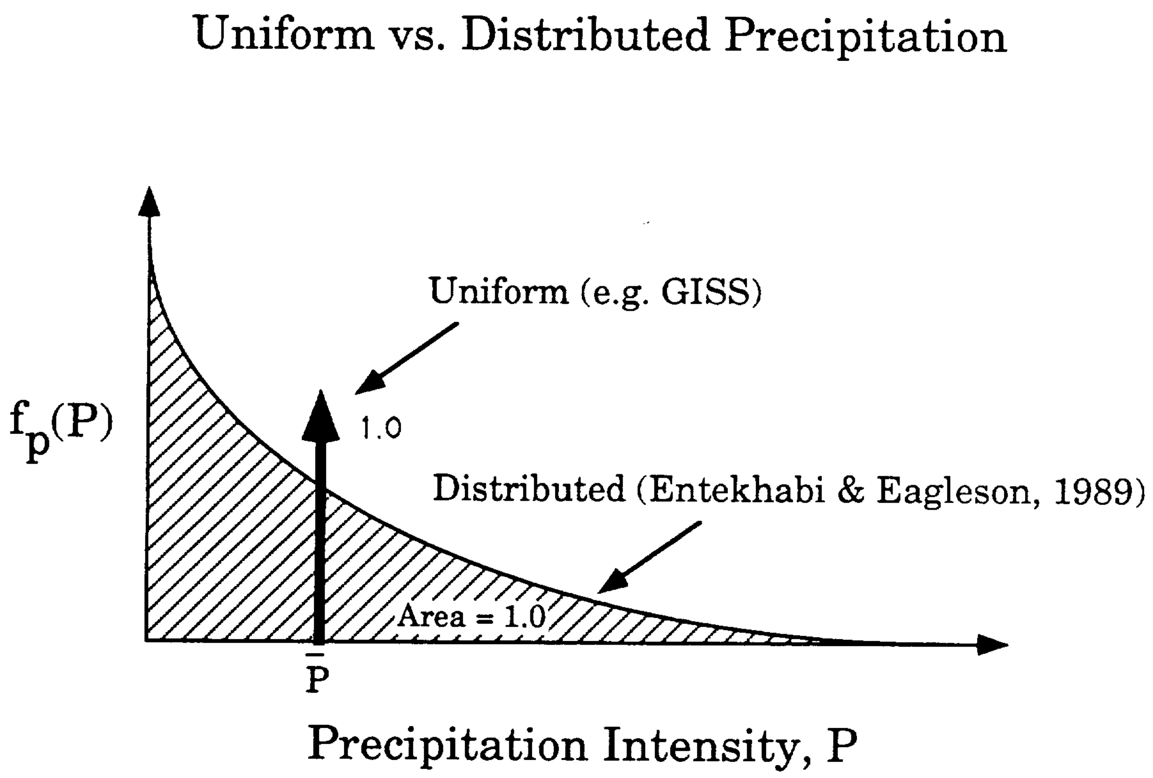

Figure 1.2 Generalized probability distributions of distributed versus uniform precipitation intensity

the GISS model (and all other GCMs used today) is a delta function at the model update (mean) precipitation value. That is, the precipitation is spatially uniform since all probability "mass" is concentrated at the one mean value. Eagleson and Entekhabi (1989a), on the other hand, incorporate a distributed pdf of precipitation which recognizes that rainfall, in nature, is very far removed from a simple uniform structure over the entire grid surface. This curve in Fig. 1.2 assumes that rainstorms consist of large areas of low intensity rainfall and relatively smaller areas of intense precipitation. Later on it will be shown that by assigning a specific mathematical function to this distribution and also one for soil moisture distribution, analytic expressions may be derived for runoff and evaporation. The resulting parameterization has the distinct critical advantage of accounting for spatial variability while being computationally efficient for practical use in GCMs. Preliminary testing of this new parameterization was done on a simplified one–dimensional climate model developed at MIT (Koster et al., 1988, and later modified by Entekhabi and Eagleson, 1989b) based on the GISS GCM.

The goal of this work is to expand the current one–dimensional model to include such things as a soil heat diffusion mechanism (to accommodate seasonal simulations) and the inclusion of root extraction of soil moisture to simulate plant transpiration. Sensitivity will be performed by testing these various aspects in Chapter II. Finally, Chapter III will be devoted to the implementation of the new runoff and evaporation formulations in the GISS GCM. The new soil moisture diffusion scheme of Abramopoulos et al. (1988) will also be implemented with root extraction from lower layers. An evaluation of the results will be done using multiple observation data sets for the global hydrologic cycle and surface temperature.

3. One–Dimensional Modeling as an Efficient Screening Tool

Long–duration simulation experiments with a full three–dimensional GCM for the purpose of testing landsurface hydrological parameterizations is an expensive proposition. It is therefore necessary to use a simpler and more efficient model to screen the many possible simulation experiments so that comprehensive testing in the full three–dimensional GCM is reserved for well–defined and focused experiments. In the case of the one–dimensional model at MIT, computer simulation time requirements are reduced from that of the GISS GCM by a factor of roughly 20. The reduced model must nonetheless contain the major interactions inherent in the full GCM or else the sensitivities in the reduced model and the full GCM will not agree with one another.

The main compromise made to achieve such efficiency lies in the reduction to one dimension. Obviously with only one grid square there can be no network of nodal points over which one may solve the equations of atmospheric motion. Thus pressure levels and winds must be prescribed. The one–dimensional model of MIT, hereafter referred to as the Screening Model, dynamically links one ocean and one land grid in order to contain a complete hydrologic cycle.

The dynamic exchange of heat and moisture between these two grid squares is parameterized. Having thus a simplified ocean source of heat and moisture, and recognizing that most of the physical processes such as radiation, moist convection, and condensation are one–dimensional (vertical in the atmospheric column) even in the GISS GCM, the Screening Model landsurface grid square retains sensitivities and interactions similar to the full three–dimensional GCM. As such it is an effective tool for landsurface hydrological parameterization testing. The screening model will be described in greater detail in subsequent sections.

B. Basic GCM Hydrological Parameterizations

1. The Water Balance

The purpose of hydrological parameterizations in GCMs is essentially to account for regional water balance. Each grid square variable is a point representative of a large area. Precipitation formed in the atmospheric column above a landsurface grid square is partitioned into two components, one infiltrating into the soil and one leaving the grid as surface runoff. Generally there is no lateral surface or subsurface flow between grid squares, and so water movement in the soil is restricted to the single vertical dimension. Surface runoff is eliminated instantaneously from the landsurface, whether adjacent to the ocean or not, under the assumption that it is efficiently delivered to the ocean via rivers. The final component of the terrestrial water balance is then the evapotranspiration from the surface of the soil column. Mathematically we have for each landsurface grid

$$\frac{dW}{dt} = P - e - Q \tag{1.1}$$

where

W water stored in soil column (per unit area)

P precipitation

e evapotranspiration

Q surface runoff

In nature there is a wide variety of detailed processes interacting to produce the final water balance. For example, atmospheric heterogeneities create highly irregular rainfall patterns spatially and temporally; soil texture heterogeneities in combination with topography result in wide variations in runoff and infiltration; myriad varieties, shapes, and sizes of vegetation influence evapotranspiration; fluctuations in the local heat budget cause variability in the ambient temperature, etc. These processes are simplified or neglected altogether in GCMs to accommodate computational constraints.

Runoff and evapotranspiration typically are taken as fractions of precipitation and potential evaporation respectively; empirical relationships with dependence only on relative soil saturation (ratio of water volume to void volume; range: between 0 and 1) are used. Moisture diffusion in the soil is typically a simple mass balance relationship. Some more recent hydrological parameterizations are incorporating much greater detail and are physically–based, but very few offer any sophisticated means of accounting for spatial heterogeneity over the large extent of grid squares. The parameterization of Entekhabi and Eagleson (1989a) is an exception. Section I.B.2 will summarize two very simple parameterizations (those of GISS and GFDL); two of more detail will be described in Section I.B.3 (Sellers et al., 1986, and Dickinson et al., 1986). Section I.C reviews the inclusion of subgrid scale spatial variability using the approach of Entekhabi and Eagleson 1989a).

2. Current GISS and GFDL Hydrology Schemes

The storage component, W, in (1.1) is handled by a simplified diffusion between two layers of soil in the GISS GCM. There is also a surface snow storage during cold seasons. Our concern here, though, is mainly the formulations of runoff and evapotranspiration.

Runoff is taken to be a fraction R of the precipitation. The value

$$Q = RP \qquad 0 < R < 1 \tag{1.2}$$

of R in the GISS Model is taken to be one-half the value of the relative surface soil saturation s

$$R = 1/2\ s \qquad 0 < s < 1 \tag{1.3}$$

where s is defined as

$$s = \frac{W}{W_{FC}} \tag{1.4}$$

where W is again the per unit area stored soil water depth. Any infiltrating water which would exceed soil field capacity is also drained as runoff.

Evaporation in a similar way is taken as a fraction β of potential evaporation e_p. We have

$$e = \beta\, e_p \qquad 0 < \beta < 1 \tag{1.5}$$

The value of β, like R, is parameterized as a simple function of relative surface soil moisture,

$$\beta = s \qquad 0 < s < 1 \tag{1.6}$$

In the GFDL Model (Manabe et al., 1969), the runoff ratio R is replaced by a "bucket" model in which runoff is only produced by an exceedance of soil field capacity. Therefore, for the GFDL model

$$Q = \begin{cases} P - e & W = W_{FC} \\ 0 & W < W_{FC} \end{cases} \tag{1.7}$$

where W_{FC} is the soil field capacity.

The GFDL evaporation function is of the same form as (1.5) but β is given by

$$\beta = \begin{cases} 1 & s_k \geq s < 1 \\ \frac{s}{s_k} & 0 < s < s_k \end{cases} \tag{1.8}$$

Here s_k is a "critical value" of s usually taken to be 0.75.

These very simple empirical relationships, very loosely based on hydrologic research, are used mainly for their computational ease while providing at least a gross similarity between model output and observed data. Two other parameterizations which incorporate a great deal more detail are the SiB (Simple Biosphere, Sellers et al., 1986), and BATS (Biosphere Atmosphere Transfer Scheme, Dickinson et al., 1986).

3. SiB and BATS

The parameterizations of SiB and BATS are improvements insofar as they allow for much greater detail in vegetation and the other surface processes along with more realistic soil diffusion. The basic feature of these two parameterizations is their representation of the soil–vegetation–atmosphere transfer of heat, moisture and momentum through resistance formulation. Here the flux of the property is proportional to the gradient in the property evaluated at two levels; the constant of proportionality is the inverse–resistance. The plethora of detail involving such things as leaf temperature and leaf angle, stomatal and root resistance, canopy heat capacity, interception capacity of leaves, and extinction coefficients of canopies, among others, is too broad to allow a concise summary of equations. The main advantage is the representation of many processes which contribute to the hydrologic cycle as well as the radiation and heat balance. The difficulty of such an approach, however, is that most of the equations are still empirical and furthermore require numerous parameters which must be estimated from sparse data or approximated in some way where data is nonexistent. Also, there are stronger computational demands.

The element missing from both the detailed SiB and BATS schemes as well as from the GFDL and GISS schemes, is the accounting for spatial variability across the large GCM grid area.

C. Hydrological Parameterization with Spatial Variability

The following is a condensed version of the derivation of the runoff coefficient R and evapotranspiration efficiency β after Entekhabi and Eagleson (1989a).

1. Runoff Coefficient

As with the GISS model, runoff Q is also taken as a fraction R of precipitation (see Eq. 1.2). It is through the formulation of R that the dependence on spatial variability is included. After Warrilow et al. (1986) precipitation intensity is assumed to be exponentially distributed over a wetted fraction κ of the grid square,

$$f_P(P) = \frac{\kappa}{E[P]} e^{-\frac{\kappa P}{E[P]}} \qquad P > 0 \qquad (1.9)$$

where E[ ] is the expected value. The parameter κ has been observed for various locations (Eagleson and Wang, 1985) but its choice will be discussed in more detail in Chapter III.

The distribution of surface soil saturation is based on observations by Bell et al. (1980) and Owe et al. (1982). As an approximation, the Gamma distribution is used:

$$f_s(s) = \frac{\lambda^{\alpha}}{\Gamma(\alpha)} s^{\alpha-1} e^{-\lambda s} \qquad \lambda,\alpha,s > 0 \tag{1.10}$$

where the two parameters are given by

$$\lambda = \frac{\alpha}{E[s]} \tag{1.11}$$

$$\alpha = cv_s^{-2} \tag{1.12}$$

where cv_s is the coefficient of variation (ratio of standard deviation to the mean) of surface soil saturation, and $\Gamma(\ )$ is the gamma function. Fig. 1.3 gives field data of cv_s as a function of area. Note that as area approaches typical GCM grid area (10^{-5}km^2), cv_s is approximately 1.

Surface runoff is produced by two mechanisms: the Dunne mechanism and the Horton mechanism. Dunne runoff occurs when the surface soil layer is saturated (i.e., $s \geq 1$). Horton runoff occurs when the precipitation rate exceeds the infiltrability f^* of the first soil layer. The infiltrability is given by the linearized darcy equation of vertical steady flow in porous media for saturated conditions due to ponding:

$$f^* = K(1)\left[\frac{d\psi}{dz}\bigg|_{\text{surface saturation}} + 1\right] \tag{1.13}$$

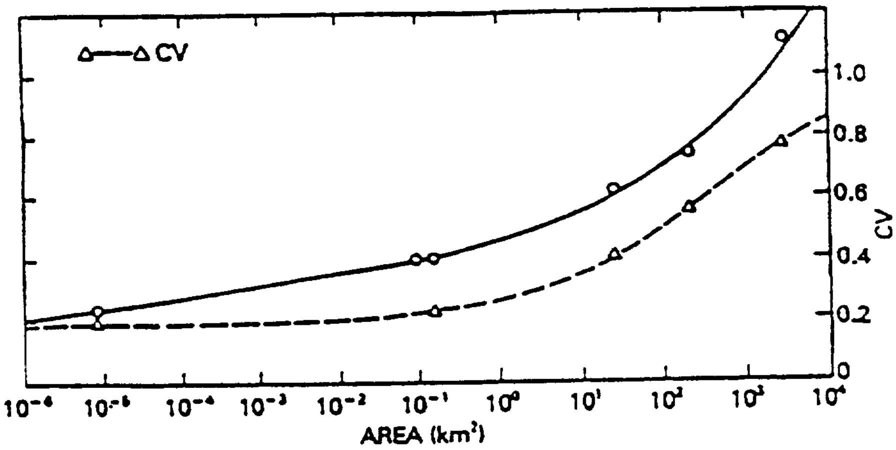

Figure 1.3 Dependence of soil moisture variability on element size.
(Data are from the Hand County, South Dakota site, from Hawley et al. (1983), and from the Washita watershed in Oklahoma.)

where K(1) is the saturated hydraulic conductivity (i.e., for $s = 1$), ψ is the matric head potential. Application of the chain rule to (1.13) results in

$$f^* = K(1)\left[\left.\frac{d\psi}{ds}\right|_{s=1} \frac{s-1}{\Delta z} + 1\right] \tag{1.14}$$

Moisture retention curves are used to determine the value of $\left[\frac{d\psi}{ds}\right]$. Here Δz is the thickness of the surface layer. We are now in a position to write an expression for runoff over the wetted fraction κ, including both Dunne runoff (integrated over all P and $s \geq 1$) and Horton runoff (integrated over $P \geq f^*$ and $0 \leq s \leq 1$):

$$Q = \kappa\left[\int_1^{\infty}\int_0^{\infty} P\, f_P(P)\, dP\, f_s(s)\, ds + \int_0^1\int_{f^*}^{\infty}(P - f^*)\, f_P(P)\, dP\, f_s\, ds\right] \tag{1.15}$$

Substitution of (1.9), (1.10), and (1.14) into (1.15) yields an expression for the dimensionless runoff ratio ($R = Q/E[P]$):

$$R = 1 - \frac{\gamma\left[\alpha, \frac{\alpha}{E[s]}\right]}{\Gamma(\alpha)} + \frac{e^{-\kappa I(1-v)}\ \gamma\left[\alpha, \kappa I v + \frac{\alpha}{E[s]}\right]}{\left[\frac{\kappa I v E[s]}{\alpha} + 1\right]^{\alpha} \Gamma(\alpha)} \tag{1.16}$$

where

$$v = \left.\frac{d\psi}{ds}\right|_{s=1} \frac{1}{\Delta z} \tag{1.17}$$

$$I = K(1)/E[P] \tag{1.18}$$

and $\gamma(,)$ is the incomplete gamma function. E[P] is the grid precipitation rate (produced by model atmospherics) and K(1) is the saturated soil hydraulic conductivity (dependent on soil type).

2. Evapotranspiration Efficiency

As with the GISS parameterization, evaporation is taken as a fraction, β, (called the evaporation efficiency), of potential evaporation (see Eq. (1.5)).

Spatial variability is introduced into the large grid evaporation estimation through soil moisture.

The derivation of bare soil evaporation efficiency β_s begins by using the desorption equation of Philip (1957), which is an approximation to the basic governing equation of vertical moisture diffusion and mass conservation:

$$f_e = \frac{1}{2} S_e \, t^{-1/2} - \frac{[K(s_0) + K(s_1)]}{2} \tag{1.19}$$

where S_e is a constant based on soil properties and s_0 and s_1 are initial and boundary conditions given by

$$\left.\begin{aligned} s(z,0) &= s_0 \\ s(0,t) &= s_1 \end{aligned}\right\} \quad z,t \geq 0 \tag{1.20}$$

A uniform moisture content s_0 holds for the entire profile at relative time zero; a constant s_1 content holds at $z = 0$ at all times. The functional form of S_e is derived by Entekhabi and Eagleson (1989a) based on the work of Parlange et al. (1985):

$$S_e = \left[\frac{8nmK(1)\,\psi(1)}{3(1 + 3m)(1 + 4m)}\right]^{1/2} \tag{1.21}$$

where n is porosity and m is soil pore disconnectedness index.

Unsaturated hydraulic conductivity is parameterized similarly to Brooks and Corey (1966):

$$K(s) = K(1)\ s^{\frac{2}{m} + 3} \tag{1.22}$$

For $s_1 << s_0$, (1.19) may be approximated by

$$f_e \approx \tfrac{1}{2}\, s_e\, t^{-1/2} + \tfrac{1}{2}\, K(s_0) \tag{1.23}$$

Under the circumstances of desorption this is a reasonable assumption.

To accommodate the time step of GCMs (generally one hour), the desorption must be integrated to obtain a mean time–step value:

$$\bar{f}_e = \frac{1}{T}\int_0^T f_e(t)\ dt = S_e T^{-1/2} - \tfrac{1}{2}K(s_0) \tag{1.24}$$

This equation may be rewritten by substitution of Eqs. (1.21) and (1.22) to yield

$$\bar{f}_e = K(1)\ \Omega\ s_0^{\frac{1}{2m} + 2} - \tfrac{1}{2}K(1)\ s_0^{\frac{2}{m} + 3} \tag{1.25}$$

$$\Omega = \left[\frac{8n\psi(1)}{3K(1)T(1 + 3m)(1 + 4m)}\right]^{1/2} \tag{1.26}$$

With the mean desorptivity defined, the bare soil evaporation efficiency may now be obtained following a derived distribution. Whenever $\bar{f}_e$ is less than the potential evaporation rate e_p, the value of $\bar{f}_e$ is the evaporation rate. This is the "soil–controlled" evaporation regime. For $\bar{f}_e$ greater than e_p, the value of e_p determines the evaporation rate; this is the "climate–controlled" evaporation regime. A transitional value of relative surface soil saturation s*, is defined for which the value of $\bar{f}_e$ and e_P are equal (i.e., $\bar{f}_e\big|_{s=s^*} = e_P$), From (1.25) we have

$$e_P = K(1)\Omega\ s^{*\frac{1}{2m}+2} - \tfrac{1}{2}K(1)\ s^{*\frac{2}{m}+3} . \tag{1.27}$$

Using these definitions, then, the expected value of area evaporation or the grid evaporation rate is

$$E[e] = e_P \int_{s^*}^{\infty} f_s(s)\ ds + \int_0^{s^*} \bar{f}_e\ f_s(s)\ ds \tag{1.28}$$

Finally, integration of (1.28) in combination with (1.25), (1.28), and (1.10) results in

$$\beta_s = \frac{E[e]}{e_P} =$$

$$= \frac{\Omega'\gamma\left[\frac{1}{2m} + 2 + \alpha,\ \alpha\mathcal{E}^{-1}\right] - \frac{1}{2}\gamma\left[\frac{2}{m} + 3 + \alpha,\ \alpha\mathcal{E}^{-1}\right]}{\left[\Omega'(\alpha\ \mathcal{E}^{-1})^{\frac{1}{2m}+2} - \frac{1}{2}(\alpha\mathcal{E}^{-1})^{\frac{2}{m}+3}\right]\Gamma(\alpha)} + 1 - \frac{\gamma(\alpha, \alpha\mathcal{E}^{-1})}{\Gamma(\alpha)} \tag{1.29}$$

where

$$\Omega' = \Omega\left[\frac{\alpha}{E[s]}\right]^{\frac{3}{2m}+1} \tag{1.30}$$

$$\mathcal{E} = \frac{E[s]}{s^*} \tag{1.31}$$

We now move to the derivation of the vegetation transpiration efficiency β_v. The derivation is similar to that of β_s except that a soil moisture extraction function $e_v(s)$ by roots takes the place of $\bar{f}_e$. As a simplification of a complex system, the following definition of $e_v(s)$ is used

$$e_v(s) = \begin{cases} 0 & 0 \le s_w \le s_w \\ e_P \dfrac{s - s_w}{s^* - s_w} & s_w < s < s^* \\ e_P & s^* \le s < 1 \\ 0 & \text{saturated} \end{cases} \tag{1.32}$$

where s_w is the plant wilting point soil moisture value and s^* is that above which the transpiration by plants is limited by the climate–controlled potential evaporation. The determination of s_w is based on the Brooks & Corey (1966) equation for partially saturated matric suction:

$$\psi(s) = \psi(1)\, s^{-\frac{1}{m}} \tag{1.33}$$

This may be rearranged and adapted to the wilting point by

$$s_w = \left[\frac{\psi_{wilt}}{\psi(1)}\right]^{-m} \tag{1.34}$$

The derived distribution of evaporation efficiency for vegetated regions now follows from (1.32):

$$E[e_v] = \int_{s_w}^{s^*} e_v(s)\, f_s(s)\, ds + E_P \int_{s^*}^{\infty} f_s(s)\, ds \tag{1.35}$$

Substitution of (1.32) and (1.10) into (1.35) then yields upon integration:

$$\beta_v = \frac{E[e_v]}{e_p} = 1 + \frac{\gamma(\alpha+1,\alpha\mathcal{E}^{-1}) - \alpha\mathcal{E}^{-1}\gamma(\alpha,\alpha\mathcal{E}^{-1}) - \gamma(\alpha+1,\alpha\mathcal{W}^{-1}) + \alpha\mathcal{W}^{-1}\gamma(\alpha,\alpha\mathcal{W}^{-1})}{\Gamma(\alpha)\ (\alpha\mathcal{E}^{-1} - \alpha\mathcal{W}^{-1})} \tag{1.36}$$

where

$$\mathcal{W} = \frac{E[s]}{s_w} \tag{1.37}$$

3. Summary

Thus the runoff coefficient R and the evapotranspiration efficiency β (with differentiation now between bare–soil and vegetated conditions) have been derived from physically based equations of soil water movement in conjunction with spatial variability in precipitation and soil moisture. Empirical relations have only been invoked in situations such as root extraction of soil moisture for which eloquent governing equations simply do not exist.

Chapter III contains plots comparing these functions to those of the current GISS GCM hydrology (see Figs. 3.1a–c). For a more detailed discussion and graphical analysis, the reader is directed to Entekhabi and Eagleson (1989a).

D. Screening Model Description and Enhancements

1. Basic Model Description

The one–dimensional Screening Model used here for further sensitivity testing of landsurface hydrological parameterizations has been described in detail elsewhere (Koster et al., 1988, and Entekhabi and Eagleson, 1989b). As mentioned earlier, the prime advantage of low–dimension climate models is their ability to account for the major feedbacks and sensitivities in the system (in this case those of the landsurface–atmosphere) while requiring only a fraction of the computer resources of GCMs.

The Screening Model has one landsurface "grid–square" and one ocean surface "grid square" (quotes are to indicate the model does not necessarily represent a particular location on earth). Based on the GISS GCM, there are nine atmospheric layers over each surface with pressure levels centered at 984, 917, 807, 650, 480, 329, 206, 105 and 27 millibars. Due to the inherent lack of lateral atmospheric dynamics (because of the one–dimensionality), the pressure tendency is zero (i.e., $dp_s/dt = 0$). The atmospheric interactions of moisture and heat transfer between the two columns are parameterized. After Entekhabi and Eagleson (1989b), these transfers follow a simple linear reservoir scheme for each atmospheric level i:

$$\begin{aligned} \frac{df_{oi}}{dt} &= \frac{f_{ci} - f_{oi}}{\chi} \\ \frac{df_{ci}}{dt} &= \frac{f_{oi} - f_{ci}}{\chi} \end{aligned} \tag{1.38}$$

where, per unit mass,

$$f_i = \begin{cases} q_i & \text{moisture exchange} \\ c_p T_i & \text{heat exchange} \end{cases}$$

The variables q_i and T_i are the specific humidity and temperature at level i and c_p is the specific heat of air at constant pressure. The parameter χ is in units of time and its effects on moisture and heat convergence in the model have been analyzed in Entekhabi and Eagleson (1989b) and comparisons of these effects with observations in the tropics have been studied in Brubaker et al. (1991). With a dynamically linked system of ocean–atmosphere–land there is thus a complete hydrologic cycle operating in the Screening Model.

The other major parameterizations in the model include rainfall production (in the forms of moist–convective origin and large–scale supersaturation), radiation, and landsurface hydrology. A brief description of each follows here.

Large–scale condensation occurs by condensing all vapor necessary to bring atmospheric saturation down (if need be) to 100%. Supersaturation may result from moisture and heat convergence. Moist–convective events are simulated by raising subgrid scale moist parcels pseudo–adiabatically from all nine atmospheric levels to their points of neutral buoyancy. Any moisture which condenses in this process and is not subsequently evaporated at lower levels (as droplets fall) becomes surface rainfall. Latent heat transfers are also accounted for in this scheme. The parcel fraction used is 1/2 the grid square air mass at each atmospheric level.

The radiation scheme is based on Hoffman (1981). Solar radiation is integrated over the model time step and supplies the forcing for the seasonal and diurnal cycles in the model. Clouds are simulated for both reflection and transmission of radiation. Also the major radiatively active gases are represented with their respective absorption spectra. These gases, in order of significance, are H_2O, CO_2, O_3, and O_2.

Sensible heat and evaporation fluxes are parameterized by "drag laws" using a prescribed wind speed. The transfer coefficients are functionally related to the vertical gradients of temperature and specific humidity.

A surface layer (between the ground and the first atmospheric layer) is used to give a finer resolution. At each time-step, iterations are performed until the heat and moisture fluxes from the ground to the surface layer are equal to those between the surface layer and the first atmospheric layer.

Another facet of the Screening Model which is of importance to the work here is the incorporation of the Abramopoulos et al. (1988) multiple soil layer moisture diffusion scheme. We present here a summary of the equations including a transpiration sink term from each soil layer.

Each soil layer has thickness Δz_i, porosity n_i, and relative soil saturation s_i. The stored water depth w_i is,

$$w_i = n_i s_i \Delta z_i \tag{1.39}$$

Refer to Fig. 1.4 for a schematic diagram. The fluxes F_i entering and leaving each soil layer follow the darcy equation

$$F_i = K\frac{H_{i-1} - H_i}{z_{i-1} - z_i} \tag{1.40}$$

where H is the total hydraulic head, K is the hydraulic conductivity, and the subscript i refers to layer i (in the case of H) and the interface at the top of layer i (in the case of F and z). Hydraulic conductivity is assumed constant in the vertical. The fluxes of evapotranspiration e_{v_i} are evaluated by

$$e_{v_i} = \epsilon_i \beta_{v_i} e_P \tag{1.41}$$

where ϵ_i is the root fraction in layer i (the sum of all ϵ_i is then unity), β_{v_i} is the evaporation efficiency (evaluated at soil saturation s_i) discussed in previous sections. Resistances along the plant root system are considered negligible.

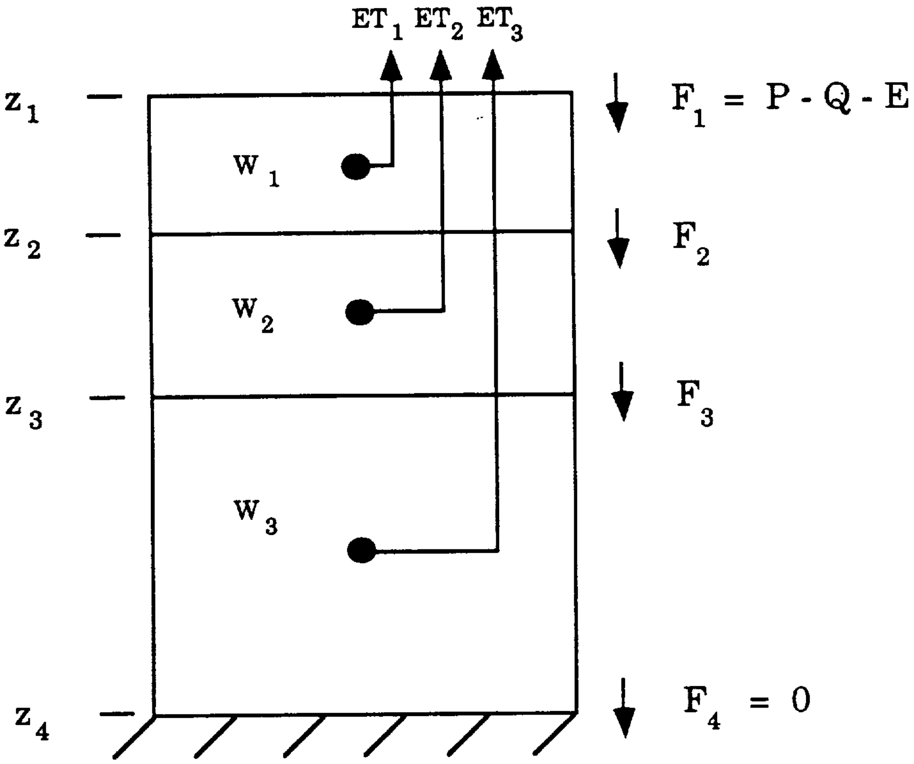

Figure 1.4 A three–layer version of the Abramopoulos et al. (1988) soil moisture diffusion scheme.

The change in stored water w_i at each soil layer i during a time step Δt is then

$$\frac{\Delta w_i}{\Delta t} = F_i - F_{i+1} - e_{v_i} \tag{1.42}$$

An implicit time scheme is used for the fluxes resulting in the following matrix of linear algebraic equations

$$A \Delta w = b \tag{1.43}$$

where

$$A_{k,i-1} = \frac{\partial F_i}{\partial w_{i-1}} \Delta t \tag{1.44a}$$

$$A_{k,i} = \left[\frac{\partial F_{i+1}}{\partial w_i} - \frac{\partial F_i}{\partial w_i} - \frac{\partial eT_i}{\partial w_i} \right] \Delta t - 1 \tag{1.44b}$$

$$A_{k,i+1} = \frac{\partial F_{i+1}}{\partial w_{i+1}} \Delta t \tag{1.44c}$$

$$b_i = (F_i - F_{i+1} + e_{v_i}) \Delta t \tag{1.44d}$$

The boundary condition at the surface is given by the net moisture entering the soil column:

$$\begin{aligned} F_1 &= P - Q \qquad (1.45) \\ &= P(1 - R) \end{aligned}$$

At the lowermost boundary a zero flux boundary condition is used. Sensitivity to this will be examined in Chapter II using conditions of an open column draining by gravity.

2. Enhancements to the Screening Model

The main modification to the Screening Model has been the incorporation of multiple soil layers to simulate seasonal heat storage in the ground. Heat storage in the soil is necessary to allow long-duration simulations with a seasonal cycle (heretofore the Screening Model has been used mainly for perpetual-day simulation).

To provide seasonal heat storage, we follow Hansen et al. (1983) using a finite difference scheme to solve the heat conduction equation. The governing equation is

$$\frac{\partial T}{\partial t} = \frac{\lambda}{C_g} \frac{\partial^2 T}{\partial z^2} = K_g \frac{\partial^2 T}{\partial z^2} \tag{1.47}$$

where T is temperature, λ is the soil thermal conductivity, C_g is the heat capacity per unit volume, and K_g is the thermal diffusivity. Fig. 1.5 gives a soil profile schematic showing the fluxes of heat. For a 3-layer soil scheme, the flux equations are

$$\Delta z_1 c_1 \frac{dT_1}{dt} = F_0 - F_1 \tag{1.48a}$$

$$\Delta z_2 c_2 \frac{dT_2}{dt} = F_1 - F_2 \tag{1.48b}$$

$$\Delta z_3 c_3 \frac{dT_3}{dt} = F_2 - F_3 \tag{1.48c}$$

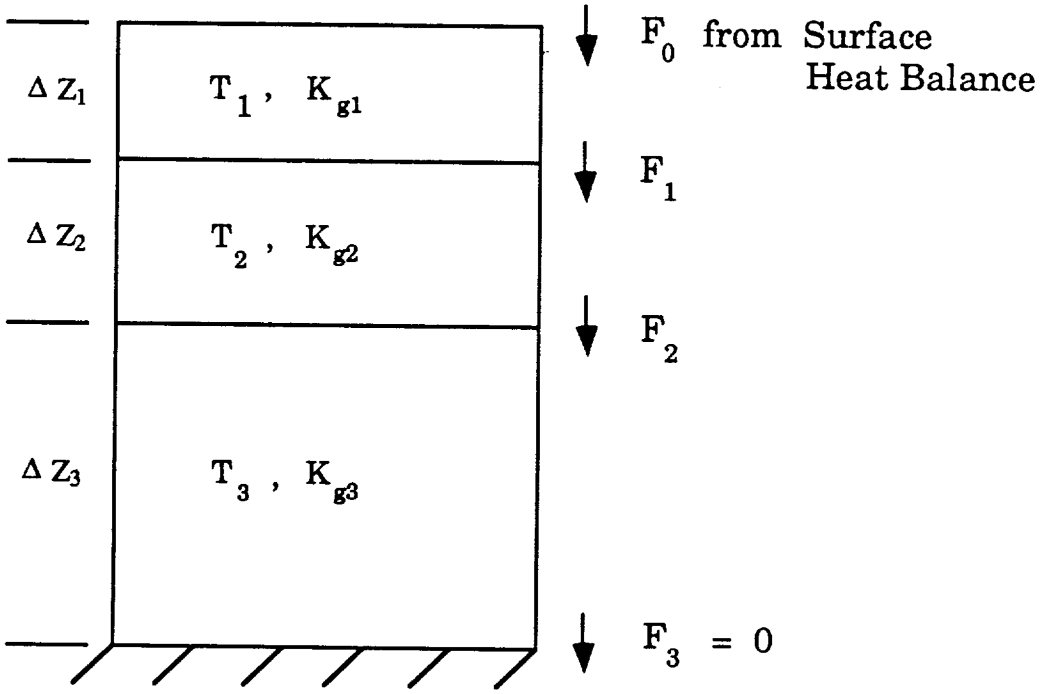

Figure 1.5 Soil heat diffusion schematic for 3–layer soil

The boundary conditions are given by the net energy balance at the surface for F_0 at each time–step. The lowermost boundary is considered a no–flux boundary ($F_3 = 0$). Using a centered difference scheme, we have for F_1 and F_2

$$F_1 = \frac{3T_1 - 3T_3 - \frac{1}{2} F_0 \frac{\Delta z_1}{\lambda_1} - \frac{1}{2} F_2 \frac{\Delta z_2}{\lambda_2}}{\frac{\Delta z_1}{\lambda_1} + \frac{\Delta z_2}{\lambda_2}} \tag{1.49a}$$

$$F_2 = \frac{3T_2 - 3T_3 - \frac{1}{2} F_2 \frac{\Delta z_2}{\lambda_2}}{\frac{\Delta z_2}{\lambda_2} + \frac{\Delta z_3}{\lambda_3}} \tag{1.49b}$$

We assume constant thermal properties for all layers using $\lambda = 0.42$ w/m/K and $c_g = 1.13 \times 10^6$ J/m^3/k.

We have now given the background material necessary for the climate simulations done with the Screening Model (Chapter II) and the full three–dimensional GISS GCM (Chapter III). Summaries of the results along with suggestions and recommendations for the GISS model and for further research will be given in Chapter IV, the concluding chapter.

Chapter II

Numerical Experiments with the One–Dimensional Screening Model

A. Introduction

This chapter is devoted to sensitivity experiments performed with the One–dimensional Screening Model described in Chapter I. The effects of changes in some key boundary conditions have not been analyzed in the past (Entekhabi and Eagleson, 1989b). Among these are the sensitivity to soil storage capacity and heat capacity (i.e., depth of the soil column), sensitivity to percolation from the lowest soil layer, and sensitivity to transpiration extraction from lower soil layers.

The experiments with the Screening Model are intended to provide guidelines for the implementation of the Entekhabi and Eagleson (1989a) and the Abramopoulos et al. (1988) hydrologic parameterizations. Sensitivities that are determined through experimentation with the Screening Model form the basis for the choice of parameters to be used in the full GCM. This approach allows more efficient use of the GCMs and their associated computational facilities for more focused numerical climate experiments.

B. Screening Model Experiments

Here we examine hydrologic sensitivity to soil water and heat capacity, to groundwater percolation, and to lower layer transpiration by plants. The series of numerical experiments defined for the Screening Model are listed in Table 2.1.

Table 2.1 Simulations performed in the Screening Model

K–1	Control Run, light Soil
K–2	Control Run, heavy soil
K–3	Proportionally 1/2 × nominal soil layer thicknesses, light soil
K–4	Proportionally 2 × nominal soil layer thicknesses, light soil
K–5	Proportionally 4 × nominal soil layer thicknesses, light soil
K–6	Top layer: Nominal; lower layers: 4 × nominal thicknesses, light soil
K–7	Groundwater percolation from lowest soil layer, light soil
K–8	Groundwater percolation from lowest soil layer, heavy soil
K–9	Transpiration Control Run, shallow soil column, light soil
K–10	Root fractions /.75, .15, .10/ , shallow soil column, light soil
K–11	Root fractions /.85, .10, .05/ , shallow soil column, light soil
K–12	Transpiration Control Run, deep soil column, light soil
K–13	Root fractions /.75, .15, .10/ , deep soil column, light soil
K–14	Root fractions /.85, .10, .05/ ., deep soil column, light soil
K–15	Transpiration Control Run, shallow soil column, heavy soil
K–16	Root fractions /.75, .15, .10/, shallow soil column, heavy soil
K–17	Root fractions /.85, .10, .05/, shallow soil column, heavy soil
K–18	Transpiration Control Run, deep soil column, heavy soil
K–19	Root fractions /.75, .15, .10/, deep soil column, heavy soil
K–20	Root fractions /.85, .10, .05/, deep soil column, heavy soil

In order to use the hydrological parameterization of Entekhabi and Eagleson (1989a), relevant parameters must be assigned representative values of their mean over the landsurface region. Table 2.2 contains values for soil hydraulic properties as given in Entekhabi and Eagleson (1989a); this information is also used in these simulations. In addition, the model requires a number of other boundary conditions and specifications. These are given in Table 2.3, and are also based on Entekhabi and Eagleson (1989b).

1. Sensitivity to Soil Water and Heat Capacity

Table 2.3 designates a "nominal" distribution of soil layer thicknesses for a three–layer version of the Abramopoulos et al. (1988) soil moisture diffusion scheme (Control Run K–1 with "light" soil). These thicknesses follow a roughly geometric progression and combine to form a total soil column depth of 75 cm. Obviously there are many regions on earth having a mean depth to bedrock greater than (or possibly less than) 75 cm. The reason a particular model depth is chosen is usually based first of all on the thickness of the upper layer since it has a strong impact on fluxes in and out of the soil system. Its chosen thickness is also tied to the model time step because often an assumption is made that moisture and heat become uniformly distributed in the upper soil layer within the period of a time step. Once upper layer thickness is determined, a progression is chosen for subsequent underlying soil layer thicknesses with geometric progression; this also gives a numerically stable behavior.

To test the effect of soil layer thicknesses, we examine cases wherein the proportions of the three soil layers to each other remain the same but the total depth is changed to 1/2×, 2×, and 4× the nominal total depth. Also, a

Table 2.2 **The definition of soil hydraulic properties (after Entekhabi and Eagleson, 1989a)**

		SAND	SILT	CLAY
m	Pore-size distribution index	3.3	1.2	0.4
K(1)	Saturated hydraulic conductivity $[10^{-3}\text{m hr}^{-1}]$	7.5	2.2	0.3
$\Psi(1)$	Saturated matric potential [m]	0.23	0.46	0.93
n	effective porosity	0.25	0.35	0.45
Ψ_{wilt}	wilting matric potential$[10^2\ \text{kPa}]$	-15		

Table 2.3 **Representative specifications for the Screening Model**

PARAMETER	VALUE		
Simulation Period	One Year (with one year spin–up)		
Latitude	15° North		
Fixed Ocean Surface temperature	25° C		
Cloud temperature standard deviation	3° C		
	LAND		OCEAN
Surface Wind Speed	2 ms^{-1}		5 ms^{-1}
Albedos	.25		.35
Soil texture fractions	SAND	SILT	CLAY
"light"	.75	.20	.05
"heavy"	.15	.15	.70
Nominal 3–layer Soil Column	Layer 1	Layer 2	Layer 3
Thickness	10 cm	15 cm	50 cm
Rainfall fractional wetting, κ	0.60		
Soil moisture coefficient of spatial variability, cv_s^*	1.0		
Land–Ocean atmospheric exchange parameter, χ	1.67 days		

final run using the nominal *top* layer thickness (10 cm) and 4× nominal *lower* layer thicknesses will be used to test the influence of the top layer thickness alone. Light soil textures (see Table 2.3) are used for these simulations. Similar results are expected for heavy soil texture since the main sensitivity is to heat and moisture storage capacity.

The heat and moisture diffusion in the soil column is estimated using a finite difference scheme with three nodes only. The reasoning behind such a coarse discretization is to gain computational efficiency. Deep soil storage of heat and moisture is believed to dampen the amplitude of the seasonal cycle of modeled hydrologic fluxes as well as the temperature at the surface. The total depth of the soil will affect the amplitude of the annual cycle while the thickness of the topmost layer should more directly affect the amplitude of the diurnal cycles. With the Screening Model, we intend to verify and quantify these sensitivities.

Each of the simulations K–1 through K–20 (i.e., inclusive of the soil layer thickness sensitivity simulations considered now) was given a one–year spin–up period and diagnostics were collected during the following one–year period. Hydrologic equilibrium is reached by the end of each spin–up period since, unlike GCMs that have long memory in the ocean component and low frequency atmospheric regimes, the Screening Model reaches a stationary state once the soil heat and moisture storages are compatible with the net fluxes across the land surface.

We point out that Run K–5 (4× nominal soil layer thicknesses) is actually inconsistent with the runoff derivation of Chapter I. This experiment is considered to be instructive as an extreme condition. The runoff parameterization infiltration equation (Eq. 1.13) requires the top layer thickness to be comparable to the penetration depth of a wetting front over one time step (one hour). Run K–5 uses a 40 cm top layer which is too thick to meet this condition.

Finally, before presenting results, we point out that in regard to diffusion in the soil, the direct effect of *increased* soil layer thicknesses will be to *decrease* the fluxes of moisture and heat transfer within a given layer. This becomes evident when considering that the moisture flux given by Darcy's Law (see Eq. 1.40) is directly proportional to the total hydraulic head, which is the sum of the gravitational and pressure heads:

$$H = z + \psi(s) \tag{2.1}$$

Equation (1.40) may then be rewritten

$$\begin{aligned} F_i &= K \, \frac{(z_{i-1} \psi_{i-1}) - (z_i + \psi_i)}{z_{i-1} - z_i} \\ &= K \, \frac{\Delta\psi_\ell + \Delta z_\ell}{\Delta z_\ell} \end{aligned} \tag{2.2}$$

where subscript ℓ refers to a layer whose top and bottom elevations are z_{i-1} and z_i, respectively. Thus since $\Delta\psi_\ell$ will be non–zero for virtually all cases (except perfectly uniform vertical moisture profiles), any increase in Δz_ℓ will result in a reduced moisture flux. That is, for a constant nonzero $\Delta\psi_\ell$, the ratio of $(\Delta\psi_\ell + \Delta z_\ell)$ to (Δz_ℓ) decreases with increased Δz_ℓ. By the same argument using Eqs. (1.48) and (1.49) the heat flux is also reduced, all other variables being constant.

The results of the sensitivity simulations for various soil layer thicknesses are given in Table 2.4. The diagnostics of the water and heat budgets are annual averages and ranges (in parentheses) of:

s(1)	Relative soil saturation of top layer [ ]
P	Precipitation [mm/day]
P_i	Mean precipitation intensity (i.e., intensity when precipitating) [mm/day]
e	Evaporation [mm/day]
Q	Runoff [mm/day]
$-\nabla \cdot q$	Atmospheric convergence of moisture over landsurface [mm/day]
T_{g_1}	Temperature of top soil layer [C]
LE	Latent heat flux over landsurface [W/m^2]
SH	Sensible heat flux over landsurface [W/m^2]
F_g	Heat flux into soil [W/m^2]
$-\nabla \cdot F_a$	Atmospheric convergence of heat over land surface [W/m^2]

Two salient features of Table 2.4 are that 1) as the total soil column depth is increased and the layer thickness proportionality is maintained the climate becomes steadily and considerably drier (compare s(1), P, E and R as well as temperatures in Runs K–1 to K–5), and 2) When the thickness of the topmost layer is held constant, even large changes in lower layer thicknesses produce little or no change in the mean annual climate (Run K–6 and Run K–1 are nearly identical); the annual *range* of climatic variables, however,

Table 2.4 **Annual mean water and heat budgets for simulations varying the soil layer thicknesses**

(Numbers in parentheses are annual ranges of monthly-averages)

WATER BALANCE

	s(1)[ ]	P[mm/day]	Pi[mm/day]	e[mm/day]	Q[mm/day]	$-\nabla_q$[mm/day]
K-3 ($\frac{1}{2}$× Nominal)	0.32 (0.36)	4.64 (2.54)	35.57 (95.84)	3.74 (1.91)	0.78(0.90)	0.88(0.94)
K-1 (Nominal)	0.22 (0.17)	4.35 (1.41)	41.24 (36.10)	3.58 (1.26)	0.75 (0.50)	0.76 (0.75)
K-4 (2× Nominal)	0.13 (0.11)	3.67 (2.76)	78.74 (74.37)	3.09 (1.47)	0.56 (0.71)	0.56 (1.19)
K-5 (4× Nominal)	0.08 (0.08)	3.12 (2.02)	101.5 (98.29)	2.72 (1.27)	0.38 (0.82)	0.39 (0.81)
K-6 (Top: Nominal Lower Layers: 4×)	0.20 (0.13)	4.33 (1.25)	44.55 (35.15)	3.63 (1.12)	0.73 (0.55)	0.72 (0.72)

HEAT BALANCE

T_{g1}[C]	Le[W/m^2]	SH[W/m^2]	F_g[W/m^2]	$-\nabla F_q$[W/m^2]	
K-3 (1/2× Nominal)	23.0 (8.9)	108.1 (55.5)	29.9 (50.6)	-1.1 (3.0)	-13.0 (45.1)
K-1 (Nominal)	23.4 (7.6)	103.6 (36.4)	25.6 (39.9)	0.0 (2.5)	-12.3 (70.8)
K-4 (2× Nominal)	25.3 (6.8)	89.3 (42.5)	29.1 (42.4)	-0.4 (3.9)	-12.0 (58.8)
K-5 (4× Nominal)	27.2 (10.3)	78.7 (36.7)	29.9 (45.1)	0.4 (3.8)	-12.6 (72.8)
K-6 (top: Nominal lower layers: 4×)	23.3 (6.6)	105.0 (32.6)	23.8 (29.1)	0.0 (3.3)	-8.4 (58.7)

is generally decreased as the lower layer thicknesses are increased. Supporting the first point we see that as the total soil depth increases from 1/2× nominal to 4× nominal depth (Runs K–3, K–1, K–4, K–5), all components of the annual mean water balance are decreased. In the heat balance we see a steady increase in mean surface ground temperature and a steady decrease in latent heat flux. As drier conditions ensue the sensible heat flux takes on a greater role in the surface cooling since there is less water available for cooling by latent heat flux. As a measure of aridity, the Bowen ratio of sensible to latent heat flux generally follows a rise with greater total soil depth.

There is a striking similarity of Run K–6 to Run K–1 in all of the annual mean diagnostics (Run K–6 has a nominal *top* layer depth of 10 cm, with *lower* layers 4× the nominal depth). The annual *range*, however, particularly evident in s(1) and T_{g1}, is reduced by the larger storage capacity in Run K–6. One other obvious feature of Table 2.4, to be discussed shortly, is the dramatic increase in precipitation intensity P_i when the climate becomes warmer and drier.

It was mentioned earlier that the total depth of the soil ought to affect the *annual* cycle of heat and moisture while the thickness of the top layer ought to have a greater impact on the *diurnal* cycle. Thus Run K–6 ought to follow the trend of the other simulations in *annual range* according to its *total* soil column depth while following the *diurnal range* according to its *top* soil layer depth. This is borne out in Fig. 2.1, which demonstrates this hypothesis in graphical form with respect to temperature by plotting the mean *annual* range of surface ground temperature against *total* soil column thickness (top) and the mean *diurnal* range against the *top* soil layer thickness (bottom). As shown, Run K–6 follows the trend of the others in both plots.

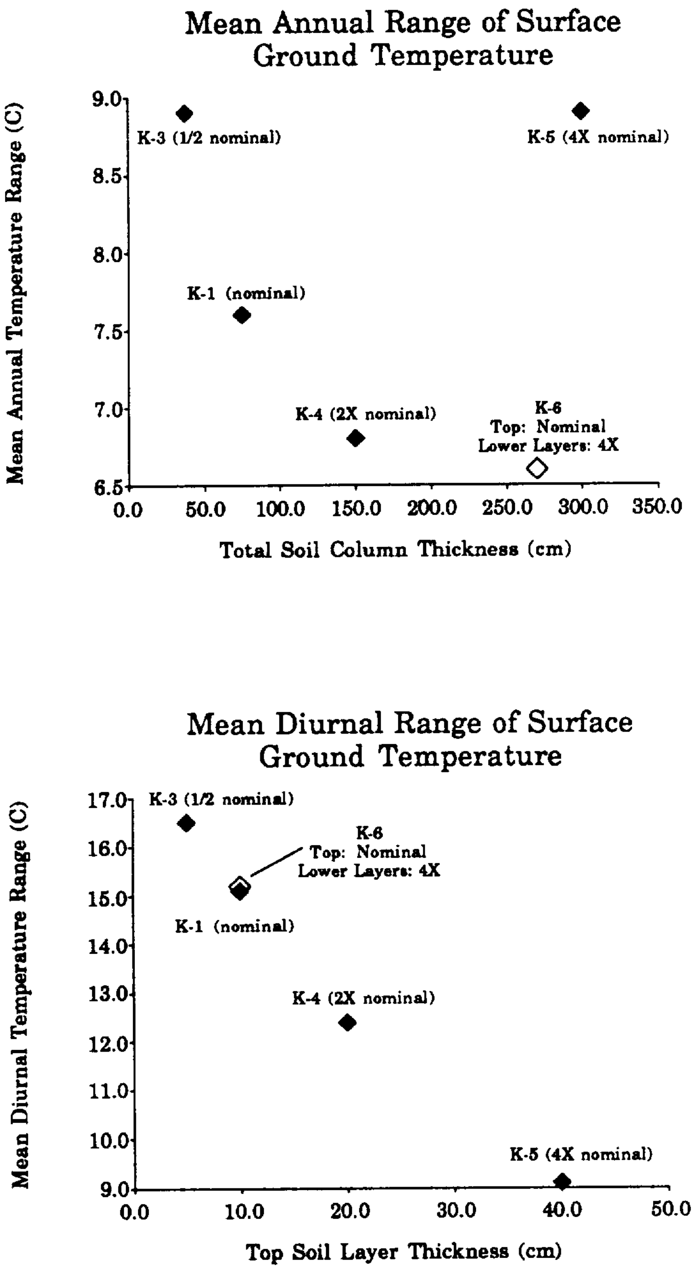

Mean Annual Range of Surface Ground Temperature

Mean Diurnal Range of Surface Ground Temperature

Figure 2.1 Mean annual (top) and diurnal (bottom) ranges of surface ground temperature versus total soil column thickness and top soil layer thickness

There is an apparent discrepancy in the upper plot of Fig. 2.1 in the case of Run K–5. In spite of having the highest heat and moisture capacity, it has a very *large* mean annual surface ground temperature range. The reason for this lies in the *secondary* effects (feedbacks) which are producing excessively dry and hot summer conditions. In the winter, the soil moisture increases again to give lower surface temperatures roughly comparable to those of Run K–4. Thus the annual range of Run K–5 is quite large.

Annual ranges of relative surface soil moisture are given in Fig. 2.2. Again, for the *annual range* of s(1) we see Run K–6 behaving according to its *total* soil column depth. Recall from Table 2.4 that the annual *mean* of s(1) in Run K–6 is nearly identical to that of Run K–1 (control). This is also true of annual mean surface ground temperature T_{g1}.

Thus we may conclude that the climate mean values of the water and heat balance diagnostics are influenced mainly by the *top* soil layer thickness. The *diurnal ranges* also depend most strongly on the top layer thickness. The *annual ranges*, however, depend on the *total* soil column depth.

2. Moist Convection Intensity and Land Surface Temperature

As evident in Table 2.4, as precipitation in the mean is reduced and the climate becomes warmer and drier, precipitation *intensity* is nonetheless greatly increased. By precipitation intensity we mean the average rainfall rate when it is raining. Rainfall in the Screening Model is produced mainly by the moist–convective mechanism, which is dependent on vertical potential temperature and specific humidity gradients in the atmosphere. Fig. 2.3 shows that the increase in mean precipitation intensity P_i is strongly dependent on mean surface ground temperature. Moist static stability, the main criterion of

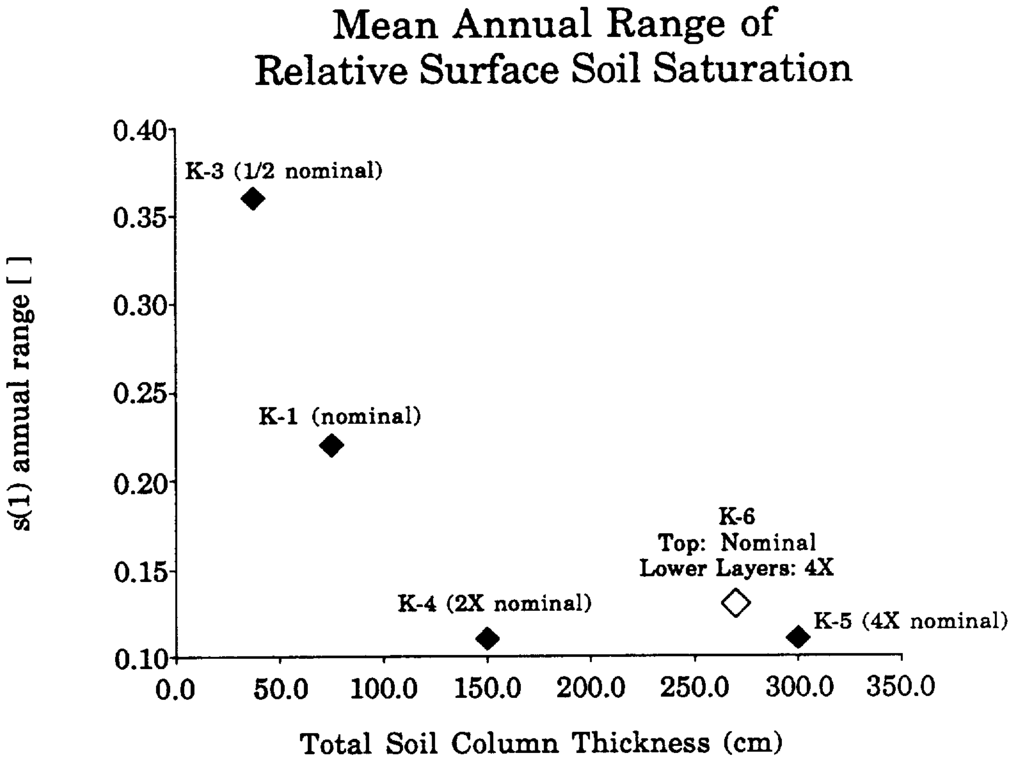

Figure 2.2 Mean annual range of surface relative soil saturation versus total soil column thickness

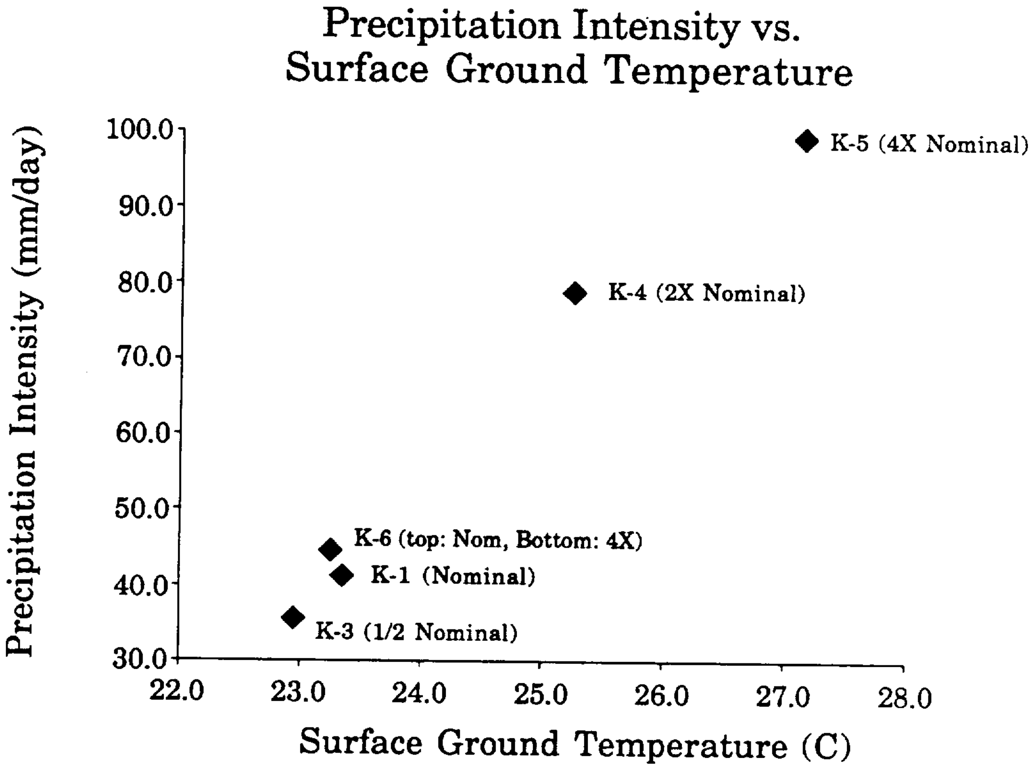

Figure 2.3 Mean annual precipitation intensity versus surface ground temperature

the moist–convective mechanism, is apparently in direct correlation with surface ground temperature for these ranges since the ground temperature is an indicator of energy influx at the bottom boundary of the air column. This energy drives the atmospheric overturning and convection.

3. Sensitivity to Groundwater Percolation

This section examines sensitivity to a simple formulation of groundwater percolation from the soil column as given by Runs K–7 and K–8; Runs K–1 and K–2 serve as control cases.

In most GCM landsurface hydrological parameterizations a no–flux boundary condition is used at the bottom of the soil column for the solution of soil moisture diffusion equations (see Fig. 1.3). It may be advantageous however, particularly in humid regions or places with deep soils, to modify the standard soil column to account for groundwater runoff. As a test of climate sensitivity to groundwater runoff we have simply changed the lower boundary condition of Fig. 1.3 (using Eqs. 1.42 through 1.44d) from a no–flux condition to one of a *constant* flux through the lower layer by setting F_4 equal to F_3. Percolation through the lower boundary is then considered groundwater runoff.

Two simulations were run--one using light soil (Run K–7) and one using heavy soil (Run K–8). All other boundary conditions and specifications are given by Tables 2.2 and 2.3. A 1–year spin–up period was used followed by a 1–year period of diagnostics collection.

The results are presented in Table 2.5, using the same notation as that for Table 2.4 except that Q_{TOT} represents the total runoff and Q_{GW} represents the groundwater runoff. These runoff diagnostics show that the strongest impact of groundwater percolation is in the light soil case. This is

Table 2.5 **Annual mean water and heat budgets for simulations showing sensitivity to groundwater percolation**

(Numbers in parentheses are annual ranges of monthly-averages)

WATER BALANCE

	s(1)[ ]	P[mm/day]	e[mm/day]	Q_{TOT}[mm/day]	Q_{GW}[mm/day]
Light Soil					
K-1 (Control)	0.22 (0.17)	4.35 (1.41)	3.58 (1.26)	0.75 (0.50)	-----
K-7 (percolation)	0.15 (0.10)	3.93 (2.68)	3.12 (1.46)	0.84 (1.00)	0.38 (0.39)
Heavy Soil					
K-2 (control)	0.22 (0.13)	4.29 (0.88)	3.60 (1.22)	0.70 (0.62)	-----
K-8 (percolation)	0.21 (0.17)	4.50 (2.03)	3.79 (1.36)	0.73 (0.82)	0.04 (0.04)

HEAT BALANCE

	T_{g1}[c]	Le[W/m^2]	SH[W/m^2]	F_g[W/m^2]	$-\nabla F_q$[W/m^2]
Light Soil					
K-1 (control)	23.4 (7.6)	103.6 (36.4)	25.6 (39.9)	-0.0 (2.5)	-12.3 (7.08)
K-7 (percolation)	23.9 (7.6)	90.2 (42.3)	35.8 (42.6)	0.1 (2.7)	-8.3 (58.2)
Heavy Soil					
K-2 (control)	23.1 (5.8)	104.3 (35.5)	22.7 (26.6)	-0.3 (2.9)	-7.7 (44.2)
K-8 (percolation)	23.3 (5.8)	109.7 (39.3)	20.9 (15.9)	-0.3 (2.7)	-10.3 (56.2)

reasonable since light soil has a much higher saturated hydraulic conductivity than heavy soil (see Table 2.2). Although Q_{GW} in the light soil case increased from zero (control) to 0.38 mm/day in Run K-7, nevertheless the surface runoff was correspondingly decreased such that total runoff Q_{TOT} increased by only 10%. The surface relative soil saturation s(1) was nonetheless decreased substantially by (roughly 30%) since a greater portion of soil moisture was partitioned to the lower layers. Because of the drier top layer, the surface fluxes of precipitation, evaporation and runoff all decreased from those of the Control Run. The reason the *total* runoff Q_{TOT} increased is that the groundwater runoff more than makes up the difference for the reduced surface runoff.

In the heavy soil case (Run K-8), groundwater runoff is practically negligible. It does, however, have a slight effect on the modeled climate. Precipitation and evaporation are both increased over the Control Run although the surface runoff remains unchanged and the mean soil moisture actually decreases. The annual *ranges* of the water balance variables, particularly for precipitation, are all increased. Apparently the mean values of P and E are increased due to their high values during humid time periods.

It is not clear what mechanism is responsible for the marked increase in the annual range of P for both the light soil and heavy soil cases. A possible explanation is that it is due to the interaction of precipitation and evaporation with the soil. Since the top soil layer has less stability with regard to moisture retention due to groundwater percolation, it may be that the feedback of the atmosphere involves a high variability in precipitation. However, the ranges given are of *monthly* averages so that increases in the range must involve long time constants in the system. Also, atmosphere-soil feedbacks ought to affect evaporation in the same way as precipitation, yet we see the increase in the range of evaporation is much smaller than the increase in the precipitation range.

We conclude that groundwater runoff in this simple formulation is most significant in light textured soils having the effect of increasing total runoff while creating an overall drier climate.

It should be noted that for actual implementation in a GCM, topographic information ought to be used to obtain an average terrain slope to be used in the groundwater runoff formulation. Groundwater percolation is the flow rate under gravity head. For a bedrock with a certain slope, the groundwater percolation equals the unsaturated hydraulic conductivity multiplied by this slope. Since slopes are generally small over large regions, this contribution to large–scale or continental runoff may be small although it may play an important role in redistributing moisture in localized parts of river basins.

The experiments performed through Runs K–7 and K–8 represent open drainage at the bottom of the soil column (i.e., gravity hydraulic head is unity). They thus represent the extreme case and the upper bound on the influence of groundwater percolation in GCM landsurface hydrology.

4. Sensitivity to Lower Layer Transpiration

This section examines sensitivity to the root distribution in the soil column. The experiments are defined as Runs K–9 through K–20 in Table 2.1.

In the simulations discussed thus far, transpiration has been allowed from the top soil layer only. This corresponds to a root distribution of $\epsilon_1 = 1.0$, $\epsilon_2 = 0.0$, $\epsilon_3 = 0.0$ (see Eq. 1.41). As a compact way of representing this we use the notation /1.0, 0.0, 0.0/ for the three soil layers. Because of the wide diversity of vegetation over areas as large as GCM grids, exact representation of plant root distribution is impossible. Nevertheless, moisture extraction by roots can be a significant component of evapotranspiration. To identify model sensitivity to these effects a set of simulations is performed as a guide for implementing the Abramopoulos et al. (1988) parameterization into the GISS GCM (to follow in Chapter III).

Based on the studies of plant root geometry by Epstein (1973), the root distributions used in the simulations are roughly exponential, with the greatest concentration of roots in the upper soil layer. Because preliminary simulations showed a strong tendency toward drying in the lower soil layers, the fractions of roots in the lower layers were kept relatively low. In the simulations presented here, we use root distributions of /0.85, 0.10, 0.05/ and /0.75, 0.15, 0.10/ for cases of heavy soil and light soil. Furthermore, based on the results of II.B.1 and anticipating the implementation of the soil diffusivity scheme into the GISS GCM, two cases of soil layer thicknesses are used--a shallow case and a deep case. Both of these cases use a top layer thickness of 10 cm and a middle layer thickness of 15 cm. The lowest layer thickness is set to 25 cm for the shallow case and 200 cm for the deep case. All other boundary conditions and specifications are as given in Tables 2.2 and 2.3.

The results of the simulations are presented in Table 2.6 following the same format as Tables 2.4 and 2.5. In general, the effect of increasing the transpiration flux from the lower soil layers is a slightly more humid climate. The top layer is slightly more moist since the lower layers are now taking some of the burden for seasonally high evapotranspiration. While the sensitivity of the top soil layer moisture ranges from being essentially

Table 2.6 Annual mean water and heat budgets for simulations testing sensitivity to lower layer transpiration

(Numbers in parentheses show annual ranges of monthly averages;
Numbers following simulation names give 3-layer root distributions)

	s(1)[ ]	P[mm/day]	E[mm/day]	Q[mm/day]
Light soil, shallow column				
K-9 (/1.,0.,0./)	.17 (.15)	3.82 (1.85)	3.28 (1.21)	0.57 (0.66)
K-10 (/.75,.15,.10/)	.20 (.15)	4.09 (1.73)	3.46 (1.28)	0.64 (0.82)
K-11 (/.85,.10,.05/)	.20 (.09)	4.15 (1.51)	3.59 (1.18)	0.63 (0.38)
Light Soil, Deep Column				
K-12 (/1.,0.,1./)	.15 (.12)	3.98 (1.67)	3.14 (0.94)	0.49 (0.62)
K-13 (/.75,.15,.10/)	.22 (.08)	4.47 (1.81)	3.84 (1.79)	0.89 (0.80)
K-14 (/.85,.10,.05/)	.19 (.12)	4.11 (1.97)	3.56 (1.30)	0.62 (0.55)
Heavy Soil, Shallow Column				
K-15 (/1.,0.,0./)	.20 (.19)	4.41 (1.86)	3.67 (1.57)	0.74 (0.74)
K-16 (/.75,.15,.10/)	.21 (.18)	4.45 (2.20)	3.64 (1.42)	0.80 (0.88)
K-17 (/.85,.10,.05/)	.20 (.13)	4.19 (0.99)	3.60 (1.31)	0.62 (0.55)
Heavy Soil, Deep Column				
K-18 (/1.,0.,0./)	.19 (.17)	4.18 (1.49)	3.58 (1.21)	0.61 (0.74)
K-19 (/.75,.15,.10/)	.27 (.11)	4.69 (2.19)	3.97 (1.90)	.08 (0.84)
K-20 (/.85,.10,.05/)	.24 (.17)	4.38 (1.84)	3.79 (1.41)	0.85 (0.70)

unaffected (Runs K–15 through K–17) to being rather strongly affected (Runs K–18 through K–20), the changes in the water balance variables are generally within 10% of the control.

The stronger effect is occurring in the lower layers themselves. Figs. 2.4a and b show daily values of the relative soil saturations of all three layers for the cases of light and heavy soil in a shallow soil column. As can be seen, particularly in the light soil case (Fig. 2.4a), there is a substantial drying of the middle and lowest soil layers (i.e., layers 2 and 3) when transpiration from those layers is allowed. It is interesting to note that the relative saturation of layer 1, however, is relatively unaffected by the strong changes in layers 2 and 3. The main reason for this is that while there is less of a water supply from the lower layers, there is also a reduced evaporative draw from layer 1 since it has a reduced root fraction from the Control Run.

Based on these simulations, and in the absence of root distribution data for the GISS GCM, the choice was made to use a root distribution of /.85, .10, .05/ for implementation into the GISS GCM (described in Chapter III). The severe drying of lower soil layers found with larger fractions of roots in lower soil layers is regarded as unrealistic for most settings.

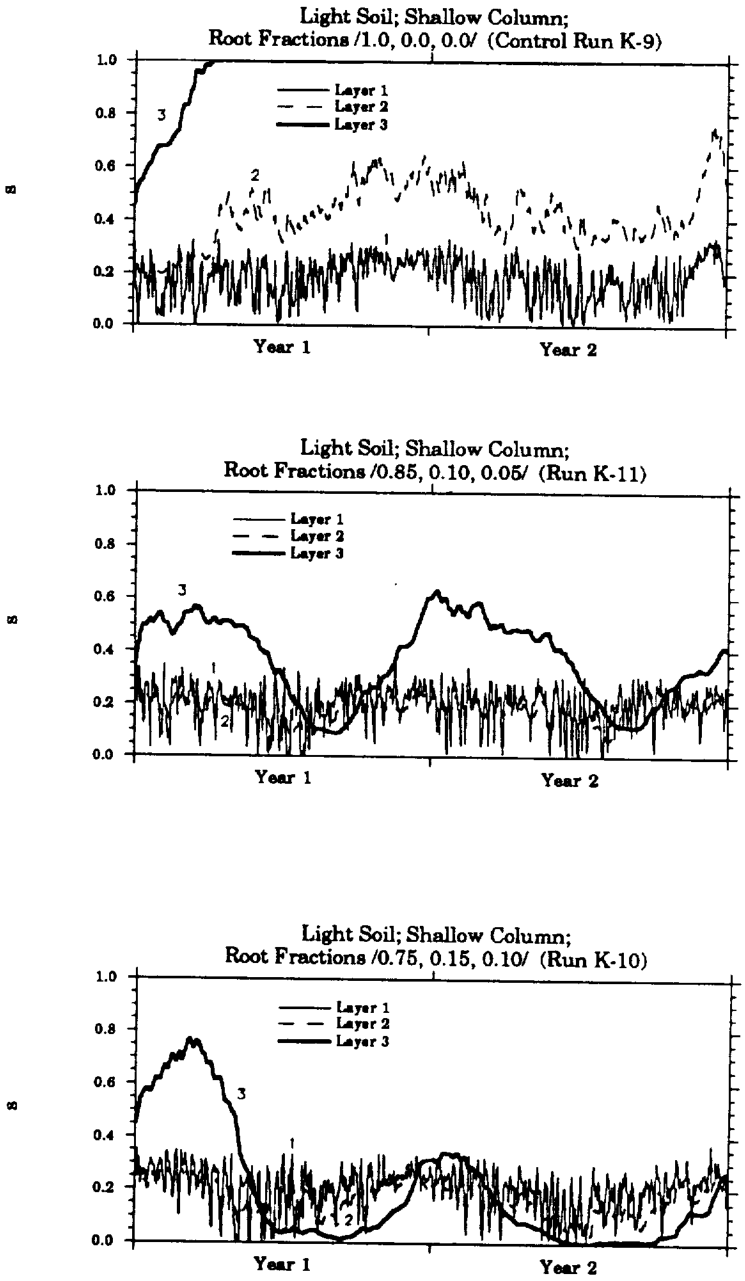

Figure 2.4a Daily 3–layer relative soil saturations for the case of light soil and shallow soil column for root distributions of /1.0, 0.0, 0.0/ (top), /0.85, 0.10, 0.05/ (middle), and /0.75, 0.15, 0.10/ (bottom)

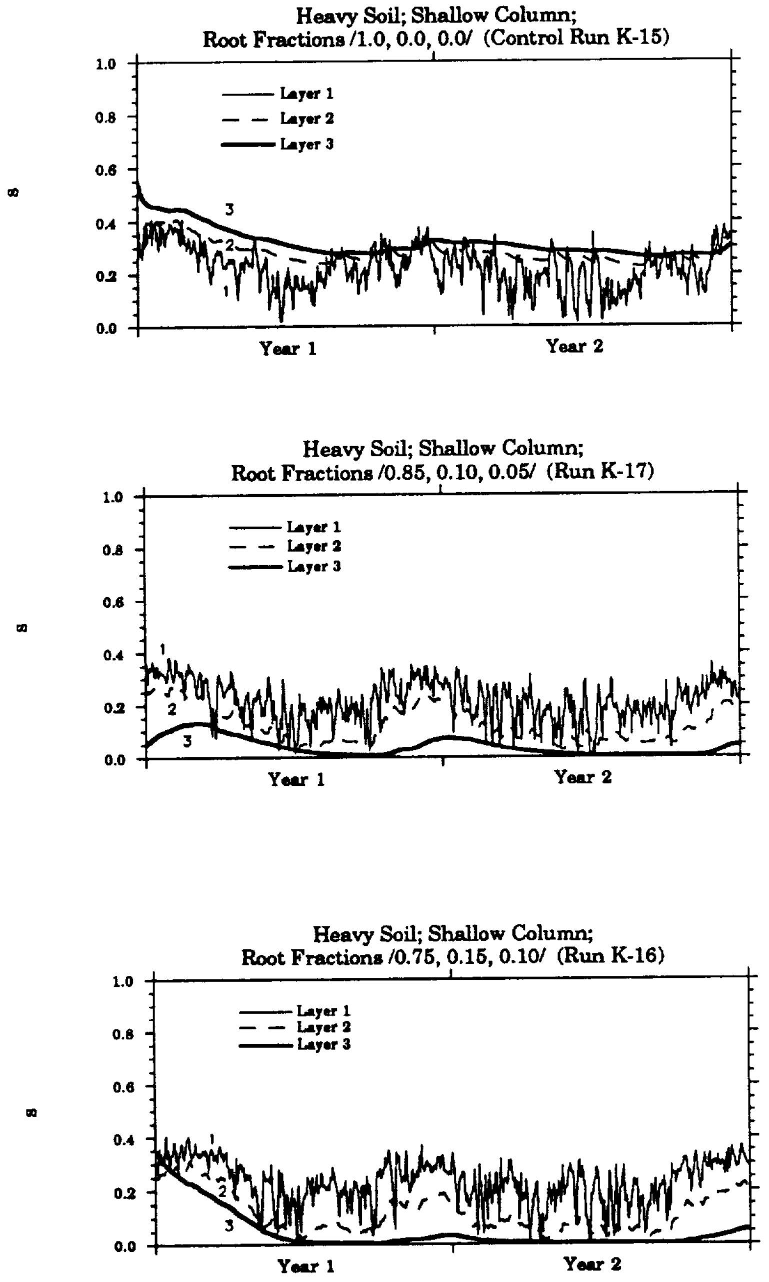

Figure 2.4b Daily 3–layer relative soil saturations for the case of heavy soil and shallow soil column for root distributions of /1.0, 0.0, 0.0/ (top), /0.85, 0.10, 0.05/ (middle), and /0.75, 0.15, 0.10/ (bottom)

C. Discussion

This chapter has essentially been a set of screening simulations in preparation for the implementation of the spatial variability hydrological parameterization of Entekhabi and Eagleson (1989a) and the soil moisture diffusion scheme of Abramopoulos et al. (1988) into the GISS GCM. Based on the results of Part II.B.1 the upper two soil layers will be kept constant for all grids with layer 1 thickness 10 cm and layer 2 thickness 15 cm. The lowest layer thickness will then be adjusted to give a consistent total soil storage capacity with that used in the current GISS GCM. Layer 3 thickness will be set such that the total field capacity of the new soil column, based on its porosity, will be equal to the field capacity in GISS Model II.

The results of the groundwater percolation simulations in part II.B.2 showed significant runoff sensitivity only for cases of light soil where the hydraulic conductivities are generally high. In the absence of a means for obtaining representative terrain slope information, the simulations in the GISS GCM will use the no–flux lower boundary condition.

Finally, due to the lack of reliable plant root distribution observations, it has been determined that a distribution of /.85, .10, .05/ yields realistic results and it will be used in the GISS GCM experiments of the following Chapter.

Chapter III.
Numerical Experiments in the GISS GCM

A. Introduction

1. Overview of the Numeric Experiments

The goal of the effort described thus far is an improved hydrologic scheme whose utility may be demonstrated in a three-dimensional GCM. As explained in Chapter I, the current empirical relations in the GISS GCM hydrologic parameterization are not physically-based. An area of improvement for this GCM would be to introduce more realistic expressions for land surface hydrologic fluxes such as those proposed by Entekhabi and Eagleson (1989a). Their scheme introduces subgrid-scale spatial variability for some key parameters and derives physically-based expressions for the grid-average rates of runoff and evapotranspiration. Furthermore, the improved GCM land surface hydrology scheme would also require a more realistic soil moisture storage and diffusion scheme in order to realistically account for seasonal cycles in surface water and heat balance. For this purpose we include the soil moisture diffusion scheme of Abramopoulos et al. (1988) alongside the landsurface parameterization of Entekhabi and Eagleson (1989a).

The implementation of the new schemes into the GISS GCM is performed in a step-wise fashion in order to isolate the marginal changes due to each scheme. Four simulations with the three-dimensional GISS GCM will be compared as listed in Table 3.1. The numerical experiments will use the 8 × 10 degree GISS GCM with fixed sea-surface temperatures based on climate values. Run G-0 is the control case and its diagnostics are collected for a three-year period. Run G-1 differs from G-0 only due to the

Table 3.1 **Simulations performed in the GISS GCM.**

Simulation Name	Description
G–0	GISS Model II as described in Hansen et al. (1983) using 8 × 10 degree grid resolution and fixed ocean temperatures (Control Run).
G–1	Same as G–0, except for new formulation of runoff coefficient R, bare soil, evaporation efficiencies, β_s, and transpiration efficiency, β_v (after Entekhabi and Eagleson, 1989a). Fractional wetting parameter κ set equal to 1.0 for large scale supersaturation rainfall and 0.6 for moist–convective rainfall. (Abbreviated "space")
G–2	Same as G–1, except new soil moisture diffusion scheme of Abramopoulos et al. (1988) is used with transpiration from lower layers. No instantaneous upward diffusion or prescribed growing season as in GISS II. (Abbreviated "space/soil")
G–3	Same as G–2, except fractional wetting parameter κ for moist–convective rainfall set to 0.15 (Abbreviated "space/soil/storm")

replacement of the Hansen et al. (1983) empirical runoff and evapotranspiration efficiency functions with the Entekhabi and Eagleson (1989a) expressions. Run G–2 is further modified to include the Abramopoulos et al. (1988) soil moisture diffusion scheme. The final simulation experiment G–3 differs from G–2 only by changes in one parameter that defines the spatial fractional wetting in the subgrid parameterization for runoff generation.

The diagnostics collected for each run in addition to those standard for the GISS–II model include:

a) For all grids; monthly values of potential evaporation, evaporation over earth, runoff produced by snowmelt, no–rain probability, percentage of rainfall which is of moist–convective origin, number of independent storm events, mean storm duration, mean interstorm duration, and mean storm depth,

b) For selected regions; daily values of precipitation, evaporation, surface temperature, and relative surface soil saturation,

and c) For three selected United States grids; hourly precipitation records.

Initial conditions for each of the simulations are taken from the standard GISS Model II 8° × 10° Run as described in Hansen et al. (1983).

2. Model Boundary Conditions of the Landsurface

The GISS–II GCM landsurface boundary conditions are based on the archived 1° × 1° vegetation data set of Matthews (1983) and the archived 1° × 1° soil texture data set of Zobler and Cary (1984). Eight vegetation types were defined by Matthews, and each vegetation type was associated with a value for albedo, roughness length, "masking depth" (a variable describing the effect of vegetation on snow albedo), and field capacity. The values of the parameters used over a particular grid in the model are weighted averages based on the percentage of each vegetation type over that grid. Table 3.2 gives the values of parameters for each vegetation type.

Soil textures (given by percentage of sand, silt, and clay) are assumed to have no variation in the vertical dimension. From the soil textures, values of the soil hydraulic properties are taken as weighted averages over the three soil types. We follow Entekhabi and Eagleson (1989b) in assigning values as presented in Table 2.1.

3. Data Sets Used to Evaluate Model Performance

Simulated model climates for each of the cases (G–0 through G–3) are compared with each other and with some observed hydroclimatic variables. The sources and data quality for each of the observed data sets used in the comparisons are described below.

Comparisons will first be made of the water balance over the entire globe (divided into lumped values over the ocean and landsurface). From there, we move progressively to finer scales of resolution including zonally averaged (i.e., latitude–belt averages) values, continentally averaged values, and finally balances over major hydrologic basins. Data sets used are those of

		Desert*	Tundra	Grass	Shrub	Woodland	Dediduous	Evergreen	Rainforest
Visual albedo	Winter	0.35	0.07	0.09	0.09	0.08	0.10	0.07	0.06
	Spring	0.35	0.06	0.10	0.10	0.07	0.05	0.07	0.06
	Summer	0.35	0.08	0.09	0.14	0.08	0.06	0.08	0.06
	Autumn	0.35	0.08	0.09	0.11	0.06	0.05	0.06	0.06
Near-IR albedo	Winter	0.35	0.20	0.27	0.27	0.23	0.30	0.20	0.18
	Spring	0.35	0.21	0.35	0.30	0.24	0.22	0.20	0.18
	Summer	0.35	0.30	0.36	0.42	0.30	0.29	0.25	0.18
	Autumn	0.35	0.25	0.31	0.33	0.20	0.22	0.18	0.18
Field Capacity (g/m)	Layer 1	10	30	30	30	30	30	30	200
	Layer 2	10	200	200	300	300	450	450	450
Masking Depth (m)		0.1	0.2	0.2	0.5	2	5	10	25
Roughness Length (m)		0.005	0.01	0.01	0.018	0.32	1	1	2
Wilting Point (10^2 kPa)		----	-30	-22	-20	-20	-20	-20	-15

* Desert albedo is reduced by a factor of (1 - 0.5 s_1)

Table 3.2 Vegetation boundary conditions of GISS Model II
All values derived from Hansen et al. (1983) except for the wilting level values which are based on Entekhabi and Eagleson (1989a)

Budyko (1978) for global hydrologic balance, Zubenok (1970) for zonally averaged balance over landsurfaces, Henning (1990) for balance over continents, and Russell and Miller (1990) for major river basin water balances.

Further comparisons include the seasonal distribution of surface air temperature and precipitation over the earth. January and July mean surface air temperature data from Washington and Meehl (1984) are used, as well as December–January–February (DJF) and June–July–August (JJA) mean precipitation data from Schutz and Gates (1971).

Finally, we consider precipitation regime comparisons for gridded data from the National Center for Atmospheric Research (Sprangler and Jenne, 1988), and rainfall frequency comparisons based on hourly station data over the U.S. from the National Climate Center data set. As a check on the heat balance, we also compare zonally averaged temperatures over landsurfaces to the data of Legates and Willmott (1990).

Whereas comparisons of the GISS Model climate against observed data have in the past been done over the entire globe, the comparisons performed here will concentrate on the landsurface only. Comparisons of this sort are vital to the validation of parameterizations such as those generating runoff and evaporation over the landsurface since in global comparisons that include land and ocean, the behavior of the oceans can obscure the dynamics of the landsurface. A case example is evaporation; the zonally–averaged evaporation rate is dominated by the ocean evaporation rate at many latitudes. When the GCM is characterized by seasonally–fixed ocean temperatures, this diagnostic is a poor indicator of model performance, especially over land grids.

Data sets whose goal is to provide global coverage often have poor quality in regions where observation stations are sparse. Also, in the case of zonally averaged data over landsurfaces, interpretations must be made keeping in mind the percentage of a given latitude belt which is in fact landsurface and not ocean. Where this percentage is small (such as in the 40° to 60° S Latitude region in Figs. 3.18a–c) observed and simulated data must be viewed with greater caution. Throughout the comparisons we attempt to point out data quality issues such as these.

B. Implementation of the New Hydrological Parameterization into the GISS GCM: Some Off-Line Results

1 Description

Incorporation of the new hydrology schemes into the GISS GCM requires adaptation to some new details not present in the screening model used in Chapter II. In this section, the manner in which the Entekhabi and Eagleson (1989a) and Abramopoulos et al. (1988) schemes were incorporated into the GISS GCM are outlined. A few off-line (outside of the GCM) sensitivities are also analyzed by assuming typical forcing for each of the schemes. These off-line tests are important indicators of expected model sensitivities.

a. Runoff Ratio and Evapotranspiration Efficiency. Precipitation is generated in two forms over the grid square: moist convective rainfall and large-scale supersaturation rainfall. We have taken their occurrences to be spatially independent for any given time step in the model. Given an amount of each type of rainfall, we use Equation (1.16) to obtain a runoff coefficient for the moist convective event, R_{mc}, and for the supersaturation event, R_{ss}.

With precipitation intensities P_{mc} and P_{ss}, we obtain the total runoff Q as

$$Q = \text{MAX}\ [P_{mc}R_{mc} + P_{ss}R_{ss}, \text{ soil moisture capacity exceedance}] \tag{3.1}$$

The new parameterization must also accommodate the effects of freezing temperatures. Specifically, snowmelt runoff and ice in the soil column need to be addressed. The current GISS parameterization treats snowmelt runoff identically to rainfall runoff. We choose to deal with snowmelt runoff in two ways. In Run G–1 we allow no runoff from snowmelt except when the field capacity is exceeded. In Runs G–2 and G–3 we treat it in the same way as supersaturation rainfall, i.e., snow coverage is over the entire grid. For the case of G–1, we see runoff volumes in high latitudes generally peak higher in spring thaw than in the control case. This is because any snowmelt during the winter remains stored in the ground until the capacity is filled.

Ice in the soil column is treated as follows: it contributes to the relative soil saturation used to formulate both the runoff coefficient and evaporation efficiency, but is not allowed to diffuse in the soil. Sublimation from the surface layer is allowed in this parameterization.

The GISS GCM has eight vegetation–type designations, and each grid has eight values delineating the fraction of each type within the grid. As we have mentioned earlier, Table 3.2 gives values of parameters associated with each vegetation type (all values except wilting point values are from Hansen et al., 1983). The evaporation efficiency is calculated as a weighted average of that obtained over bare soil and vegetated fractions, the vegetated fraction evapotranspiration efficiency itself being a weighted average taken using all values of the wilting point. Soil hydraulic properties for the sand, silt and clay classes correspond to those of Table 2.1.

The fractional wetting parameter κ (representing the fraction of the grid square actually wetted by a precipitation event) exerts a strong influence in the spatial variability parameterization of runoff as seen in Figs. 3.1a–e. Unfortunately there is no simple method for the determination of a proper value of κ for use in GCMs. In nature, κ would have a complicated seasonal and geographical dependence on regional climate and may be subject to various scales of spatial and temporal variability. To provide reasonable estimates for κ we reduce the complexity of the conceptual model to one simply involving storms over grid squares.

Within an individual grid square, there are at least three scales of spatial variation to consider. First, there is the size of a typical storm area relative to GCM grid area. For large scale supersaturation events these two may be similar; moist–convective storms, however, would generally be much smaller in area than the entire grid square. Second, there is the fraction within the storm itself which is actually wetted by rainfall (e.g., there are generally rain–free gaps in meso–scale storm bands). Observational analysis of air mass thunderstorms over Arizona and the Sudan (Eagleson, 1987; Eagleson, 1984) suggests this value may be roughly 0.60 in the mean for moist–convective events. Third, there is the relative location of storms within the grid square. To reflect the spatial variability of storm location, storms may be modeled as only partially covering a grid square (see Eagleson and Wang, 1985). The value of κ, then, ought to be determined based on factors related to these interactions.

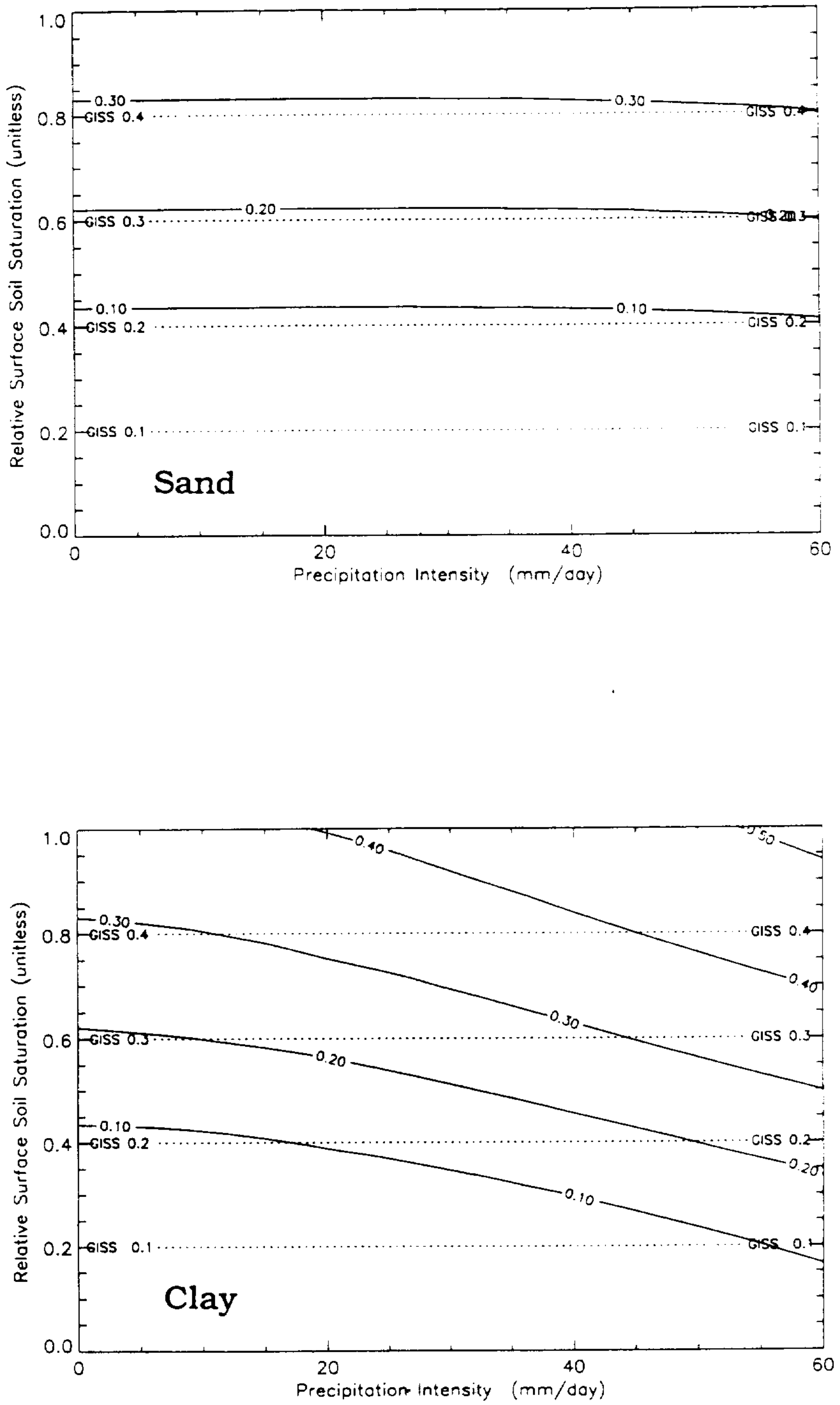

Figure 3.1a Runoff coefficient R for $\kappa = 1.0$, çv = 1.0, sand (top) and clay (bottom) for typical ranges of soil moisture and precipitation intensity

Solid lines = R (spatial variability parameterization)

Dotted lines = R (GISS parameterization)

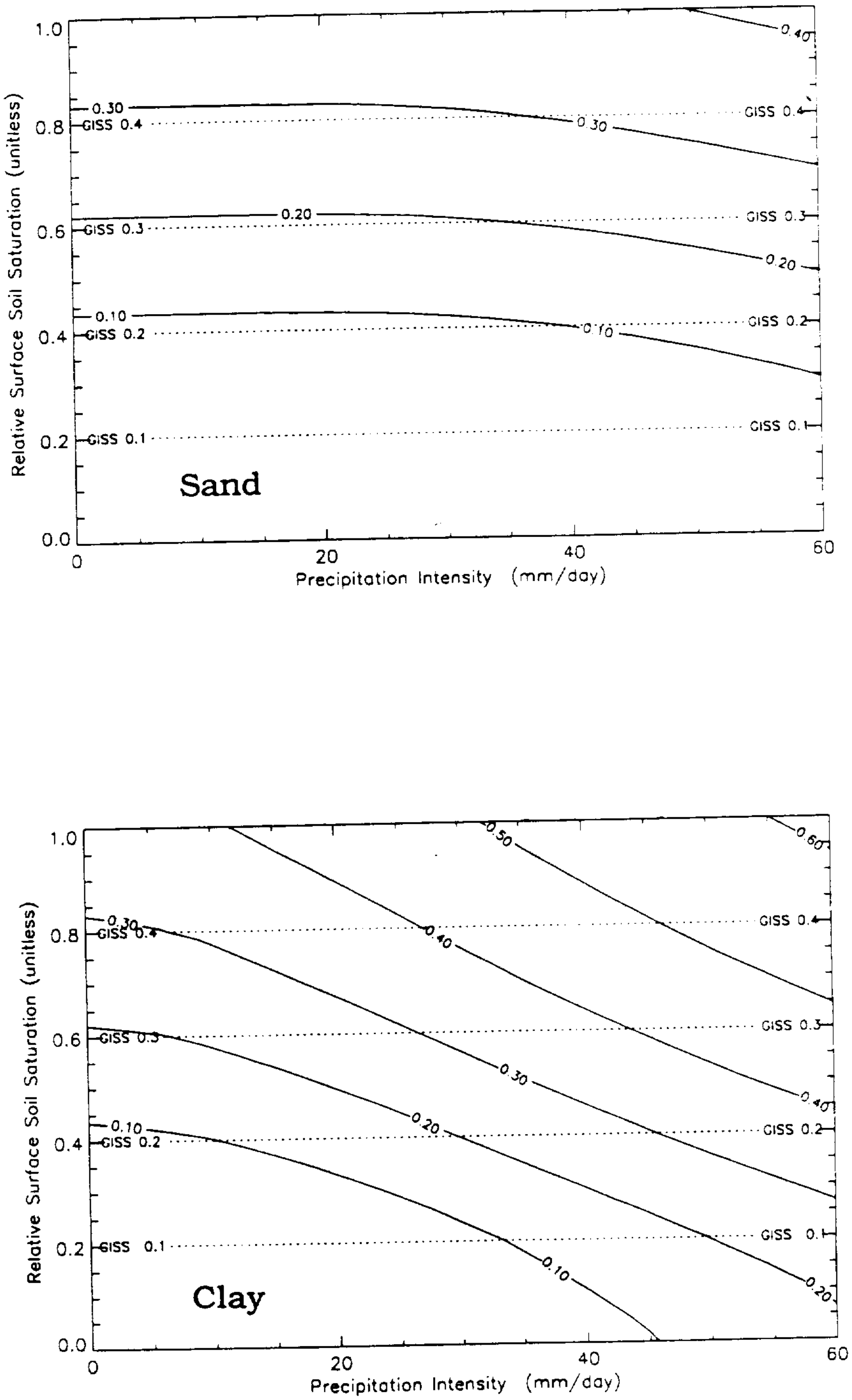

Figure 3.1b Runoff coefficient R for $\kappa = 0.6$, $cv = 1.0$, sand (top) and clay (bottom) for typical ranges of soil moisture and precipitation intensity

Solid lines = R (spatial variability parameterization)

Dotted lines = R (GISS parameterization)

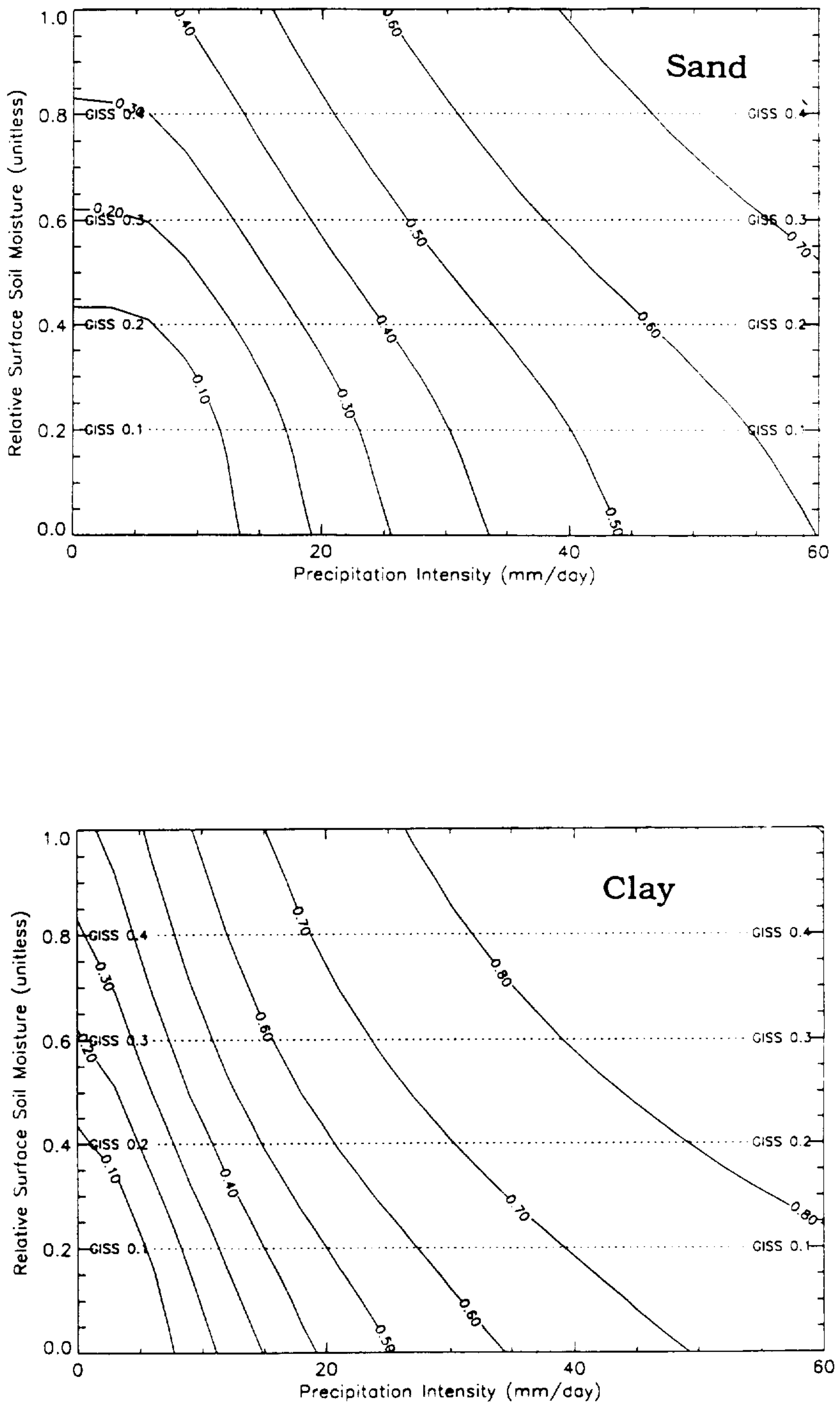

Figure 3.1c Runoff coefficient R for $\kappa = 0.1$, $cv = 1.0$, sand (top) and clay (bottom) for typical ranges of soil moisture and precipitation intensity

Solid lines = R (spatial variability parameterization)

Dotted lines = R (GISS parameterization)

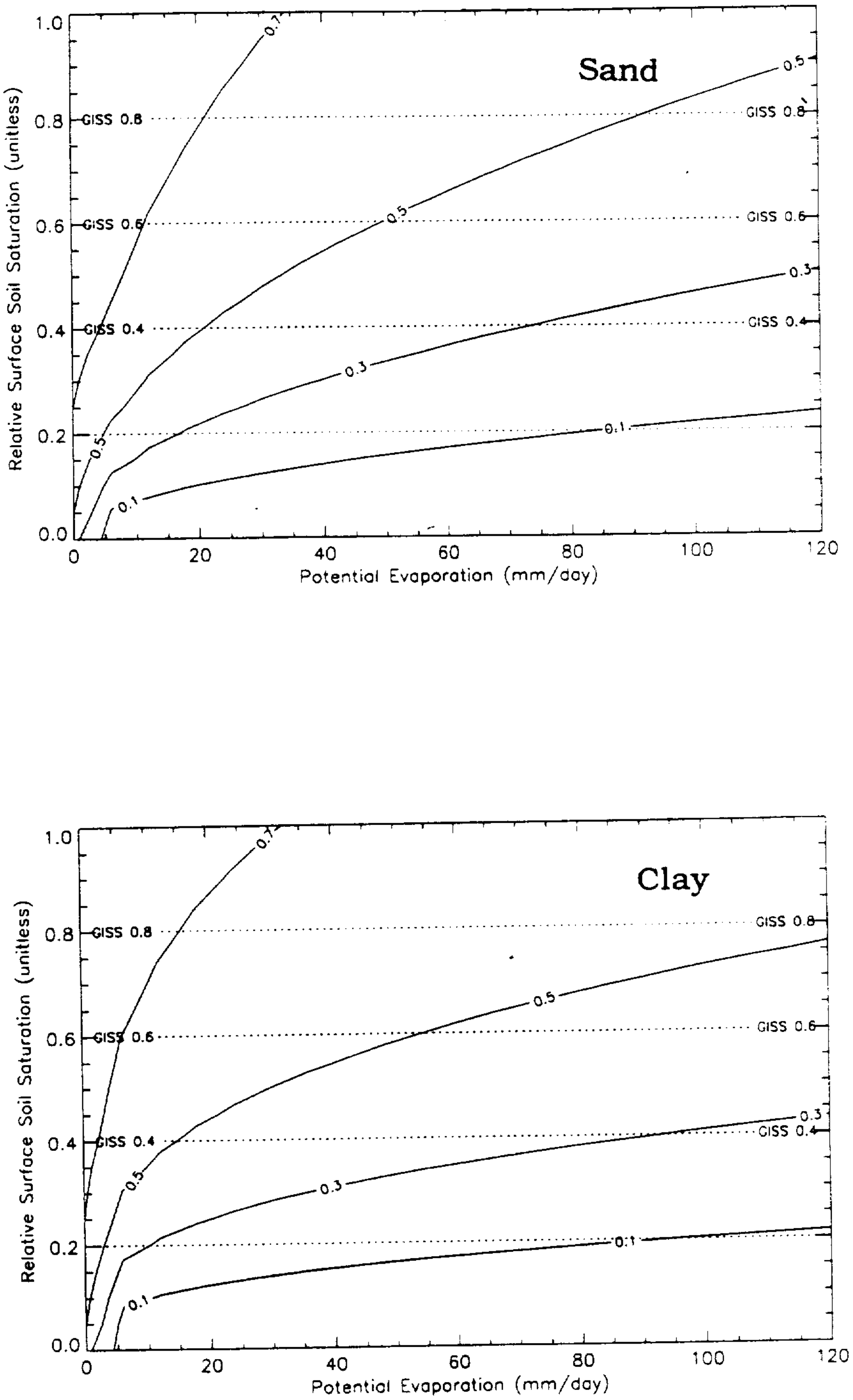

Figure 3.1d Bare soil evaporation efficiency β_s for $cv = 1.0$, sand (top) and clay (bottom) for a typical range of potential evaporation
Solid lines = β_S(spatial variability parameterization)
Dotted lines = β_S (GISS parameterization)

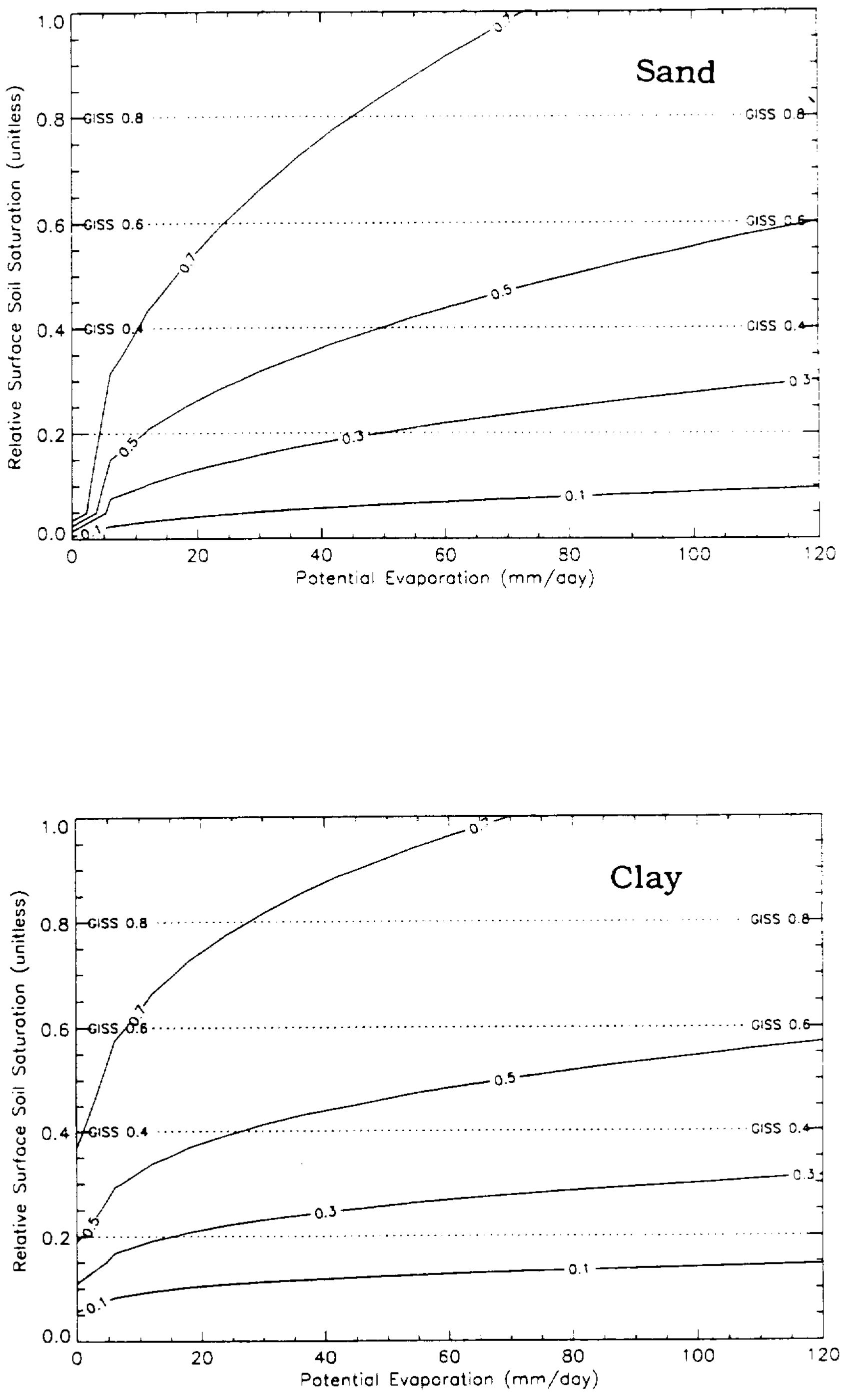

Figure 3.1e Vegetated soil transpiration efficiency β_V for $cv = 1.0$, sand (top) and clay (bottom) for a typical range of potential evaporation. The wilting pressure is taken as $\psi = -15$ bars

Solid lines = β_V (spatial variability parameterization)
Dotted lines = β_V (GISS parameterization)

As a simple approximation, we have prescribed one value of κ for supersaturation and one value for moist–convective rainfall. Due to the large spatial scales associated with supersaturation events, a value of $\kappa = 1.0$ is used for this type of precipitation for all simulations. For moist–convective rainfall, Runs G–1 and G–2 follow Entekhabi and Eagleson (1989a) using $\kappa = 0.60$. In light of the previous discussion, however, it is possible that κ ought to be set at a much lower value. To test this sensitivity, κ for moist–convective rainfall is set to 0.15 in Run G–3.

One final point is that for Kuo–type moist–convection parameterizations (not used in GISS Model II), the fraction of the grid square experiencing convection is a variable that depends on boundary layer properties. The landsurface hydrologic parameter κ may thus be tied to and coupled with the moist–convective parameterization if the Kuo–scheme is used in the GCM.

The contour plots of runoff ratio and evaporation efficiency reveal major differences between the linear relationships in the current GISS–II formulation (which has dependence on relative soil moisture alone) and the new spatial variability formulation (which has nonlinear dependence on relative soil saturation, precipitation intensity [in the case of runoff coefficient] and potential evaporation [in the case of evaporation efficiency]).

The nonlinear dependence of the runoff coefficient on precipitation intensity is of importance. In Figs. 3.1a–c for a given soil saturation, the new parameterization generally gives a lower value of R for low intensity rainfall than the GISS formulation. However, as precipitation intensity increases at this soil saturation, the new formulation for R exceeds the GISS value. This nonlinear dependence is consistent with equations of infiltrability and therefore has greater physical validity than does the GISS parameterization.

The rather strong dependence of R on κ can be seen by comparing Figs 3.1a through 3.1c. The runoff ratio for the new parameterization is highly sensitive to the parameter representing fractional wetting over the grid. The effects are strongest mainly for higher values of precipitation intensity. As we will see, the bulk of the grid squares have low–intensity precipitation and the effect of the spatial variability will be small. However, many of the grids with high–intensity precipitation are tropical grids for which (the Amazon River Basin, for instance) current model runoff values are known to be low. Fig. 3.2 shows the percentage of the annual rainfall in the Control Run G–0 that is due to moist convection. As expected, the tropical regions have the highest percentage values (up to 70%) and they are hence characterized by greater rainfall intensities. In these regions the changes resulting from the new runoff parameterizations will be clearly evident and significant changes in model climate are to be expected. In these same regions, the sensitivity to the landsurface parameter κ is going to be highest as evident in Figs. 3.1a through 3.1c.

The evapotranspiration efficiency functions β_S and β_V are plotted in Figs. 3.1d and e respectively as functions of the relative soil saturation and the potential evaporation rate. These functions are most sensitive to the potential evaporation rate at low values of this variable and have reduced sensitivity at high values.

<u>b. New Three–Layer Soil Column (Runs G–2 and G–3)</u> The two–layer soil moisture diffusion scheme of the GISS GCM has major shortcomings. First, upward diffusion from layer 2 to layer 1 is restricted to a pre–defined growing season in mid and upper latitudes (Hansen et al., 1983). The second layer is provided to overcome excessive drying of layer 1 in continental regions

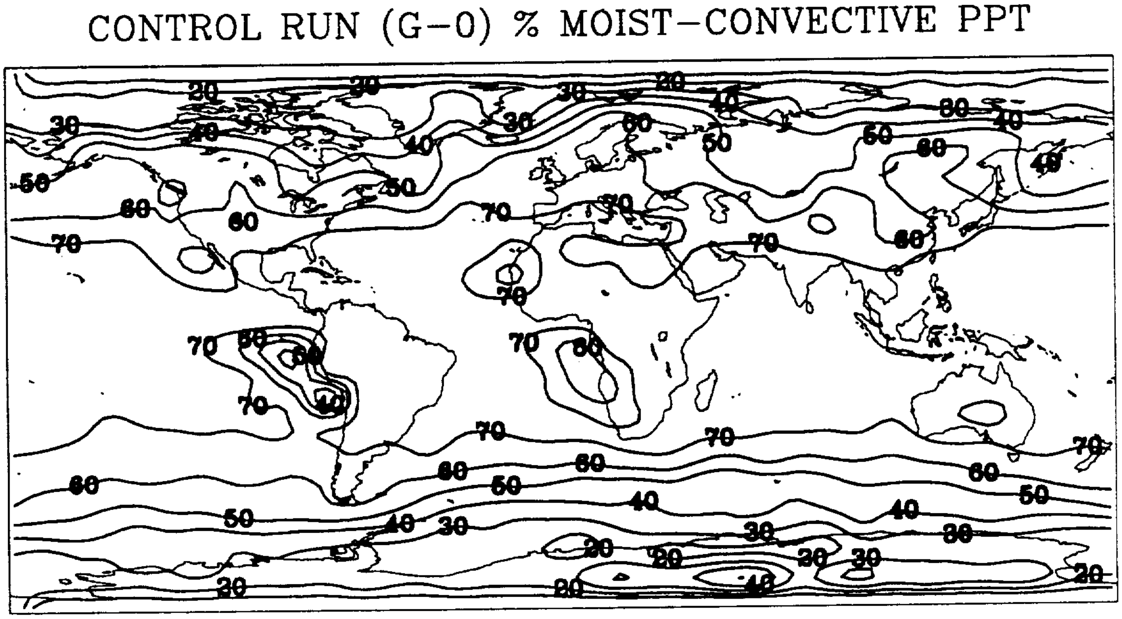

Figure 3.2. Percentage of rainfall which is of moist–convective origin in the GISS Model II Control Run

during summer. The lower layer can recharge outside the growing season and then supply its store of water to layer 1 over the summer. The simplified differential equations governing diffusion in the current GISS GCM are themselves not physically based. For example, there is an *instantaneous* equilibration of *relative soil moisture* in layers 1 and 2 for vegetated fractions of the grid when diffusion is in the upward direction. As an improvement on this, we use a three–layer soil column based on the work of Abramopoulos et al. (1988).

This scheme is a finite difference solution of the diffusion equation; we use a no–flux boundary condition at the base of the column. A flux boundary condition at the top is given by the net inflow into the soil resulting from precipitation, evaporation, and runoff. Transpiration from lower layers is performed by means of a sink term in each layer proportioned by the assumed fraction of roots in each layer. A schematic comparison of the diffusion scheme in the current GISS GCM and the one implemented here is given in Fig. 3.3.

The determination of soil layer thicknesses was in part based on the field capacities used in the GISS model. Porosities based on the weighted soil textures were used to scale the total depth of the column such that the total field capacity remained unchanged from the GISS–II GCM. However, due to the strong influence of the thicknesses of the upper layers on infiltration and desorption rates, the upper two layer thicknesses were set uniformly over the entire earth. The top layer is 10 cm and the middle layer is 15 cm. The bottom layer, then, makes up the difference such that the total field capacity remains unchanged, giving a total soil depth that varies over the earth from 50 to 225 cm. The lowest layer acts as a storage, supplying moisture to the

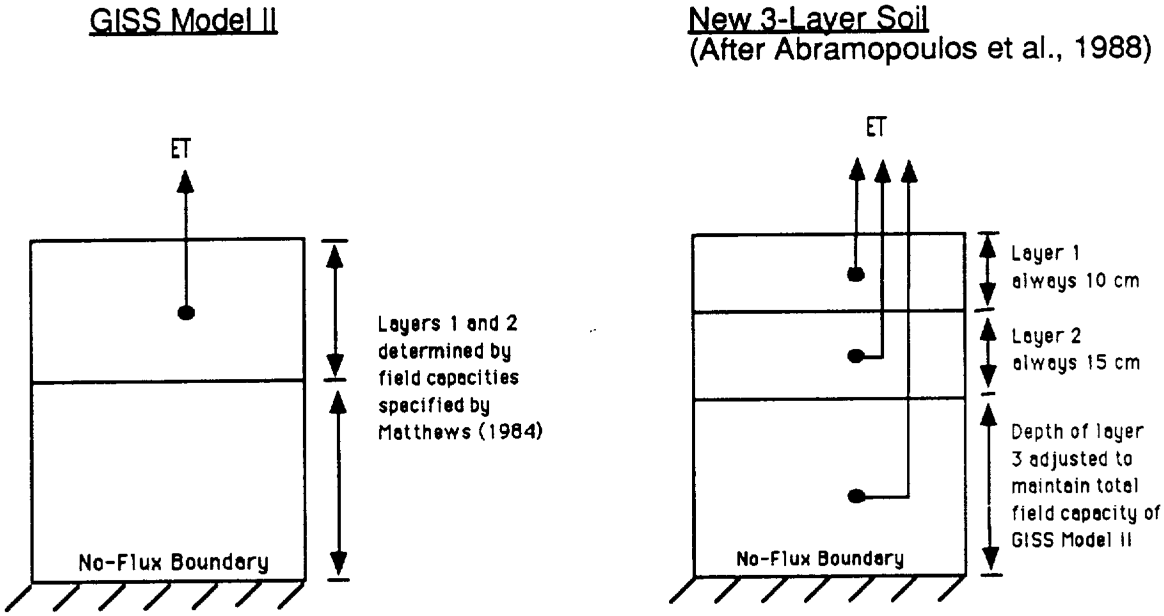

- Transpiration only from top layer
- Seasonal "on/off" toggle for exchange from lower layer to upper layer
- Instantaneous moisture equilibration for vegetated areas

- Solves diffusion equation
- Transpiration from lower layers

Figure 3.3. Comparison of new soil model to current GISS II

upper layers during dry periods. As shown by Entekhabi and Eagleson (1989b), the effectiveness of this mechanism is strongly dependent on soil texture (i.e., fractions of sand, silt, and clay). Heavier soils have a much greater ability to diffuse water upward against gravity due to high matric suction. Since this upward diffusion is replacing those features of GISS–II (i.e., prescribed growing season and instantaneous soil moisture equilibration between the two layers) designed to prevent summer desiccation, it will be of interest to examine summer continental temperatures, particularly where soil texture is composed mostly of sand.

The two–layer heat conduction of the soil column remains the same as in GISS–II. However, the thickness of the top layer is made equal to the combined depths of the top two layers in the new soil moisture diffusion scheme. The bottom layers of both heat and moisture schemes are then of equal thickness. This matching provides a convenient common flux boundary over which heat transfer by movement of water can be computed along with heat conduction. Ice in the soil column contributes to relative soil saturation, but remains fixed in its soil layer of origin.

In nature, the fraction of roots in different soil layers is dependent on many parameters including plant type, soil texture, and climatic region. It is not the purpose here to provide a full treatment of plant physiology in this parameterization. Rather, we sought to give a means of extracting water from lower soil layers to give a simple approximation to the function of plants in regional hydrologic balance. Based on observations compiled by Epstein (1973), it seems reasonable that for many plants, the root density in the soil decreases exponentially with depth. Seeking to find a reasonable value for root densities, the Screening Model was utilized to test sensitivity to various weighting schemes. A weighting of 85% of plant roots in the top layer, 10% in the second, and 5% in the lowest layer was concluded to be a reasonable estimate. Higher percentages in the lower layers tended to dry the lowest layer in the screening model. We set these weightings uniformly over the globe since no firm data base exists for root density.

In order to demonstrate the improvements brought about by the new soil diffusion scheme when compared with the current GISS scheme, we present the following plots of off–line sensitivity runs for three cases:

1) A fifty–day response to an initially saturated top layer and initially dry bottom layer (s) with zero flux at the surface (Fig. 3.4a);
2) A fifty–day day response to an initially saturated lower layer and initially dry top layer (s) with zero flux at the surface (Fig. 3.4b);
3) A fifty–day response to a sinusoid forcing of the top layer (an implicit sinusoid flux at the surface) (Fig. 3.4c).

A medium soil texture was used for the new soil diffusion scheme in these plots (the current GISS scheme has no dependence on soil texture). The thickness of layers follows the "nominal" thicknesses from Table 2.3 for the new soil diffusion scheme and an equivalent total thickness for the GISS diffusion scheme. Further, we are considering a vegetated area as opposed to bare soil (the vast majority of landsurface grids are predominantly vegetated).

Figs. 3.4a–c show that, in general, the GISS scheme equilibrates at a much faster rate than the new scheme (this is true for other soil types as well). In fact, in the case of upward diffusion (Fig. 3.4b) instantaneous equilibration of relative soil saturation in the GISS scheme is evident. The equilibrium state for the GISS scheme, regardless of the relative thicknesses of the two layers, is for the relative soil saturation values of all layers to be

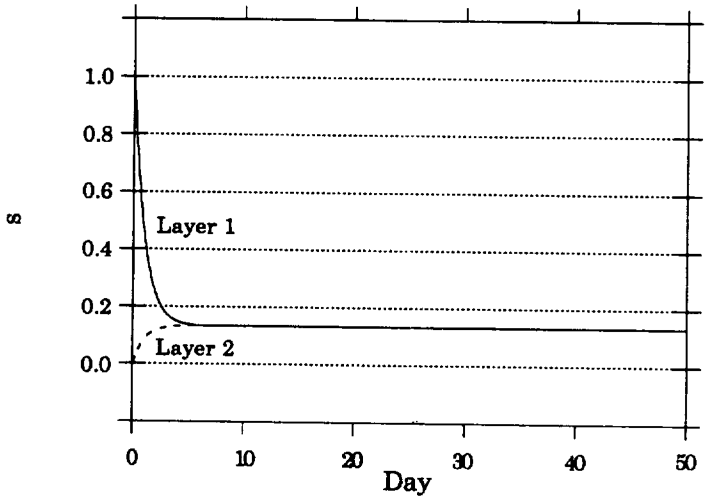

GISS Diffusion:
Top Layer Initially Saturated

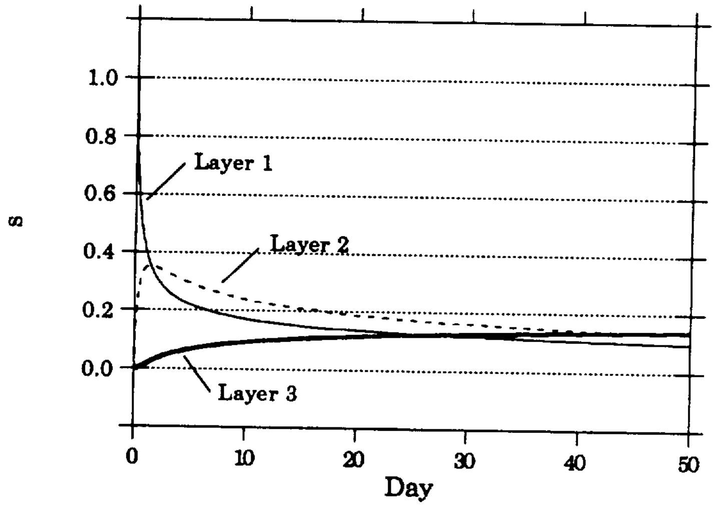

New Soil Diffusion:
Top Layer Initially Saturated

Figure 3.4a Fifty day off–line comparison of GISS (top) and New Soil Diffusion (bottom) for an initially saturated top layer and dry lower layer (New Soil Diffusion uses medium soil texture, GISS scheme has no dependence on soil texture)

GISS Diffusion:
Bottom Layer Initially Saturated

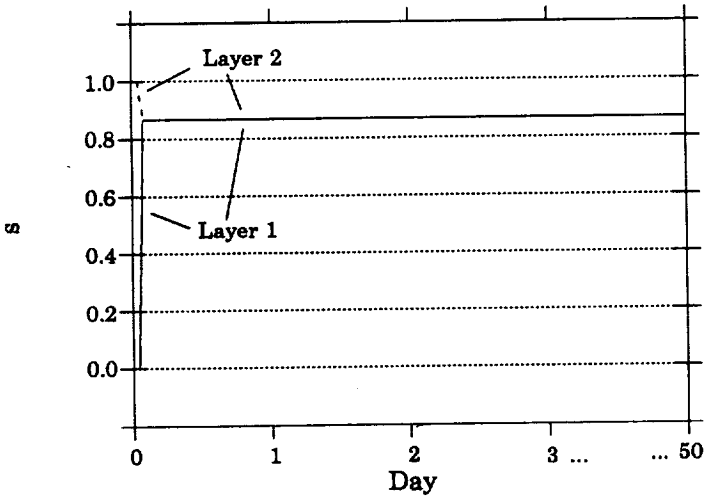

New Soil Diffusion:
Bottom Layer Initially Saturated

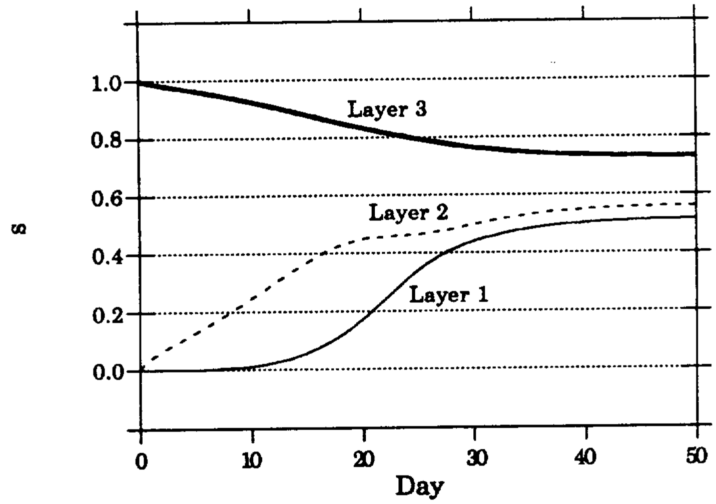

Figure 3.4b Fifty day off–line comparison of GISS (top) and New Soil Diffusion (bottom) for an initially saturated lower layer and dry upper layer (New Soil Diffusion uses medium soil texture, GISS scheme has no dependence on soil texture)

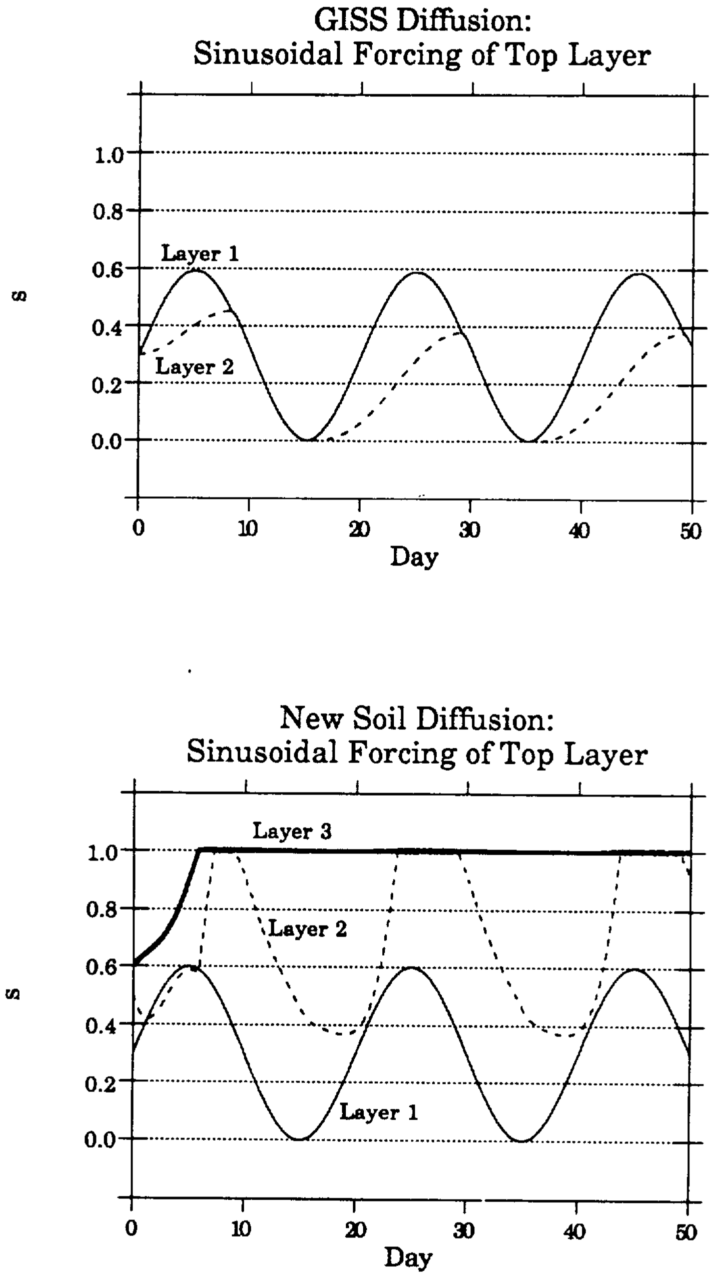

Figure 3.4c Fifty day off–line comparison of GISS (top) and New Soil Diffusion (bottom) for a sinusoidal forcing of upper layer (New Soil Diffusionuses medium soil texture; GISS scheme has no dependence on soil texture)

equal. This is unrealistic since gravity ought to be forcing a higher concentration in the lower layer(s) in the absence of other forcings. In the new soil scheme, the effects of gravity are accounted for and we see in Figs. 3.4a–c that indeed the lower layers have preferentially higher equilibrium relative saturations. Finally, in the sinusoidal forcing case particularly, we see that the response of the lowest layer to the upper layer is very dampened in the new scheme as compared to the GISS scheme. The quick response in the GISS scheme is at least to some degree a surrogate for plant transpiration. In the new scheme, transpiration by root extraction is modeled directly, although these six plots have not included these effects since it would require complications which would cloud the messages of the plots. The rate at which diffusion takes place between the layers will have significant influence on the model climate. The amplitude of the annual cycle in surface soil saturation will affect the amplitude of surface heat and moisture balances among other factors. These effects will become evident when the new Abramopoulos et al. (1988) scheme for soil moisture diffusion is implemented in the GISS–GCM model and tested along with the new landsurface hydrology parameterization with subgrid scale spatial variability.

C. Results

We have discussed so far the changes to be explored within the landsurface hydrological parameterization of the GISS GCM. From here on we discuss the results as obtained from the simulations with the three–dimensional GISS GCM II.

1. Fundamental Changes in Hydrology Over Landsurface Grid Squares

The changes induced by the new hydrology parameterization may first be seen by examination of individual landsurface grids. We consider here diagnostics of single points in space averaged over increments of time as well as distributions of diagnostics of all landsurface grids averaged over the entire simulation period. More attention is given to the results of Run G–3 (see Table 3.1) since it produced the strongest changes.

The runoff ratio (the ratio of runoff to precipitation) at a point may be averaged over time and plotted against the average relative surface soil moisture. In this way we see the actual model results which compare to the off–line analytical plots presented earlier. Fig. 3.5 shows monthly–averaged runoff ratios in both the Control Run G–0, and Run G–3 over a Central Argentina grid square. This particular grid experienced a large seasonal range of soil moisture values. It is seen that the plot for the Control Run G–0 deviates slightly from the empirical $R = \frac{1}{2}s$ line which is inherent in the model. This is due to ponding on the surface (giving a slightly higher value of R) and also to the surface storage of snow (giving a slightly lower value of R). The GISS scheme has no dependence on precipitation intensity, soil type, or spatial characteristics, but only on relative surface soil moisture.

The bottom plot of Fig. 3.5 shows the runoff ratio of the same grid square, but for Run G–3. Immediately obvious is the nonlinear relationship of R with s. High values of s result in runoff ratios reaching 0.7 in the monthly mean. The current GISS runoff parameterization would not allow such high values under any conditions except a persistently saturated surface layer. The effects of the higher runoff ratios in general have caused a higher likelihood of lower values of relative soil saturation (evident near the left of the graph).

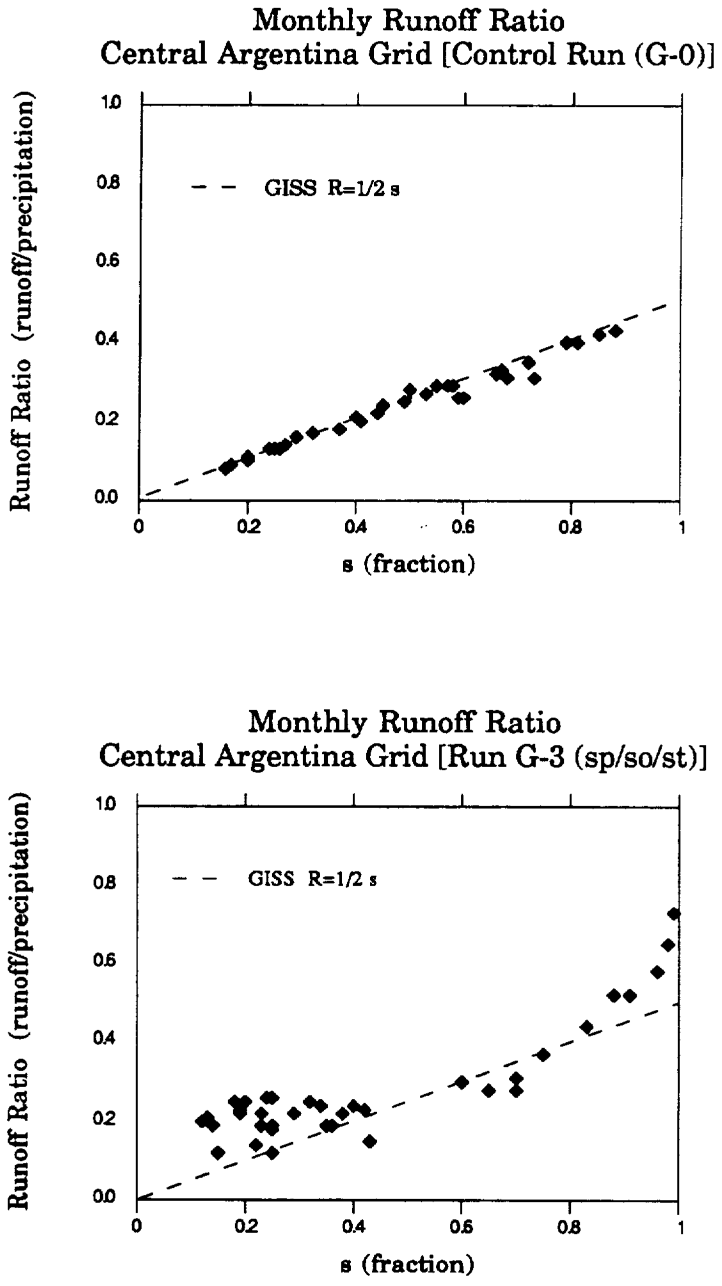

Monthly Runoff Ratio
Central Argentina Grid [Control Run (G-0)]

Monthly Runoff Ratio
Central Argentina Grid [Run G-3 (sp/so/st)]

Figure 3.5 Comparison of Control Run G–0 and Run G–3 (space/soil/storm) of the monthly runoff ratio over a Central Argentina grid (Note: Deviations from R = 1/2 s line in Control Run are due to ponding on the surface and snow storage)

Actual soil moisture data is unavailable for this region (as it is in general) and comparisons against "ground truth" are not possible. The important point is that the runoff ratio in Run G–3, with the effects of spatial variability and realistic infiltration dynamics, exhibits a nonlinear relationship with soil saturation.

When various hydrologic fluxes for all landsurface grids are plotted, patterns of direction and magnitude of changes may be seen across the globe. Figs. 3.6 through 3.8 illustrate the *difference* between the G–3 Run and Control Run of the diagnostics of runoff and evaporation, plotted against relative soil moisture and precipitation intensity. Figure 3.9 gives the distribution of soil saturation versus precipitation intensity.

Figs. 3.6 and 3.9 show that grids with low soil saturation are often characterized by high precipitation intensity as well as high runoff ratio. Since the offline plots of R (Figs. 3.1a–c) show greater sensitivity at high rainfall rates, it is expected that the largest difference between Runs G–0 and G–3 are at the low soil saturations (see Figs. 3.6 and 3.8): the strongest positive changes occurred in grids having low values of s.

When plotted against precipitation intensity (Fig. 3.7) the runoff difference shows a very clear envelope rising sharply at low intensities and leveling off as intensities exceed 25 mm/day. Based on the off–line analysis discussed earlier, one might have expected the slope of this envelope to continue to be quite steep even as the precipitation intensities became high. However, in high intensity rainfall areas, the current GISS model produces generally high soil moistures, which give rise to higher runoff. In Run G–3, these soil moistures have generally decreased, and therefore the effects of

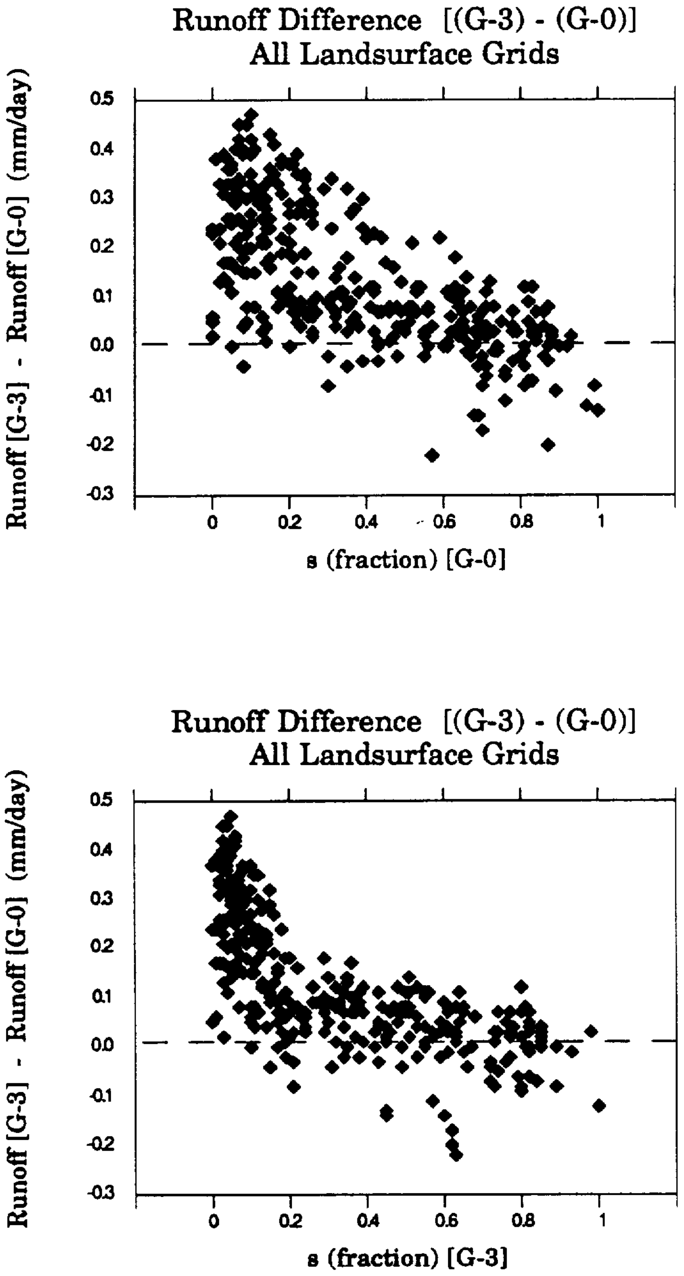

Figure 3.6 Grid–by–grid plot of the *difference* in runoff produced in Run G–3 (space/soil/storm) and the Control Run G–0, plotted against relative surface soil moisture for both cases

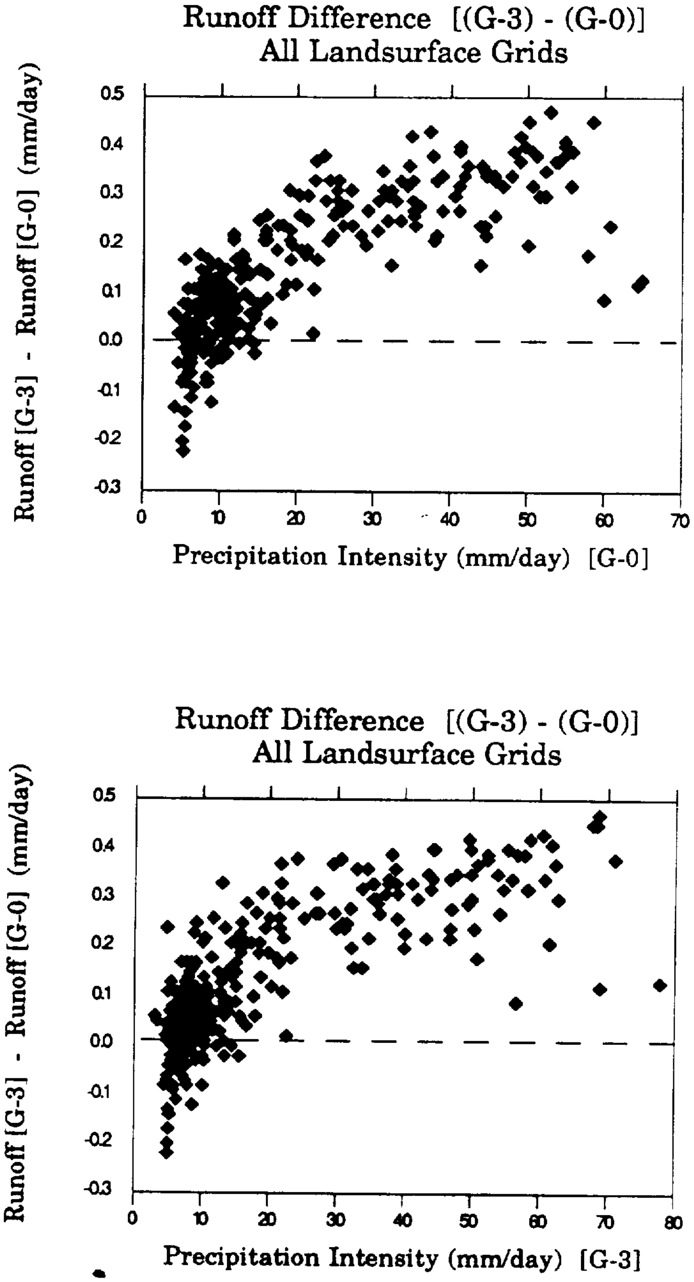

Figure 3.7 Grid–by–grid plot of the *difference* in runoff produced in Run G–3 (space/soil/storm) and the Control Run G–0, plotted against precipitation intensity for both cases

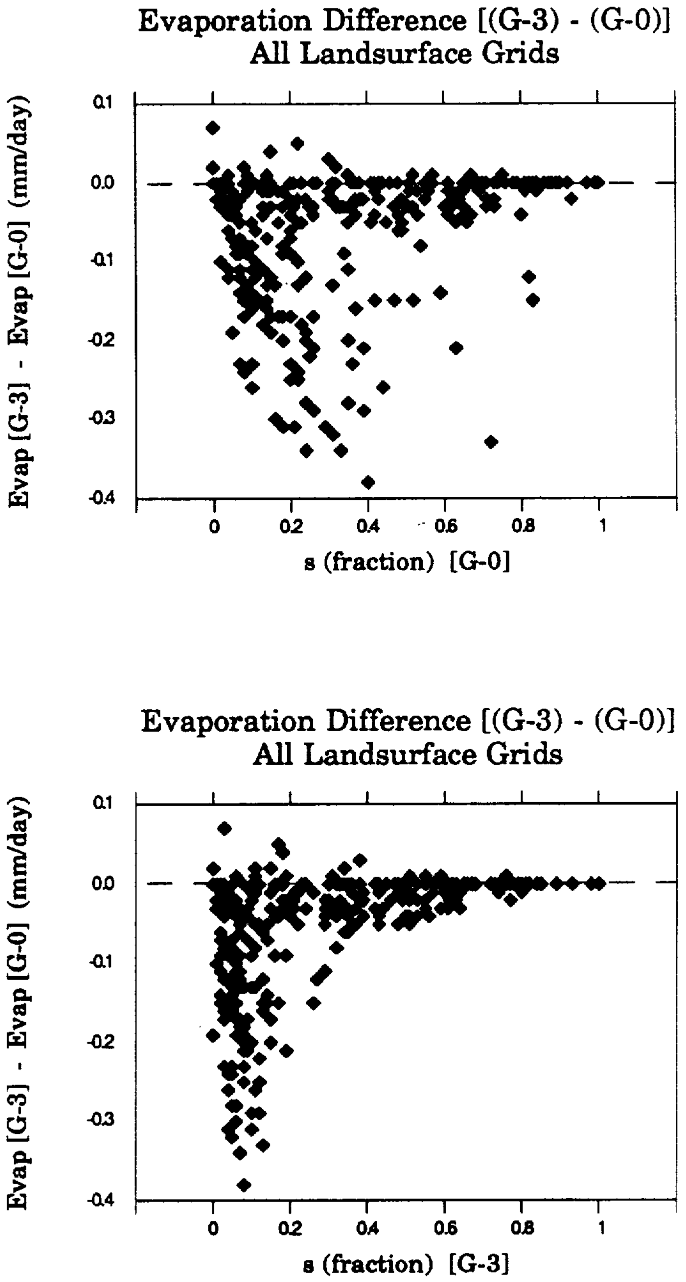

Figure 3.8. Grid–by–grid plot of the *difference* in actual evaporation produced in Run G–3 (space/soil/storm) and the Control Run G–0, plotted against relative soil saturation for both cases

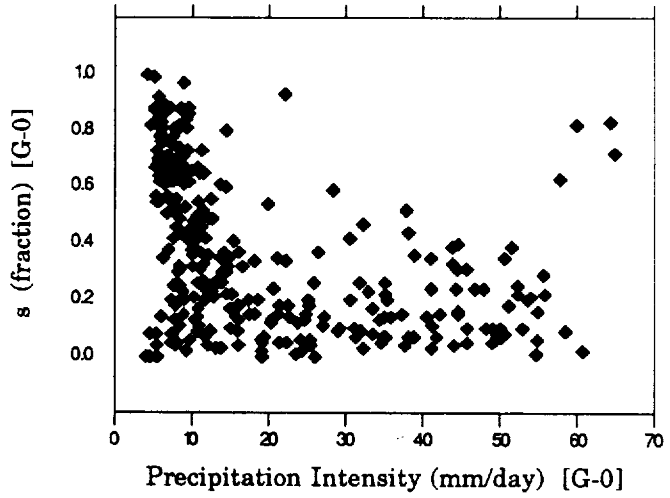

Surface Relative Soil Moisture vs. Precipitation Intensity [Control Run (G-0)]

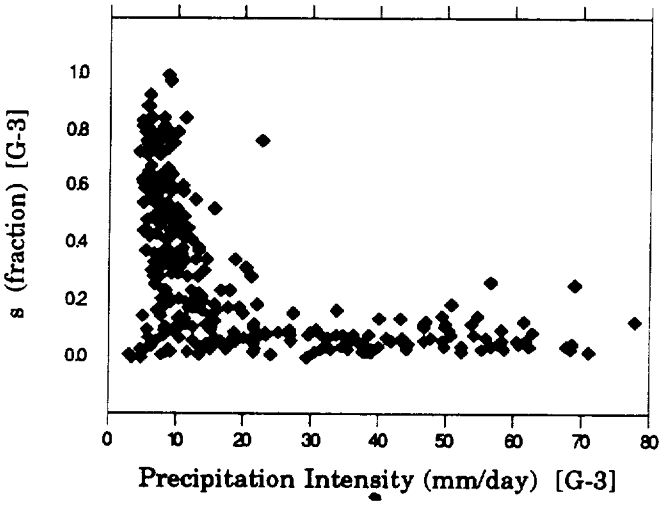

Surface Relative Soil Moisture vs. Precipitation Intensity [Run G-3 (sp/so/st)]

Figure 3.9 Distribution of relative surface soil saturation and precipitation intensity for the Control Run G–0 and Run G–3 (space/soil/storm) spatial variability, though still strong, are held in check by this negative feedback mechanism operating in high intensity rainfall regimes.

In the case of evaporation, we see in Fig. 3.8 that the strongest effects are also in grids with low relative soil saturation. Evaporation changes in Run G–3 were almost everywhere negative. This would appear to be due to the drying of soils produced by increased surface runoff. Because potential evaporation is in general extremely high (a point we shall return to later) evaporation is very efficient in both the GISS scheme and the spatial variability scheme. The main reason for the negative differences at low values of s in Fig. 3.8 is that there is simply not as much water available to evaporate since a greater portion has been lost to runoff. The underestimation of continental runoff in much of the 8° × 10° GISS GCM model is coupled with the severe overestimation of land surface evaporation in that model. Simulation Run G–3, which includes the effects of subgrid scale spatial variability on the estimation of surface hydrologic fluxes, significantly improves the model climate runoff rates over the continents; as a consequence, the remainder of the water balance and components such as the land surface evaporation rates are also improved with respect to correspondence to observations.

Next we consider the effects of the new soil moisture diffusion scheme. Figs. 3.10a–b and 3.11a–b show the time series of relative soil moistures of a Northwest U.S. grid (mainly covering Montana, chosen for the large range of soil moisture values) and an eastern Sahel grid (a dry desert area). The top soil layer (layer 1) relative soil saturation has been collected and plotted as a special daily diagnostic whereas the lower layer is the standard monthly-average diagnostic. Note that for Runs G–2 and G–3, which actually used

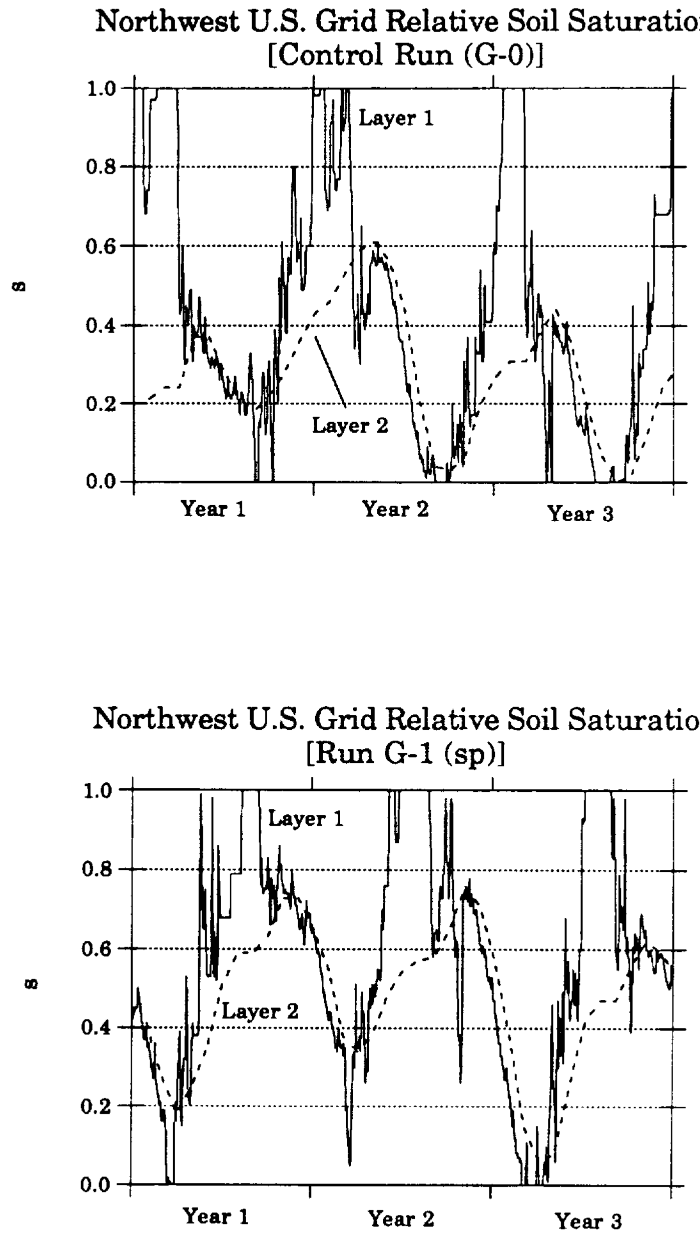

Northwest U.S. Grid Relative Soil Saturation [Control Run (G-0)]

Northwest U.S. Grid Relative Soil Saturation [Run G-1 (sp)]

Figure 3.10a Three–year plots of *daily* averaged soil saturation in layer 1 and *monthly* averaged soil saturation in layer 2 for Control Run G–0 and Run G–1 (space) over a Northwest U.S. grid

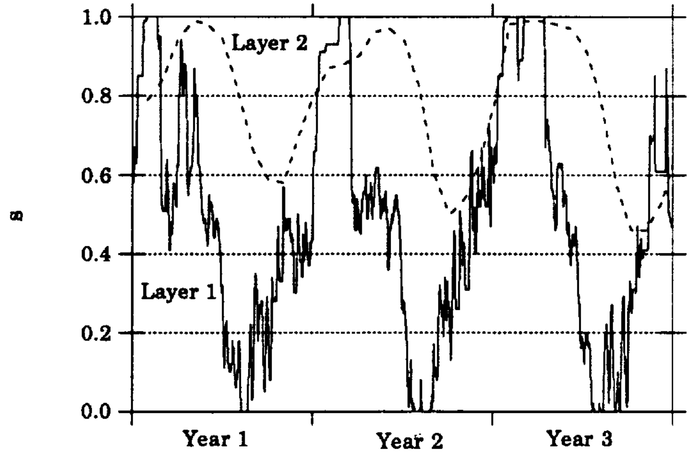

Northwest U.S. Grid Relative Soil Saturation
[Run G-2 (sp/so)]

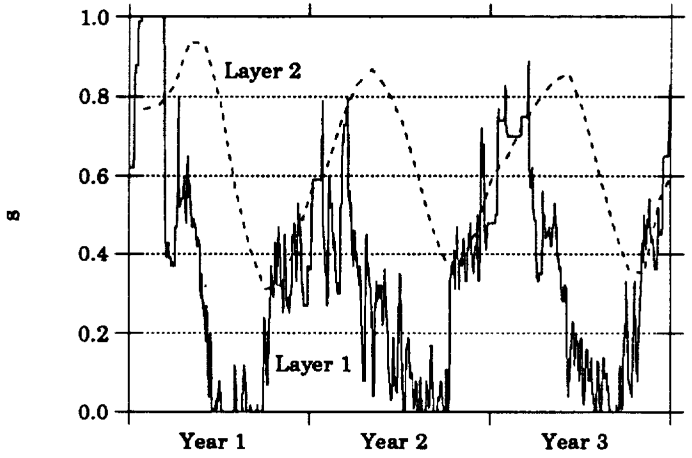

Northwest U.S. Grid Relative Soil Saturation
[Run G-3 (sp/so/st)]

Figure 3.10b Three–year plots of *daily* averaged soil saturation in layer 1 and *monthly* averaged soil saturation in Runs G–2 (space/soil) and G–3 (space/soil/storm) over a Northwest U.S. grid

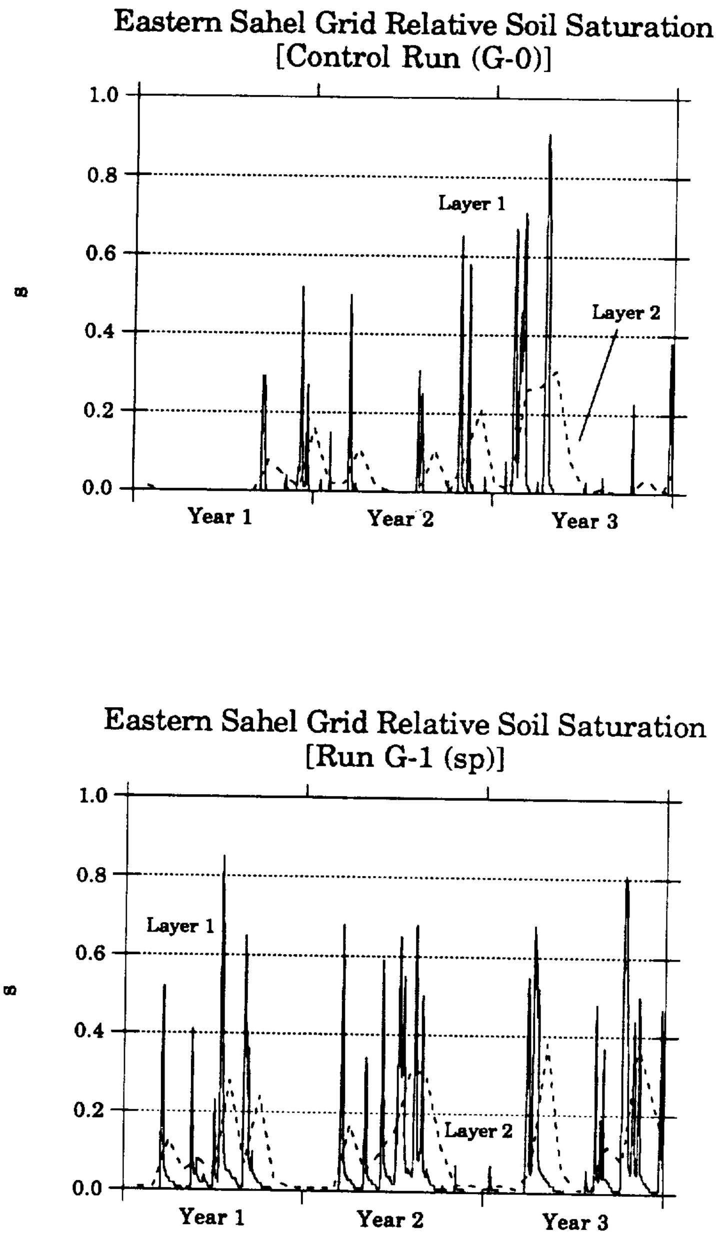

Figure 3.11a Three–year plots of *daily* averaged soil saturation in layer 1 and *monthly* averaged soil saturation in layer 2 for Control Run G–0 and Run G–1 (space) over an Eastern Sahel grid

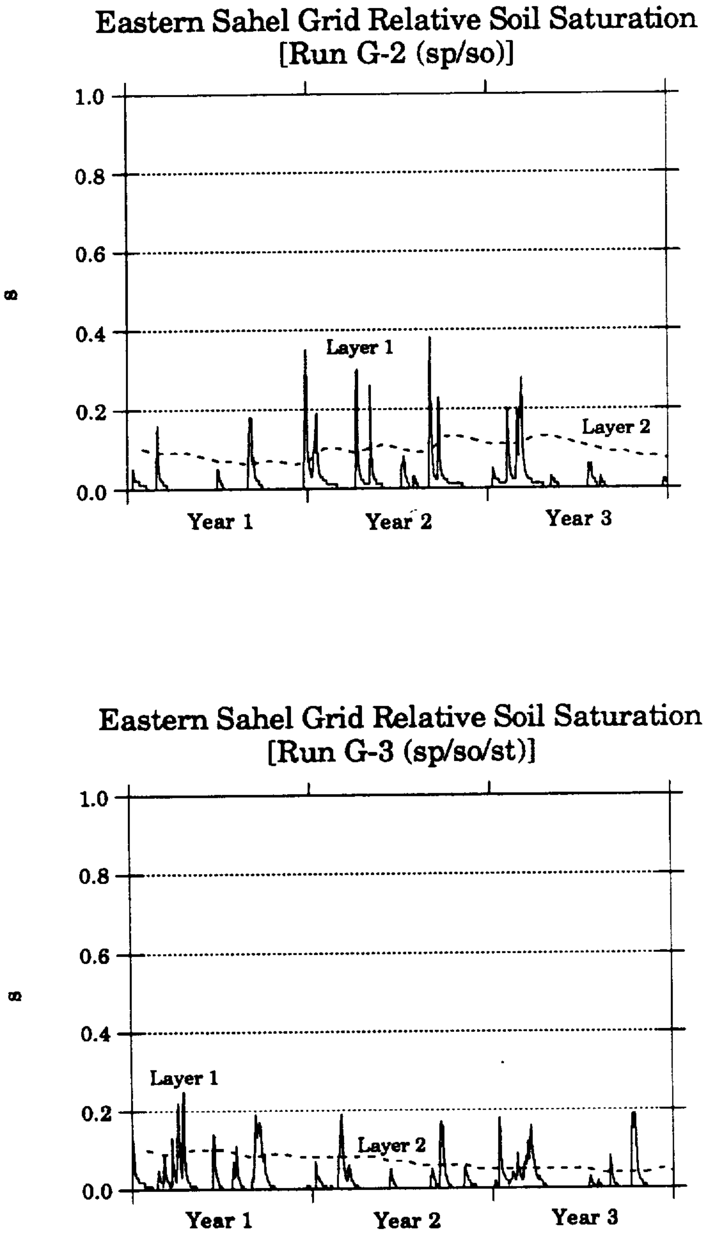

Figure 3.11b Three–year plots of *daily* averaged soil saturation in layer 1 and *monthly* averaged soil saturation in layer 2 for Run G–2 (space/soil) and G–3 (space/soil/storm) over an Eastern Sahel grid

three soil layers, the "layer 2" designation represents both layers 2 and 3. This is done for ease of comparison since the field capacity of layer 2 in the GISS scheme is roughly equivalent to the combined field capacities of layers 2 and 3 in the new 3–layer scheme.

As expected, there is only a slight change between the Control Run and Run G–1 (which retained the same GISS soil moisture diffusion) in the U.S. (Fig. 3.10a). The seasonal cycle has generally the same shape, and the seasonal range is the complete range from 0 to 1. It should be noted that the G–1 Run was started on July 1 instead of January 1, creating a half–year lag in its cycle. The G–1 Run is slightly more moist, due to a decrease in runoff in this particular grid. In both of these plots (Fig. 3.10a) we see the effects of the GISS instantaneous upward diffusion for the drying phase of layer 2 over vegetated areas. This is evident by the closeness of the drying curves of layers 1 and 2 (note the far greater independence of these curves for the wetting phases). This grid is not completely vegetated. If it were, the curves for layers 1 and 2 would match identically during the drying phase of layer 2 (as seen previously in the off–line diffusion Figs. 3.4b and c). Although not obvious from these plots, there is also a prescribed growing season for vegetated areas running from May 1 to September 1 in the Northern Hemisphere in mid– to high latitudes. Outside this time period in the GISS scheme, layer 2 soil moisture can only be increased, not depleted. Then it is allowed to supply water to layer 1 during the growing season.

For the case of Run G–2, the new 3–layer soil column is seen to yield very similar results for layer 1: the shape and magnitude of the seasonal cycle are roughly the same (Fig. 3.10b). While the amplitude of layer 2 soil moisture is also roughly the same, its mean value is about 30% higher.

Apparently the physically based equations of soil water movement are able to supply water efficiently to the point that the artificial prescribed growing season and unrealistic instantaneous upward diffusion over vegetated areas are no longer necessary. There is a much greater independence of the two layers, and there is now a consistent 1– to 2–month lag between the two cycles, whereas before there was a 1– to 2–month lag only at the peak of soil moisture (in winter) and almost no lag in the drying phase and at the low point at the end of summer.

Finally, in Run G–3 with the increased surface runoff, all three layers are consistently drier. The most significant change over the U.S. grid is the prolonged dry period in the summer months, which appears to be approximately twice as long as the dry period in the other runs.

Next we consider the eastern Sahel grid in Figs. 3.11a–b. Since this is a completely non–vegetated, low latitude grid, there are no instantaneous upward diffusion effects or growing season effects operating in the GISS scheme. Thus we see a lag in both the wetting and drying phases of the Control Run (G–0). Rain is relatively infrequent and therefore it is possible to see the intermittent pattern of completely dry soil to wet, and back to dry again from one rainfall event. In Run G–1 (Fig. 3.11a), we see first of all that the soil is more moist than the Control Run. This is a direct result of a lower runoff coefficient for light soil and low precipitation intensity (see upper plots of Figs. 3.1a and 3.1b) and also a lower bare soil evaporation efficiency. Reductions in runoff and evaporation allow for more moisture in the soil.

When the new soil diffusion scheme is incorporated (Run G–2, top of Fig. 3.11b) there is a fundamental difference: the lower layer response to changes in the upper layer is severely damped. In fact, even over long periods of time without rain the lower layer is relatively unaffected. The new runoff parameterization allows more infiltration of greater intensity rainfall events, thus the spikes of upper layer soil moisture are only half as high on average as those of the GISS soil diffusion. Interestingly, the time constants of the wetting and drying phases of the upper layer appear to be unchanged.

2. Global Hydrologic Balance

a. Globally Averaged Water Balance. We now turn to the analysis of the simulation results compared with observed data. We follow a progression from the very largest scale comparisons (globally averaged quantities) to more detailed (zonally averaged and continentally averaged quantities) and finally to mapped distributions over the earth. The mapped distributions are found in Appendix A.

The most basic picture of hydrologic performance in the model is the globally averaged hydrologic cycle. There are several sources of compiled values for the globally averaged precipitation and evaporation over the oceans and landsurface, and the exchange of moisture between those two regions (Budyko, 1963; Baumgartner and Reichel, 1975; Budyko, 1978; Henning, 1989; and others). In the long-term mean, of course, this latter exchange must equal the runoff from the land. As a comparison, we have plotted schematics of the global hydrologic balance of all simulations along with one set of observed values (Budyko, 1978) in Fig. 3.12. The values are all in annual depths [centimeters] per unit area, and the two exchange values (atmospheric divergence over land and runoff) are normalized by total landsurface area. Run G-3 is slightly out of balance due to incomplete drainage of initial storage from the landsurface. Because of this, it is expected that the runoff

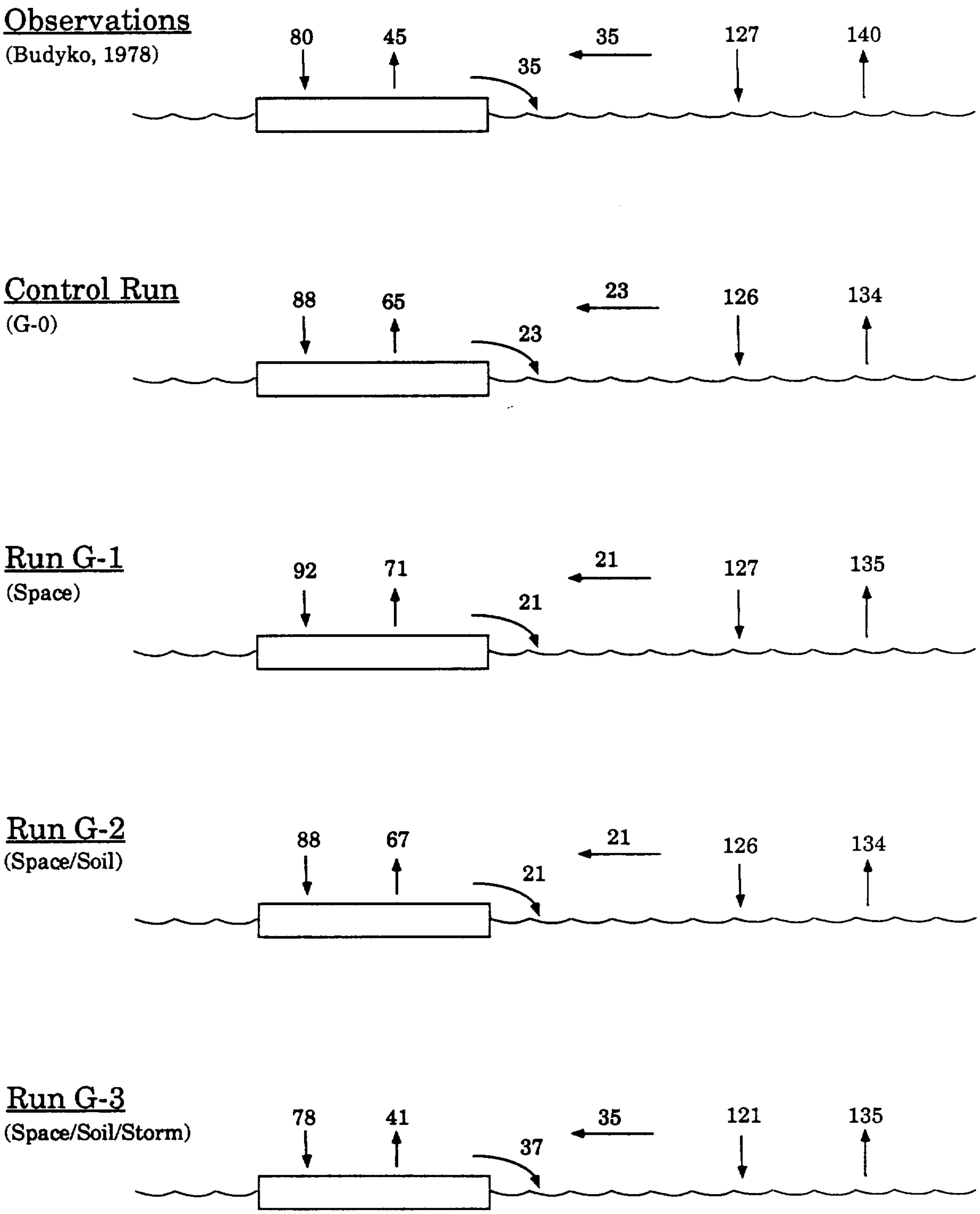

Figure 3.12. Global hydrologic balance [in cm per year] for all simulations with observations from Budyko (1978)

value in Run G–3 is slightly higher than what would result from a longer duration simulation. The ocean evaporation value is essentially constant for all runs due to the use of prescribed ocean surface temperatures.

First, we notice the GISS II model (Control Run) has underestimated runoff and overestimated both precipitation and evaporation over the landsurface (Fig. 3.12). The range of values of global landsurface runoff found by the observers cited earlier is from 27 to 35 cm annually. The GISS II value does not even fall in this range. Further, neither the GISS II precipitation over land nor evaporation over land fall into the ranges of the observers for these quantities (precipitation over land observations range from 72 to 80 cm annually whereas GISS II gives 88 cm; evaporation over land observations range from 41 to 48 cm annually whereas GISS II generates 65, roughly 50% more than observed). Similarly, Runs G–1 and G–2 grossly overestimate landsurface evaporation and underestimate runoff.

Major improvements occurred with Run G–3 (with reduced fractional wetting parameter of moist convective events; from 0.6 as in Run G–2 to 0.15). Here we see precipitation over land and evaporation over land falling to near their observed ranges. Global runoff is slightly high, but as mentioned earlier the runoff value will likely decrease as soil storages are depleted to their equilibrium states. Agreement with the Budyko (1978) values is remarkable. It is interesting to note the effects of the landsurface hydrology on the precipitation over oceans. The lower ocean precipitation value, while lower than Budyko (1978), is still well within the range of the other observers (105–127 cm annually).

Inside the schematic landsurface boxes in Fig. 3.17 is the average landsurface temperature. Observed values are derived from Legates and Willmott (1990). In Hansen et al. (1983) it was noted that summertime temperatures over continents were 2–3° C too cool in GISS II. As can be seen in the schematic, landsurface temperatures rose 0.7° C on average in Run G–3. As will be seen on the global temperature maps, this warming occurred mainly in the tropics over the Amazon, Central America and the Caribbean as well as North Africa in June–July–August, and over northern Australia in December–January–February. Aside from this slight warming, though, the G–3 Run has shown a significant improvement in the globally–averaged hydrology of the GISS model.

b. Zonally Averaged Water Balance. Figs. 3.13a–c show the zonally averaged values of precipitation, evaporation, and surface runoff over the landsurface for each of the simulations as well as observed values compiled by Zubenok (1970). Although Hansen et al. (1983) plotted zonally–averaged precipitation and evaporation and found very good agreement with observations, their comparison included the oceans. Since two–thirds of the earth is covered by oceans and the hydrologic fluxes over oceans are considerably larger than over land, the contribution of the landsurface alone was masked. Here we see that the zonally averaged hydrology over landsurfaces in the GISS Model II is actually in rather poor agreement with data (Run G–0). It should be noted that in zonally averaged plots, each latitude belt is given equal weight. In reality, however, the actual volume of the fluxes depends on the amount of landsurface in the latitude belt. Since most of the land mass over the earth is in the Northern Hemisphere (see Fig. 3.14), we must keep in mind that errors in zonal plots should be interpreted accordingly. In latitude bands where land comprises a small fraction of the total area, the estimates will have larger variance.

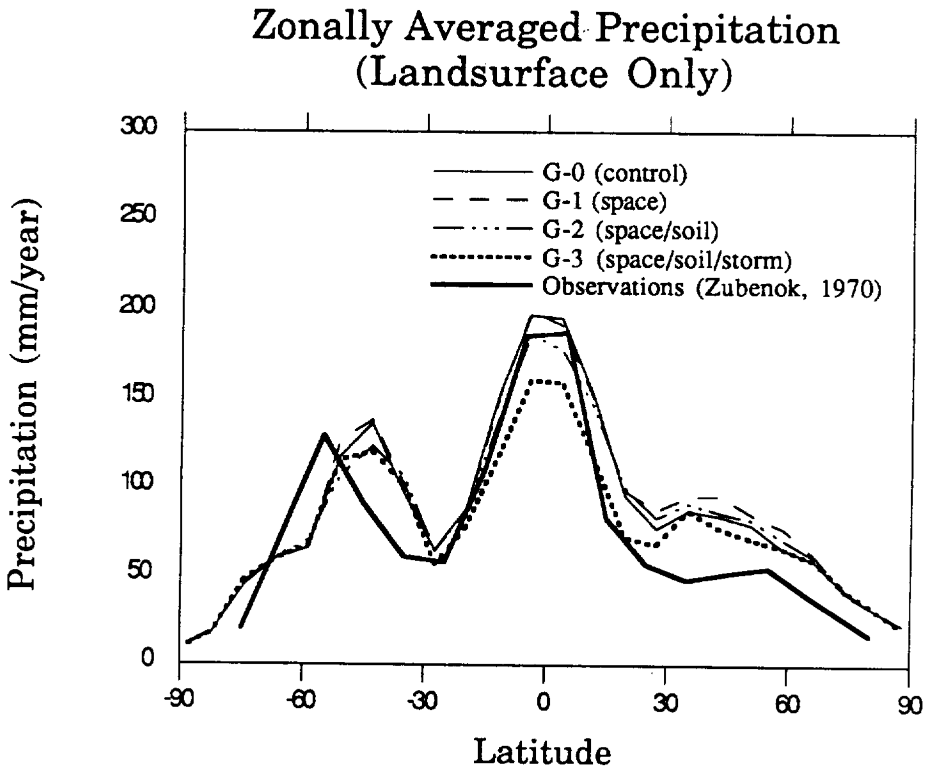

Figure 3.13a Zonally averaged annual landsurface precipitation

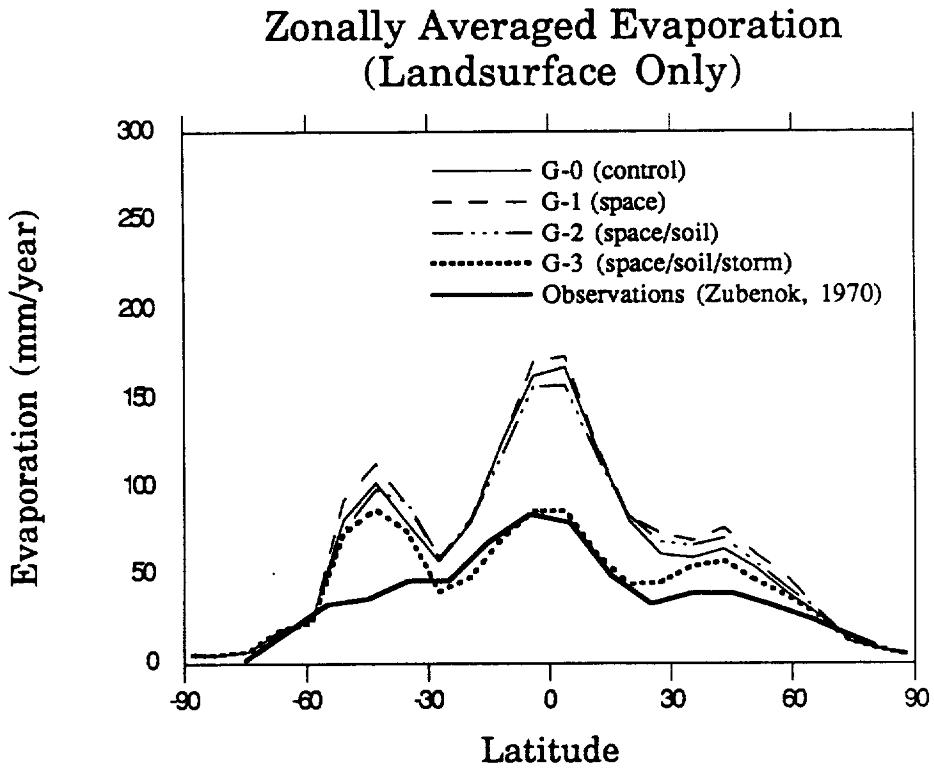

Figure 3.13b Zonally averaged annual landsurface evaporation

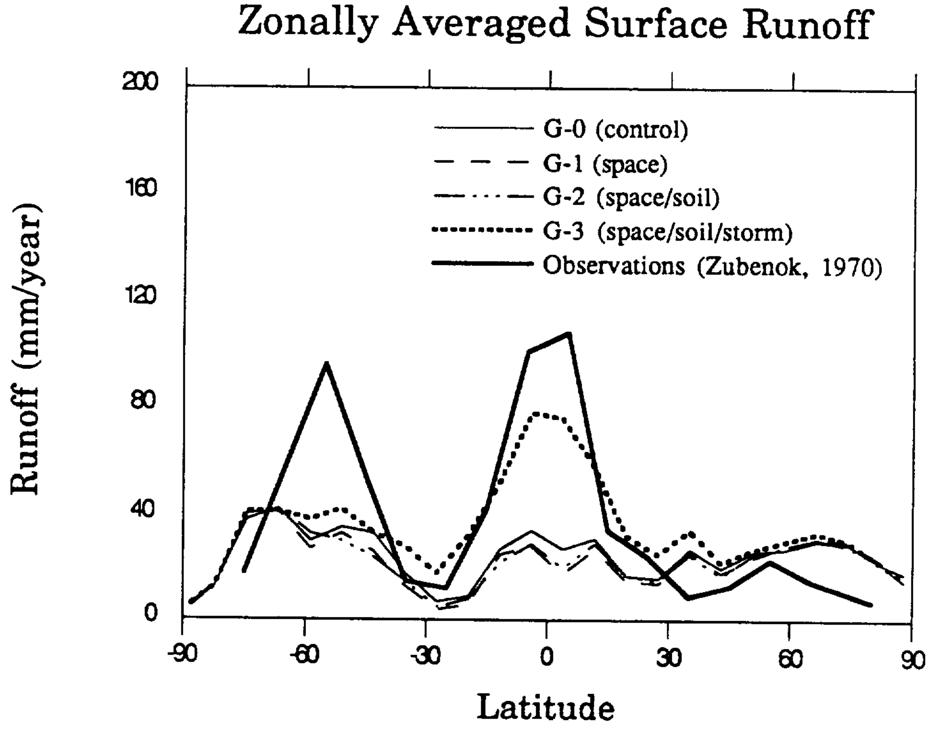

Figure 3.13c Zonally averaged annual surface runoff

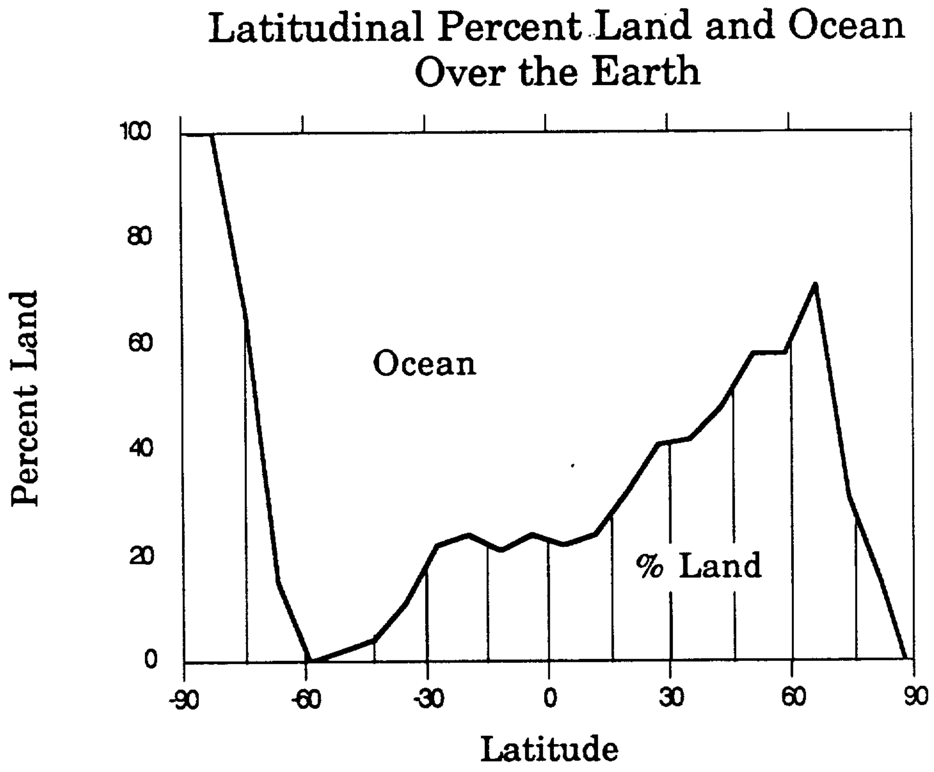

Figure 3.14 Percentage distribution of land and ocean as a function of latitude (taken from the GISS GCM)

As presented here, we see that in general, precipitation (Fig. 3.13a) is modeled quite well in the tropics, but agreement with observations deteriorates in the mid– and high latitudes. Particularly in the Northern Hemisphere mid–latitudes (where data are generally more readily available) precipitation is overestimated. The only strong deviation from the Control Run is Run G–3 in the tropics. Here we see that although Run G–3 had a very good globally averaged precipitation over land, it is actually underestimating in the tropics and overestimating in mid– and high latitudes.

In Fig. 3.13b the simulations G–1 and G–2 are essentially equivalent to the control in the zonal evaporation over land. Run G–3, however, gives agreement with observations in the tropics which is remarkable. In Fig. 3.13c the same pattern holds: runoff in Run G–3 comes much closer to the observed values in the tropics. The spike at 50° south latitude in the observed runoff is due to the fact that there is very little land in this belt (Fig. 3.14). Errors in data–sparse regimes such as this may be reflecting measurement error. Since evaporation observations are generally the residual of precipitation and runoff, an error in runoff measurement necessitates an error in evaporation "observations".

The balance at the tropics in Run G–3 makes it clear that the model is simply not producing enough precipitation in this region. Obviously if the evaporation is virtually in agreement with observation and both precipitation and runoff are low, there is a problem not in the landsurface parameterization, but in the atmospheric moisture transfer to the tropics and/or in the moist convection parameterization.

Conversely, in the Northern Hemisphere mid–latitudes, where all three of these variables are too *high*, there is an excess of precipitation. This again cannot be solved by the landsurface parameterization since runoff and evaporation are also exceeding observations.

We have seen that the effects of the reduced fractional wetting in moist convective rainfall in Run G–3 are strongest by far in the tropics. This warm, high humidity region has both the highest amount of rainfall and the highest percentage of moist–convective rainfall (see Fig. 3.2). Moving away from the tropics, the effects in Run G–3 are reduced nonlinearly, preserving similar values to the GISS Model II. As seen in these zonally averaged landsurface figures, the results are quite good for the GISS GCM equipped with the Entekhabi and Eagleson (1989a) new land surface hydrology parameterization with subgrid scale spatial variability and the new Abramopoulos et al. (1988) soil diffusion scheme. We wish to reemphasize in particular the dramatic improvement of the evaporation on all scales--global, zonal, and, as will be seen, in continental as well as over the river basins.

c. Continental Water Balance. As the next step in our progression to finer spatial detail, we consider the water balance over the continents. Shown in Table 3.3 and Figs. 3.15a–c are the precipitation, evaporation and surface runoff over continents (excluding Antarctica) for the four simulations as well as observations by Henning (1989). North America does not include Greenland, and Australia does not include New Zealand.

As we have seen before, Runs G–1 and G–2 differ only slightly from the control in most cases. Some modest exceptions include the substantial increase in both precipitation and evaporation over Europe in Run G–1 (which changed runoff very little), and a significant decrease in runoff over Africa in both G–1 and G–2. In Run G–3, there are major changes on all fronts. On all continents runoff was increased, while precipitation and evaporation were

Continental Hydrologic Balance (m/year)

Precipitation (mm/year)

Continent	G-0 (control)	G-1 (sp)	G-2 (sp/so)	G-3 (sp/so/st)	Observations (Henning, 1989)
South America	1396	1432	1361	1178	1481
Africa	1017	1003	911	831	695
Australia	768	734	756	597	471
Asia	1016	1064	1052	896	699
North America	778	851	796	734	622
Europe	767	911	865	717	597

Evaporation (mm/year)

Continent	G-0 (control)	G-1 (sp)	G-2 (sp/so)	G-3 (sp/so/st)	Observations (Henning, 1989)
South America	1172	1242	1172	682	883
Africa	877	902	828	478	502
Australia	662	672	674	400	403
Asia	708	776	737	519	417
North America	508	594	549	437	394
Europe	562	695	646	491	362

Surface Runoff (mm/year)

Continent	G-0 (control)	G-1 (sp)	G-2 (sp/so)	G-3 (sp/so/st)	Observations (Henning, 1989)
South America	216	180	185	516	598
Africa	139	100	89	373	193
Australia	105	65	82	208	67
Asia	309	291	309	409	282
North America	270	255	244	326	228
Europe	198	214	208	243	235

Table 3.3. Hydrologic balance of continents with observations by Henning (1989)

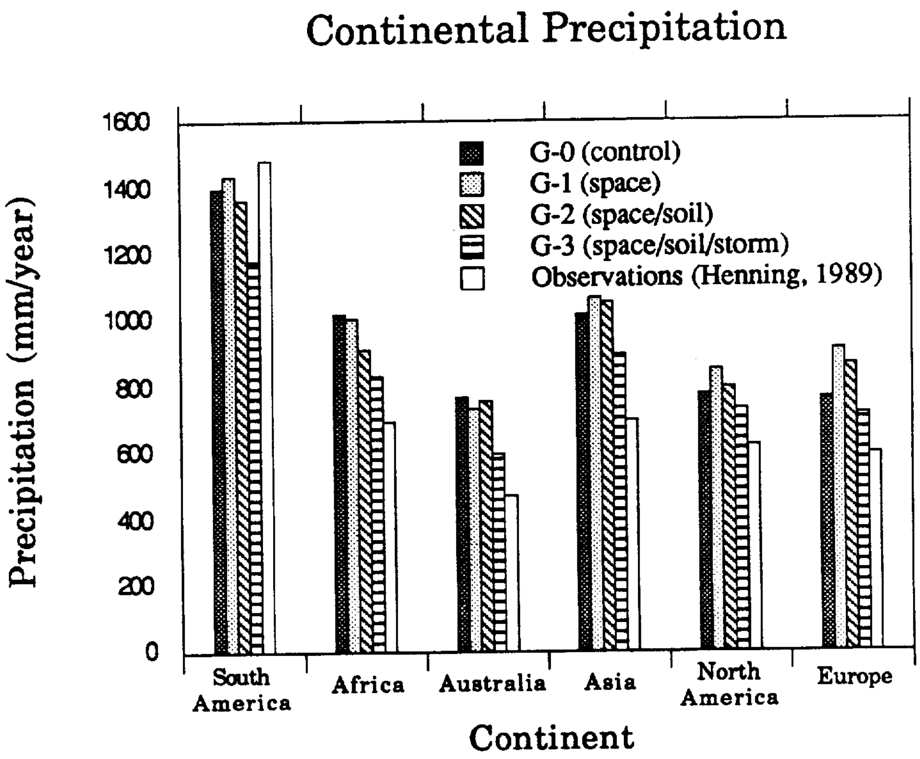

Figure 3.15a. Annual continental precipitation

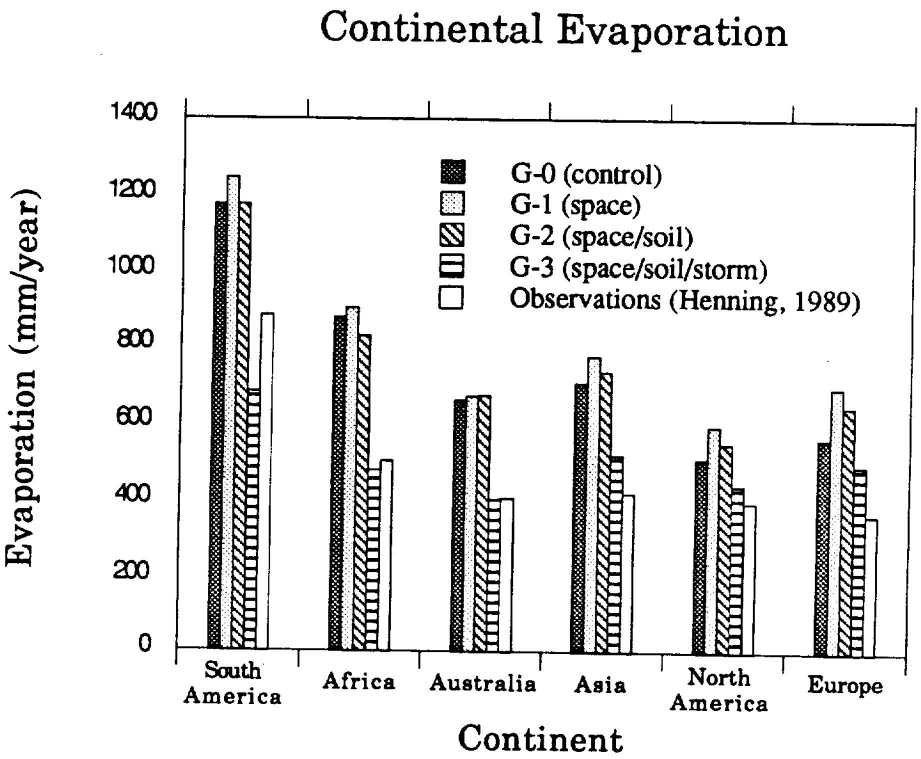

Figure 3.15b. Annual continental evaporation

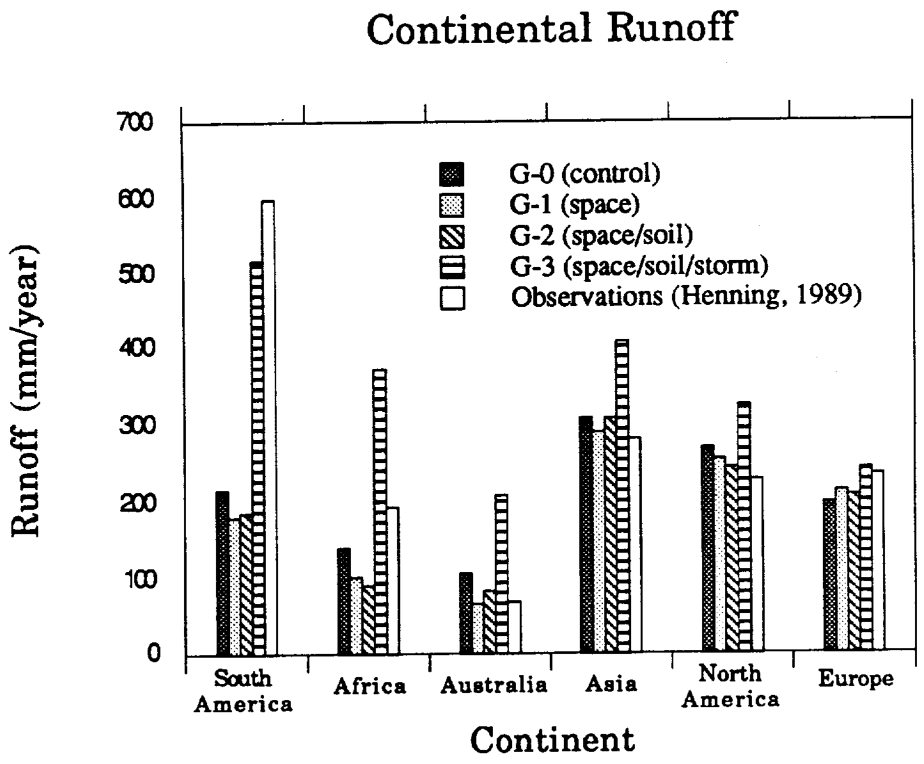

Figure 3.15c. Annual continental runoff

decreased. By comparison to observations, this was a significant improvement for all continents for evaporation, and an improvement in all but South America for precipitation. However, the runoff was only improved for two continents (South America and Africa) while the other four worsened in the direction of overestimation. It should be noted that the estimates of evaporation and runoff in Henning (1989) are independent of that made by Zubenok (1970). According to both sources, the Control Run G–0 with the GISS GCM severely overestimates landsurface evaporation and underestimates runoff. Hydrologic fluxes in Run G–3 with the improved parameterization are, however, in agreement with both sources.

The problem with runoff over continents is not solely a result of the landsurface parameterization but is partly due to there being an excess of precipitation. This can be seen by first noting that Run G–3 *evaporation* values over continents with high runoff values are all either very close to observed or else too high. But in all cases, the overestimation of *precipitation* is still higher, and thus, since runoff is also too high, we see that as before there is simply too much water being fed into the system by the atmospheric transport and rainfall generation. If the evaporative input to the atmosphere is roughly correct, then the problem of excessive precipitation lies in the atmospheric branch of the hydrologic cycle, which is not the subject of this work.

d. Major River Basin Water Balances. As a further step in evaluating the model hydrologic performance, the runoff over major river drainage systems will be compared to observations. We follow Russell and Miller (1990) in discretizing the GISS model into 33 river basins around the earth. In their paper, a 4° × 5° grid spacing was used in the model, as opposed to an

8° × 10° spacing used here. Further, their results were plotted by volume, whereas we will plot per unit area values in the water balance. The reason for this is that the modifications made act on a per unit area basis over grid squares and the pattern of the effects of the modifications is more readily apparent in this form. Furthermore ranking according to per unit area runoff helps in isolating the changes according to the levels of humidity in climate.

Tables 3.4a–c give the water balance components of the 33 basins in a diverse range of climatic zones arranged in descending order of per unit area observations. Figs. 3.16a–f show the runoff plotted in descending order of per unit area runoff; the first river basins shown are thus generally the most humid ones and the ones with the highest runoff ratios. It can be seen again that precipitation in the Northern Hemisphere is rather consistently overestimated in most of the basins.

In some cases, such as the Yellow River, the overestimation of precipitation is severe. The effects of this may be seen in the gross overestimation of runoff for this river (more than 15 times the observed value), in spite of evaporation being twice as large as observations. The observed value of runoff for this narrow basin is also prone to underestimation due to overbank flooding at times of high flow.

The striking improvement due to Run G–3 apparent in the tropical river basins depicted in Figure 3.16a–f confirms what was seen earlier in the zonally–averaged runoff plot for tropical regions. As the total runoff value decreases in more arid basins, we see the agreement becoming worse. However, one must keep in mind the overestimation of precipitation in these basins.

Major River Basin Precipitation (m/year)

River Basin	G-0 (control)	G-1 (sp)	G-2 (sp/so)	G-3 (sp/so/st)	Observations (Russell/Miller, 1990)
Irrawady	2.07	2.30	2.19	1.90	1.92
Amazon	**1.53**	**1.50**	**1.48**	**1.43**	**1.90**
Magdalena	2.17	2.12	2.14	1.81	1.55
Orinoco	**2.35**	**2.29**	**2.31**	**2.08**	**1.55**
Congo	**1.84**	**1.74**	**1.55**	**1.38**	**1.47**
Hsi Chiang	1.73	1.66	2.11	1.41	1.43
Mekong	2.27	2.43	2.41	2.01	1.38
San Francisco	2.29	2.38	2.07	1.66	1.36
Brahma-Ganges	**1.05**	**1.41**	**1.38**	**0.99**	**1.16**
LaPlata	0.62	0.64	0.65	0.60	1.15
Zambesi	1.30	1.18	1.15	1.12	1.01
Yangtze	**1.77**	**1.73**	**1.84**	**1.56**	**1.00**
Niger	1.08	1.16	1.00	0.70	1.00
St. Lawrence	1.05	1.09	0.96	0.89	0.88
Fraser	0.99	1.20	1.04	0.94	0.86
Mississippi	0.90	0.93	0.92	0.84	0.75
Danube	0.92	0.99	0.94	0.83	0.70
Nile	1.23	1.12	1.00	1.13	0.68
Columbia	0.88	1.13	0.94	0.86	0.63
Indus	0.82	0.78	0.66	0.65	0.55
Murray	0.92	0.88	0.93	0.82	0.54
Severnay Dvina	0.60	0.75	0.73	0.60	0.51
Amur	0.96	1.01	0.99	0.94	0.50
Yellow	2.10	1.97	2.04	2.07	0.48
Yukon	0.84	0.91	0.89	0.90	0.44
Ob	0.34	0.41	0.36	0.33	0.42
Orange	0.64	0.63	0.60	0.65	0.40
Tigris-Euphrates	0.49	0.61	0.59	0.53	0.39
McKenzie	0.68	0.74	0.71	0.67	0.39
Yenesei	0.53	0.57	0.54	0.47	0.37
Lena	0.57	0.65	0.62	0.58	0.33
Kolyma	0.72	0.74	0.74	0.72	0.26
Colorado	0.85	1.28	1.02	1.06	0.25

Table 3.4a Per unit area annual precipitation over major river basins; observations compiled by Miller and Russell (1990) (boldfaced lines indicate to five rivers by *volume*)

Major River Basin Evaporation (m/year)

River	G-0	G-1	G-2	G-3	Observations
Basin	(control)	(sp)	(sp/so)	(sp/so/st)	(Russell/Miller, 1990)
San Francisco	1.76	1.82	1.65	0.97	1.21
Congo	**1.54**	**1.58**	**1.43**	**0.77**	**1.14**
LaPlata	0.57	0.61	0.60	0.38	0.99
Irrawady	1.62	1.84	1.74	1.19	0.93
Amazon	**1.33**	**1.33**	**1.28**	**0.76**	**0.88**
Niger	0.98	1.08	0.92	0.36	0.85
Zambesi	1.12	1.09	1.05	0.66	0.83
Mekong	1.68	1.88	1.82	1.21	0.78
Hsi Chiang	1.28	1.34	1.49	0.88	0.74
Nile	1.05	1.00	0.91	0.61	0.65
Mississippi	0.67	0.74	0.74	0.60	0.57
Magdalena	1.79	1.89	1.81	0.95	0.56
Yangtze	**1.11**	**1.20**	**1.15**	**0.86**	**0.54**
Murray	0.77	0.80	0.83	0.58	0.52
Brahma-Ganges	**0.86**	**1.15**	**1.10**	**0.70**	**0.50**
St. Lawrence	0.62	0.75	0.64	0.55	0.45
Orinoco	**1.91**	**1.99**	**1.94**	**1.08**	**0.44**
Danube	0.71	0.82	0.77	0.62	0.44
Yellow	0.89	0.86	0.83	0.81	0.42
Orange	0.57	0.57	0.56	0.46	0.39
Tigris-Euphrates	0.44	0.56	0.56	0.41	0.35
Fraser	0.64	0.85	0.73	0.66	0.35
Amur	0.64	0.69	0.65	0.58	0.32
Indus	0.57	0.61	0.54	0.42	0.30
Ob	0.24	0.32	0.26	0.22	0.27
Columbia	0.67	0.88	0.76	0.67	0.26
Colorado	0.65	1.02	0.86	0.77	0.22
McKenzie	0.39	0.45	0.44	0.39	0.22
Severnay Dvina	0.31	0.41	0.38	0.30	0.21
Yukon	0.36	0.43	0.40	0.37	0.20
Kolyma	0.28	0.29	0.31	0.26	0.15
Yenesei	0.38	0.44	0.39	0.33	0.15
Lena	0.39	0.43	0.42	0.37	0.13

Table 3.4b Per unit area annual evaporation over major river basins; observations compiled by Miller and Russell (1990) (boldfaced lines indicate top five rivers by *volume*)

Major River Basin Runoff (m/year)

River Basin	G-0 (control)	G-1 (sp)	G-2 (sp/so)	G-3 (sp/so/st)	Observations (Russell/Miller, 1990)
Orinoco	**0.43**	**0.29**	**0.34**	**1.03**	**1.11**
Amazon	**0.20**	**0.17**	**0.20**	**0.70**	**1.02**
Irrawady	0.41	0.45	0.43	0.83	1.00
Magdalena	0.36	0.24	0.30	0.89	0.99
Hsi Chiang	0.44	0.33	0.58	0.64	0.69
Brahma-Ganges	**0.20**	**0.27**	**0.25**	**0.31**	**0.66**
Mekong	0.55	0.54	0.57	0.92	0.59
Fraser	0.35	0.36	0.32	0.30	0.51
Yangtze	**0.63**	**0.54**	**0.68**	**0.78**	**0.46**
St. Lawrence	0.43	0.35	0.31	0.37	0.43
Columbia	0.20	0.25	0.21	0.24	0.37
Congo	**0.29**	**0.16**	**0.13**	**0.65**	**0.33**
Severnay Dvina	0.28	0.33	0.34	0.32	0.30
Indus	0.25	0.17	0.10	0.25	0.25
Danube	0.20	0.18	0.17	0.24	0.25
Yukon	0.47	0.48	0.48	0.52	0.23
Yenesei	0.14	0.14	0.14	0.17	0.22
Lena	0.18	0.21	0.20	0.24	0.21
Zambesi	0.19	0.09	0.12	0.49	0.19
Amur	0.34	0.33	0.32	0.38	0.18
Mississippi	0.22	0.19	0.18	0.27	0.18
LaPlata	0.05	0.04	0.05	0.23	0.17
McKenzie	0.29	0.28	0.27	0.29	0.17
Niger	0.10	0.09	0.08	0.35	0.16
San Francisco	0.53	0.55	0.43	0.75	0.15
Ob	0.10	0.10	0.11	0.12	0.15
Kolyma	0.41	0.45	0.43	0.46	0.11
Yellow	1.21	1.11	1.20	1.26	0.07
Tigris-Euphrates	0.06	0.05	0.03	0.12	0.04
Colorado	0.19	0.27	0.14	0.28	0.03
Nile	0.17	0.12	0.10	0.54	0.03
Murray	0.15	0.08	0.11	0.25	0.02
Orange	0.07	0.05	0.04	0.20	0.01

Table 3.4c. Per unit area annual runoff over major river basins; observations compiled by Miller and Russell (1990) (boldfaced lines indicate top five rivers by *volume*)

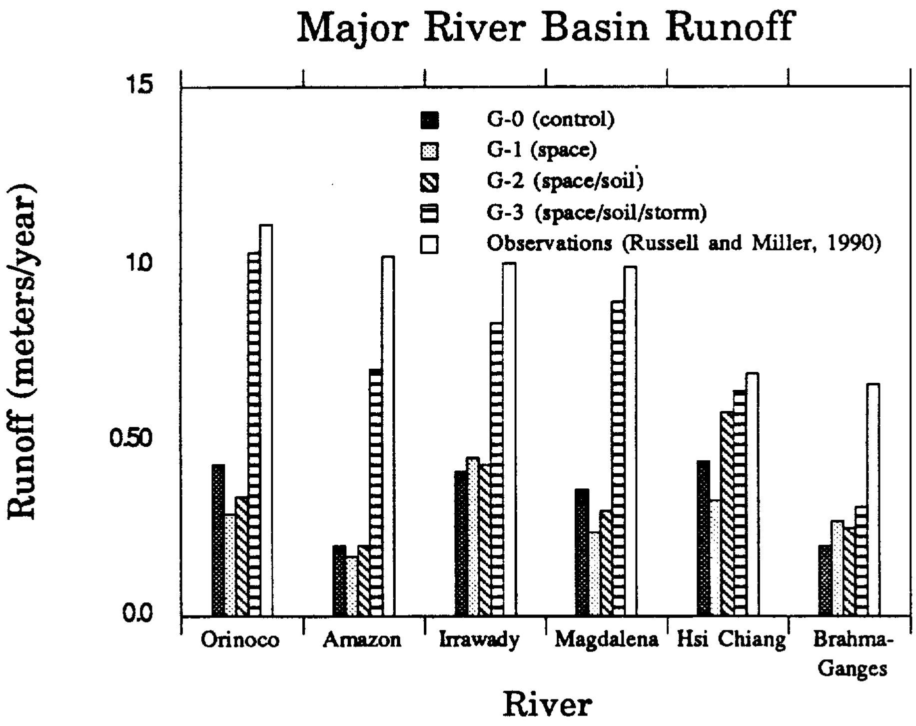

Figure 3.16a Per unit area annual runoff over major river basins

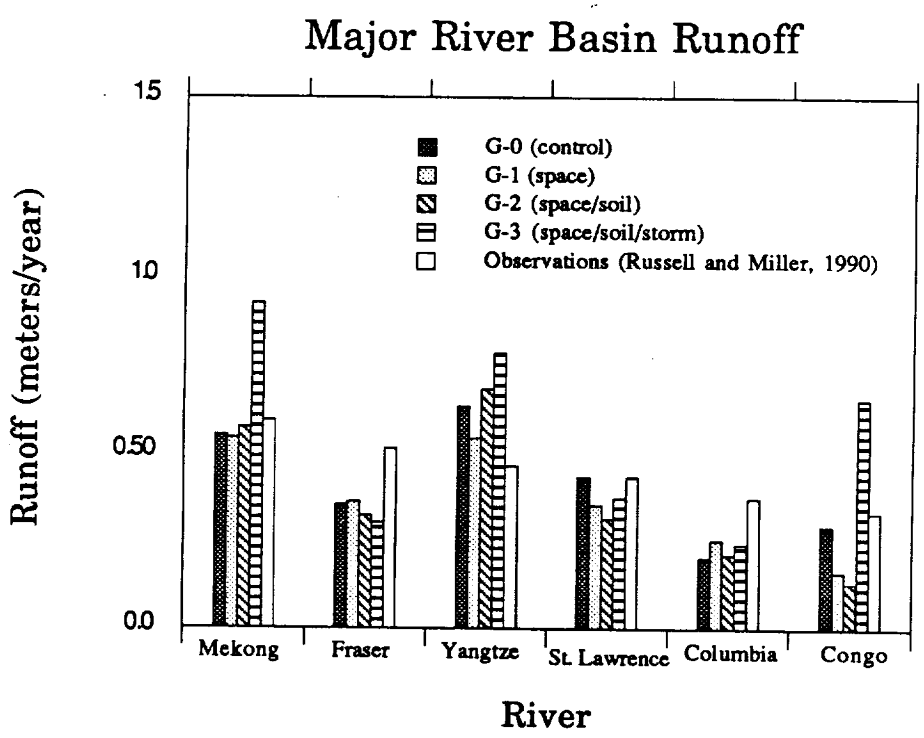

Figure 3.16b Per unit area annual runoff over major river basins

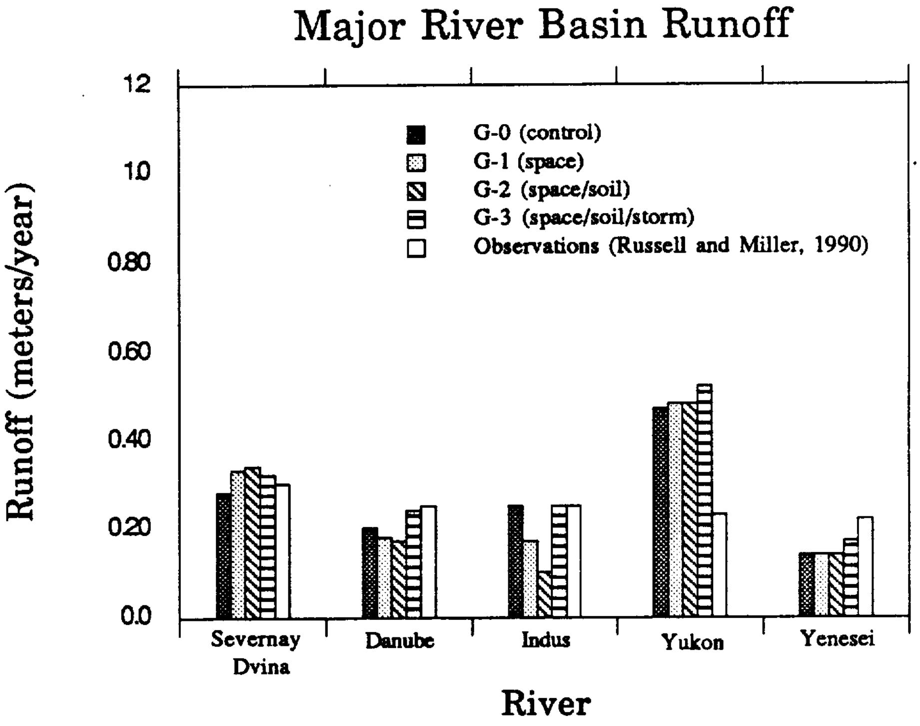

Figure 3.16c Per unit area annual runoff over major river basins

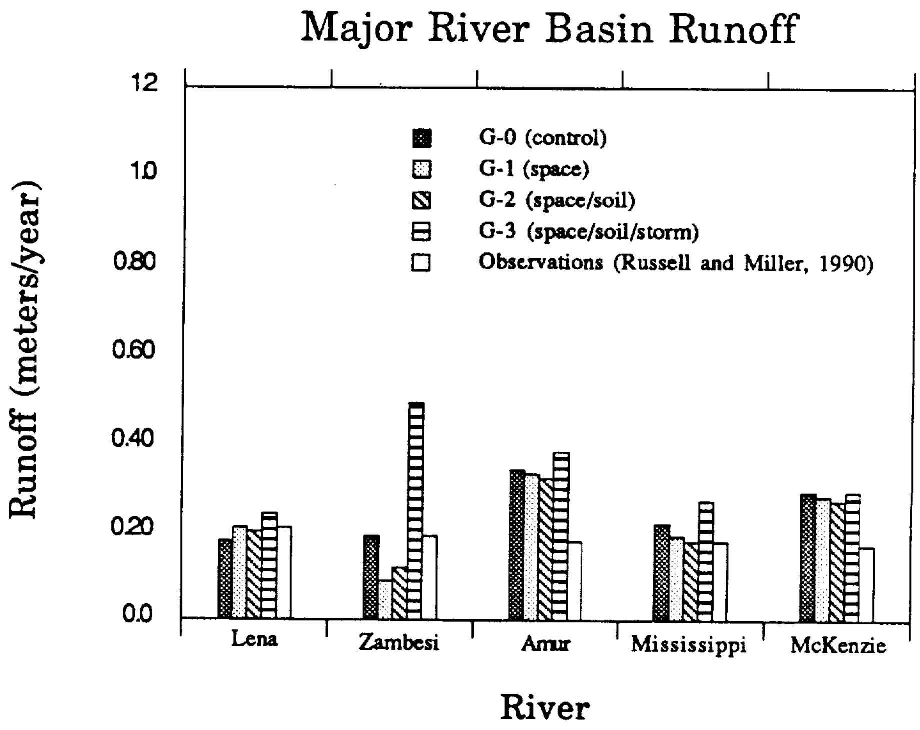

Figure 3.16d Per unit area annual runoff over major river basins

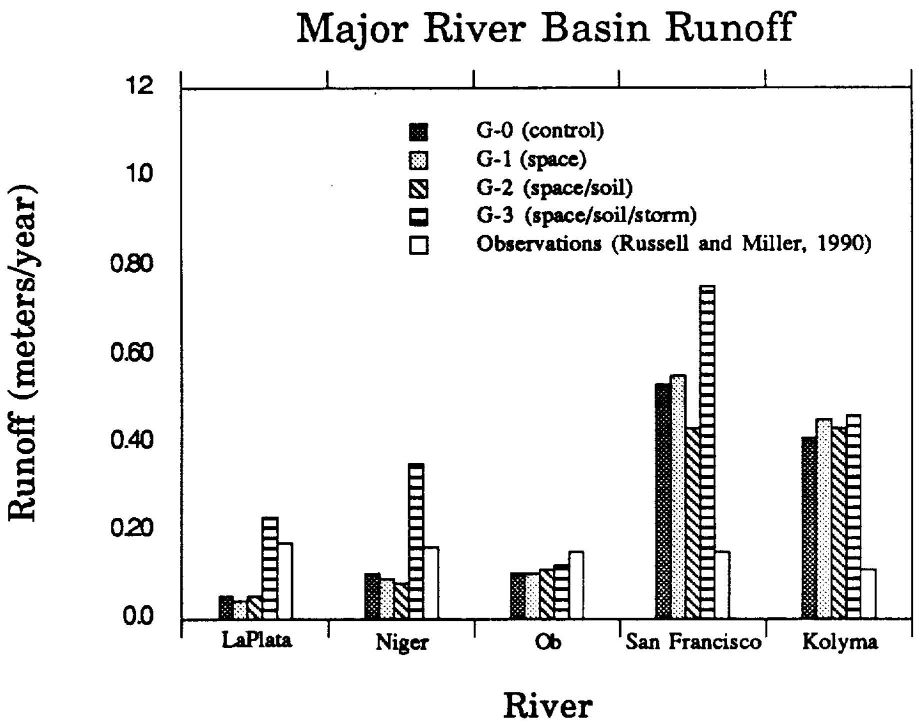
Major River Basin Runoff

Figure 3.16e Per unit area annual runoff over major river basins

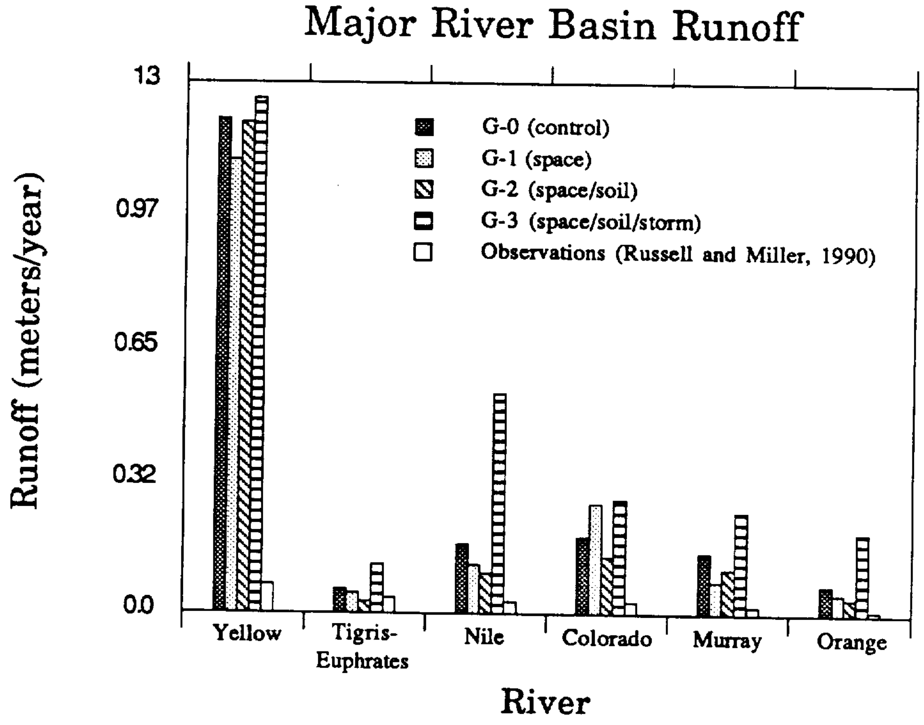

Figure 3.16f Per unit area annual runoff over major river basins

3. Temperature and the Heat Balance

The hydrologic balance over landsurfaces has a strong effect on the regional heat balance. The mechanisms include: 1) atmospheric transport of latent heat, 2) the radiative absorption and emittance by atmospheric water vapor, 3) the reflective properties of clouds, 4) the reflective properties of snow on the earth's surface, 5) the increase of soil heat capacity due to the presence of soil moisture and 6) the release of latent heat from the surface by evaporation. There are also secondary effects such as those due to the dependence of vegetation type and productivity on the moisture budget and the influence of the heat budget on wind patterns. Of all these mechanisms, it is the evaporation which has the strongest effect on the surface temperature; it is a major cooling mechanism of the landsurface when moisture is available. As moisture in the soil is depleted, the heat partitioning at the surface shifts toward higher rates of sensible heat flux. Since the sensible heat flux is a much less efficient transfer process, temperatures at the surface may rise significantly under reductions in soil moisture.

In Appendix A, Figs. A.5a–d show the global distribution of surface air temperature of the Control Run G–0 for December–January–February (DJF) and June–July–August (JJA), as well as deviations from the Control for each simulation G–1 to G–3. While there are isolated changes (mainly summer cooling) in Runs G–1 and G–2, the most dramatic effects are in Run G–3 since the hydrology changed significantly in this simulation. By comparison to the evaporation Figs. (A.2a–d) and surface soil moisture Figs. (A.4a–d) it can be seen that generally lower temperatures are produced in areas of increased soil moisture and increased evaporation. The converse is also true. Our main concern is with Run G–3 since it showed the greatest improvement hydrologically. We now consider surface air temperature comparisons with data in zonal mean and global distribution. This parameter captures the effects of the new schemes on the heat balance in the GCM most effectively.

In the zonal mean, the effects of the modified hydrology become more apparent. Figs. 3.17a–c show zonal mean surface air temperatures over the landsurface for all simulations along with observations compiled by Legates and Willmott (1990). Fig. 3.17a is the annual mean while Figs. 3.17b and 3.17c are the winter and summer means, respectively. As can be seen, all simulations are essentially the same except in the tropics. Here Run G–3 diverges from the other three, ranging from 0 to 2 degrees warmer. In the annual mean, we see that Run G–3 is actually in exceptionally good agreement with data from 20 S. Latitude to 20 N. Latitude. The seasonal means also show Run G–3 to be an improvement except for a small latitude belt near the equator in the summertime. In the global distribution, we shall see this is mainly caused by excessive heating in the Amazon and Caribbean regions.

Fig. 3.18 gives observed January and July global surface air temperature distributions. Figs. 3.19a and b show the Control Run G–0 and Run G–3 DJF and JJA surface air temperature distributions. Due to reduced runoff, and therefore reduced soil moisture and evaporation, Run G–3 is in general slightly warmer than the Control Run. For the winter months, agreement is quite good. For the summer, Run G–3 has the Caribbean and northern South America to be approximately 2–4 degrees too warm. Also, the region over Saudi Arabia has gotten slightly warmer (1 degree), but as it was already on the order of 3–5 degrees too warm in the Control Run, this is not severe. The region over west Africa has improved, becoming warmer and closer to observations. The top of Fig. 3.19b shows that the Control Run G–0 has this region almost 5° too cool during the summer.

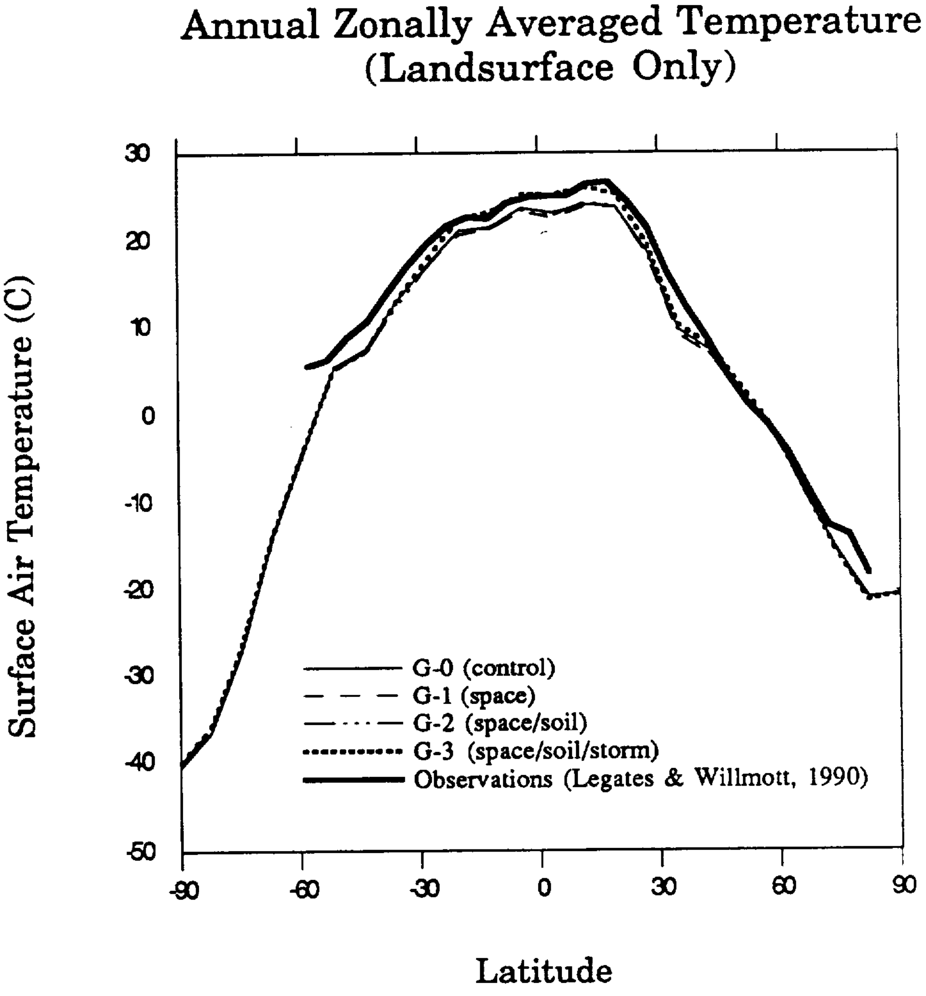

Figure 3.17a Annual zonally averaged surface air temperature over landsurface areas; observations are from Legates and Willmott (1990)

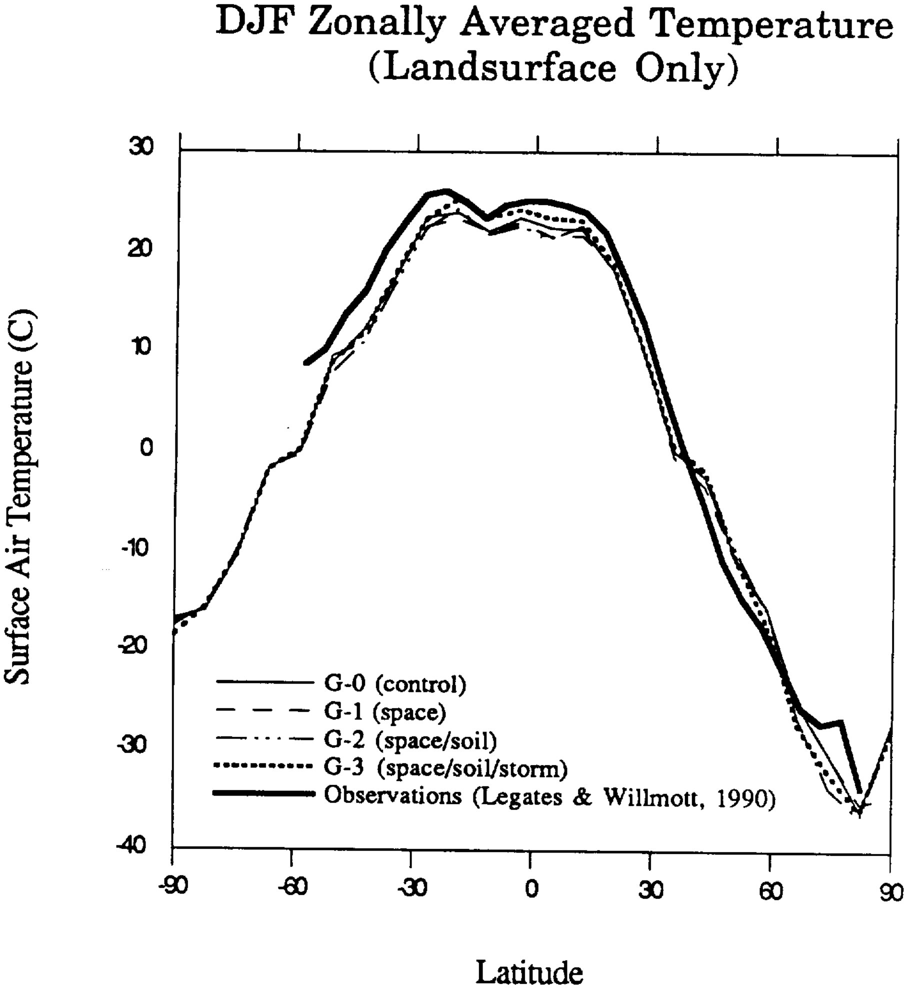

Figure 3.17b Zonally averaged surface air temperature over landsurface areas over landsurface areas for December–January–February; observations are from Legates and Willmott (1990)

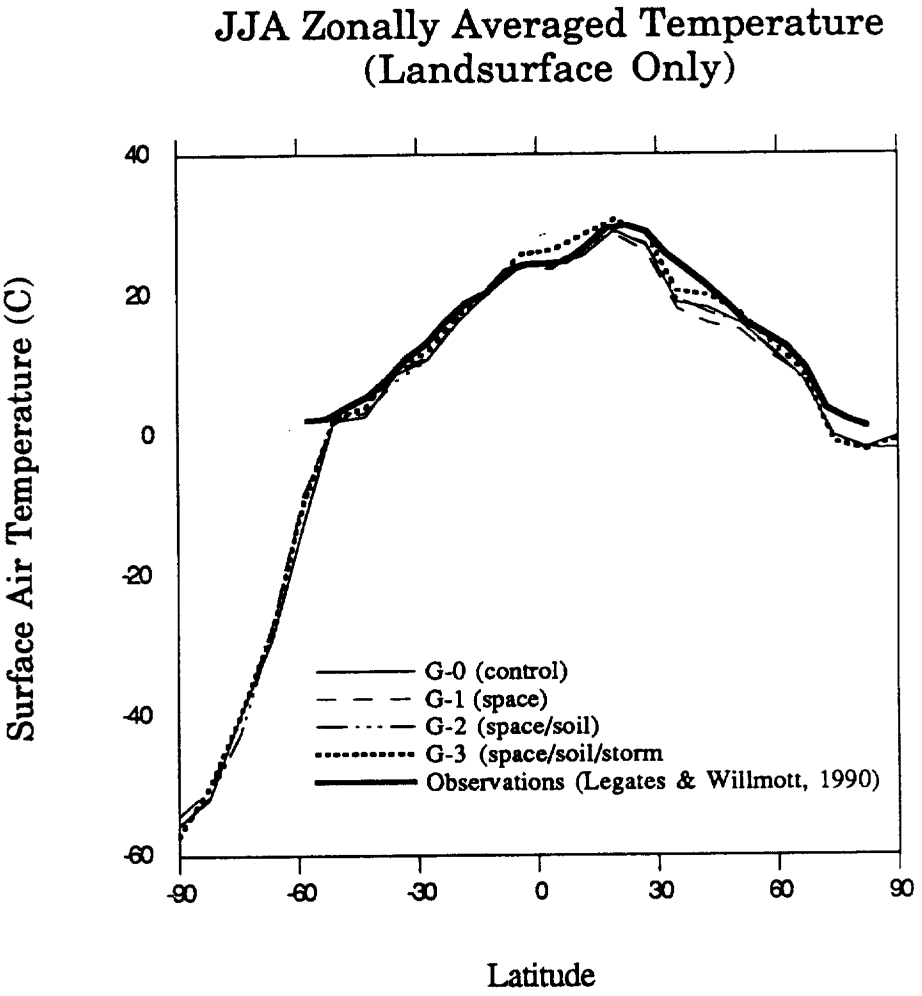

Figure 3.17c Zonally averaged surface air temperature over landsurface areas over landsurface areas for June–July–August; observations are from Legates and Willmott (1990)

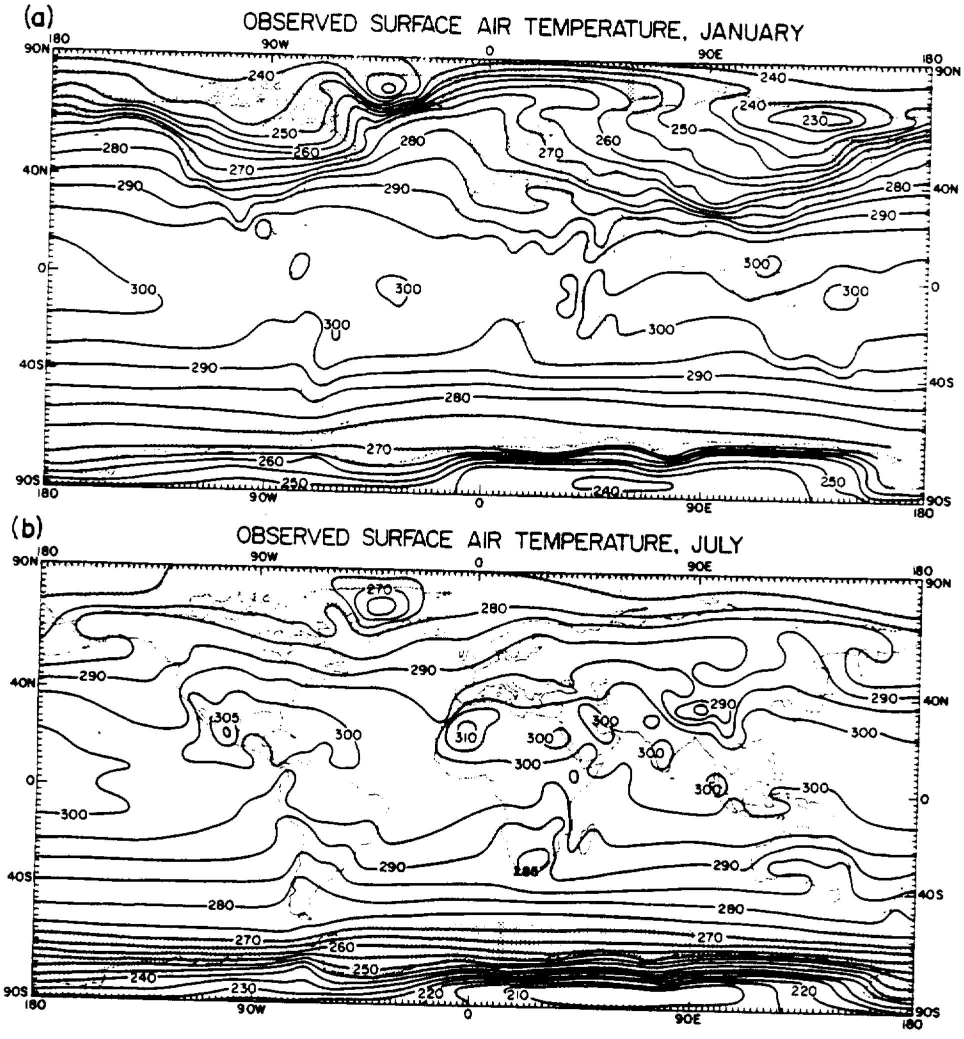

Figure 3.18 (a) January and (b) July long–term mean geographical distributions of surface air temperature. [From Washington and Meehl (1984)]

CONTROL (G-0) JAN SURFACE AIR TEMPERATURE (K)

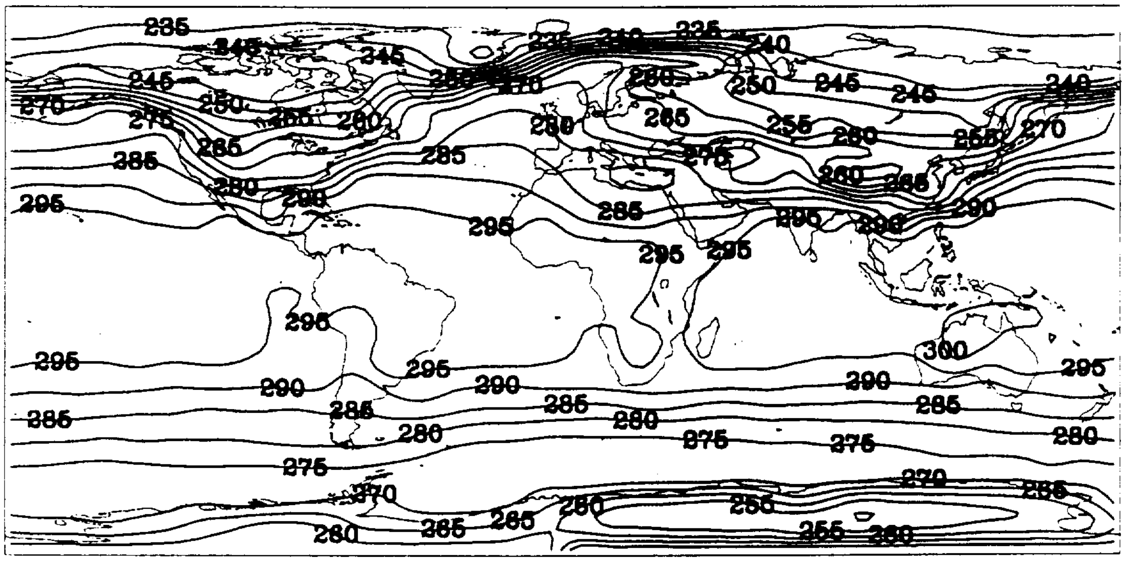

G-3 (SP/SO/ST) JAN SURFACE AIR TEMPERATURE (K)

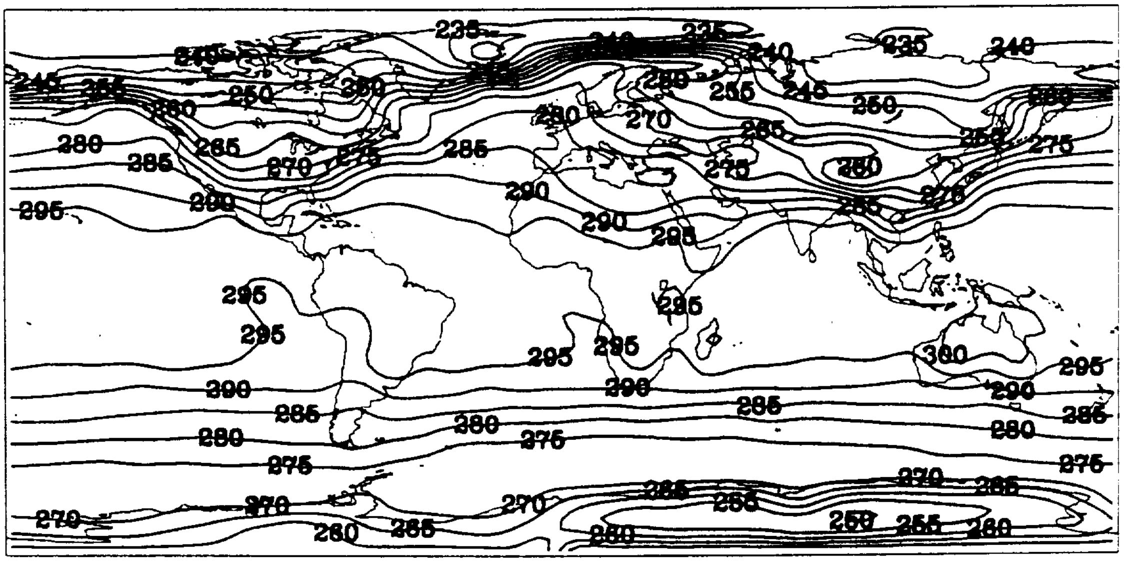

Figure 3.19a Winter surface air temperatures for Control Run G–0 and Run G–3 (space/soil/storm)

CONTROL (G–0) JUL SURFACE AIR TEMPERATURE (K)

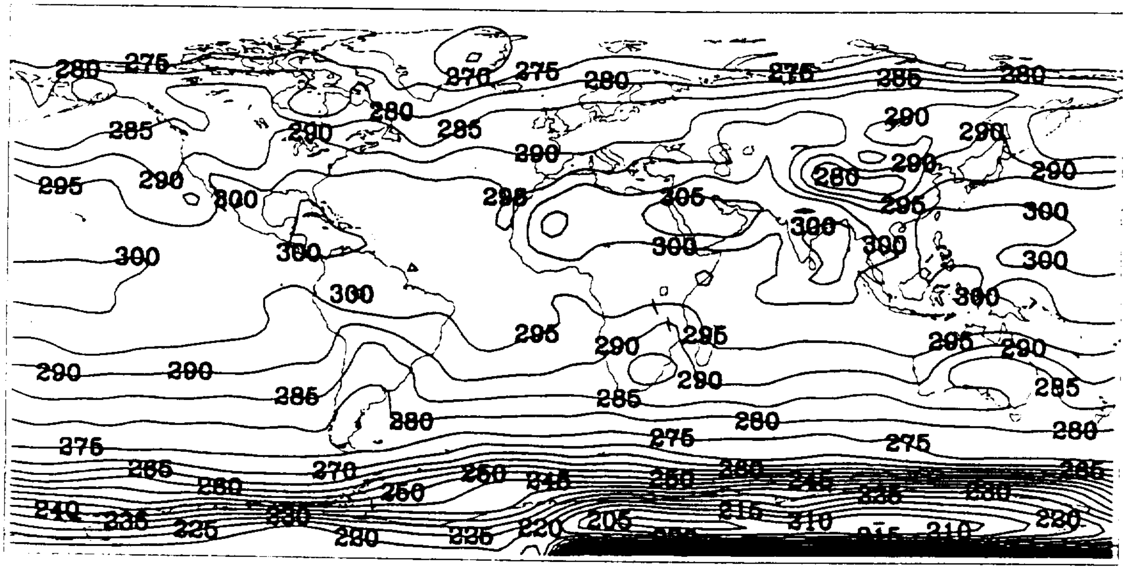

G–3 (SP/SO/ST) JUL SURFACE AIR TEMPERATURE (K)

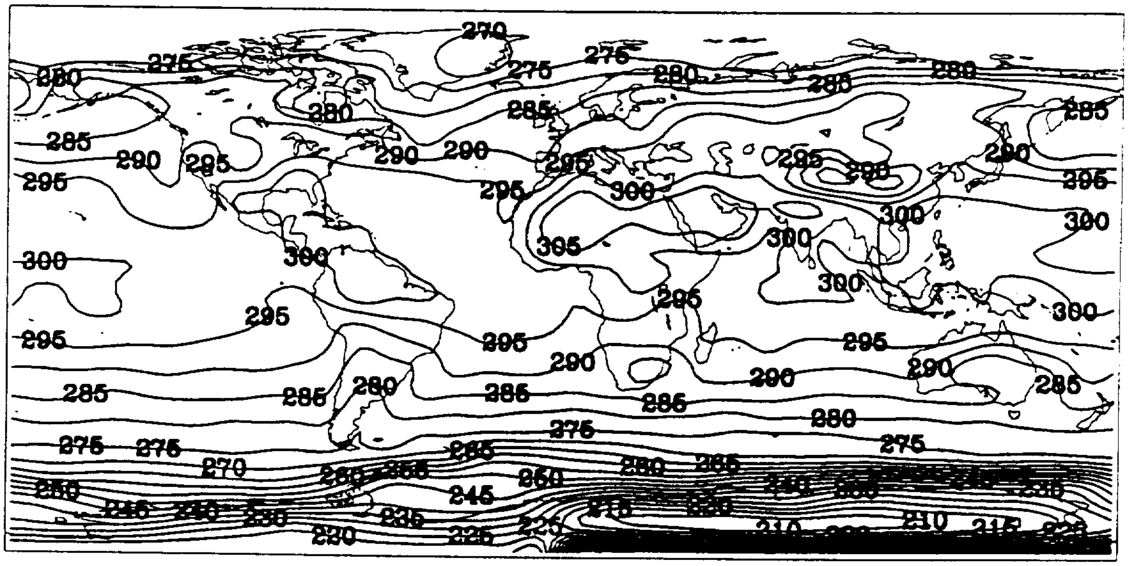

Figure 3.19b Summer surface air temperatures for Control Run G–0 and Run G–3 (space/soil/storm)

All in all, landsurface temperatures in the GISS GCM are in good agreement with observations. We have seen that the modified hydrology of the model in Run G-3 has in some areas improved surface air temperatures and in some areas made it worse. In the annual zonal mean, however, the agreement with data which is already quite good in the current GISS Model II has been improved still further with the inclusion of spatial variability.

4. Precipitation in the GISS GCM

It has been a recurring theme throughout this section that errors in runoff and evaporation can in large part be traced to errors in the precipitation generated by the model. Although it is not the point of this research to suggest methods of improvement on the precipitation mechanism, it is nevertheless instructive to show in more detail the deviation of the model precipitation from observed data.

We have already seen that model precipitation is severely in error over many river basins. As shown in Table 3.4a, the model predicts roughly 2 meters/year rainfall over the Yellow River, yet the observed value is only 0.68 meters/year. The generally more dry climates of the Yellow, Nile, Kolyma, Yukon, Colorado, and Amur river basins are all overpredicted by at least 100%. Further, more than half of the 33 selected basins show model precipitation to be in error by 50% or more on an annual basis. A more complete picture of precipitation can be seen by observing the seasonal distributions.

Figs. 3.20 and 3.21a–b show winter/summer precipitation observations (Schutz and Gates, 1971) and those simulated by GCM. The regional high rainfall accounts for the overestimated river basin precipitation. Most notable is the extreme maxima over Southeast Asia. Generally the

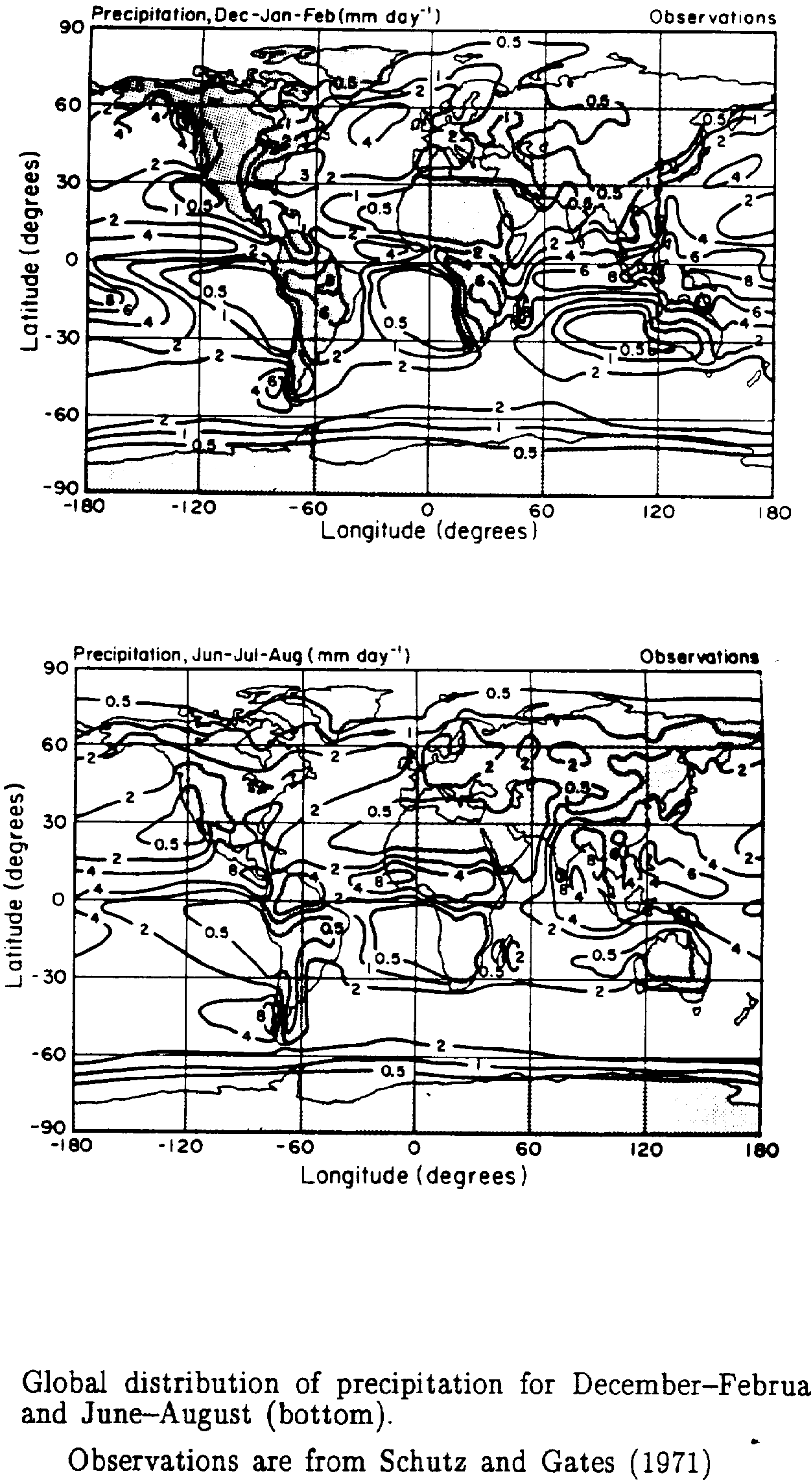

Figure 3.20 Global distribution of precipitation for December–February (top) and June–August (bottom).

Observations are from Schutz and Gates (1971)

CONTROL (G-0) DJF PRECIPITATION (MM/DAY)

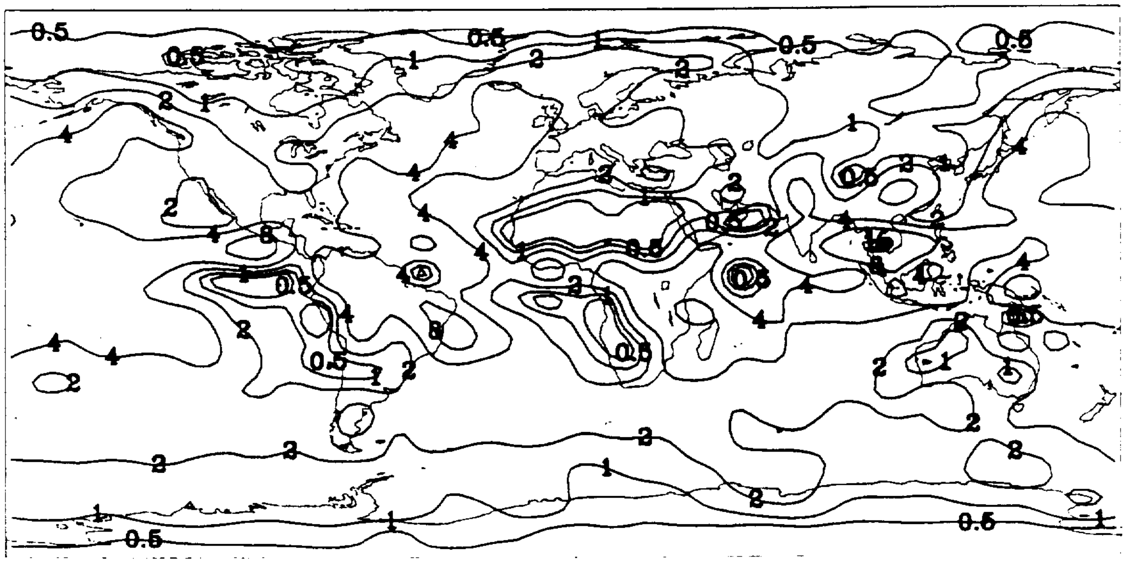

G-3 (SP/SO/ST) DJF PRECIPITATION (MM/DAY)

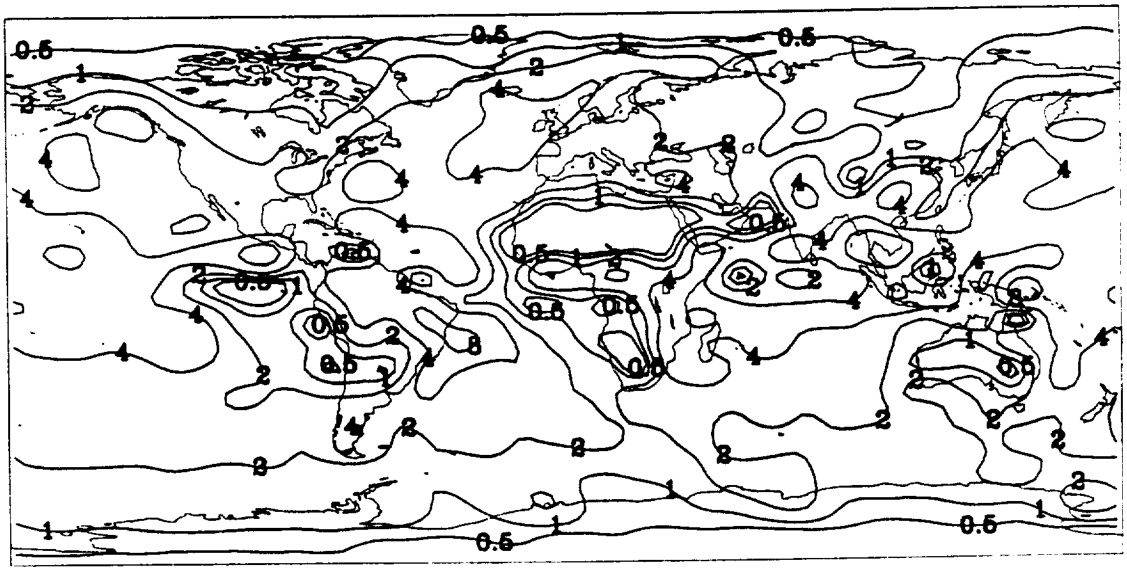

Figure 3.21a Winter precipitation for Control Run G–0 and Run G–3 (space/soil/storm)

CONTROL (G-0) JJA PRECIPITATION (MM/DAY)

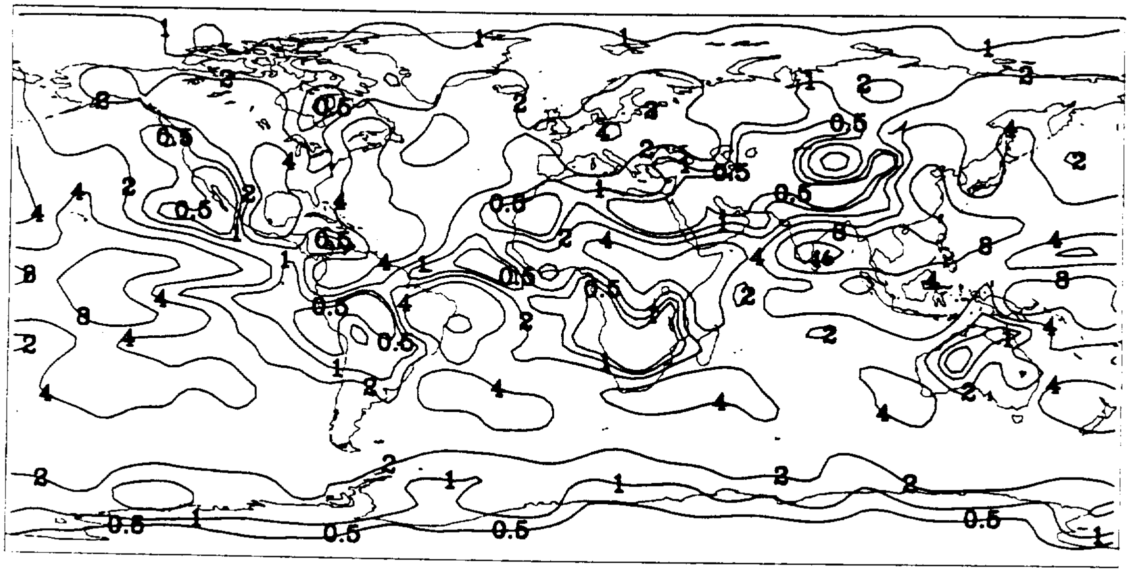

G-3 (SP/SO/ST) JJA PRECIPITATION (MM/DAY)

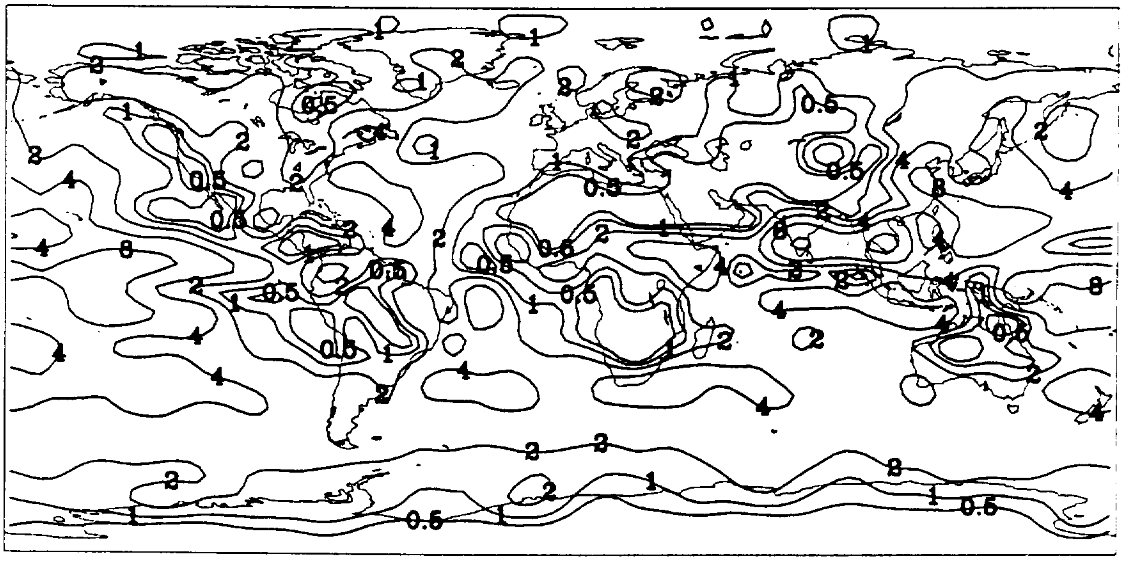

Figure 3.21b Summer precipitation for Control Run G-0 and Run G-3 (space/soil/storm)

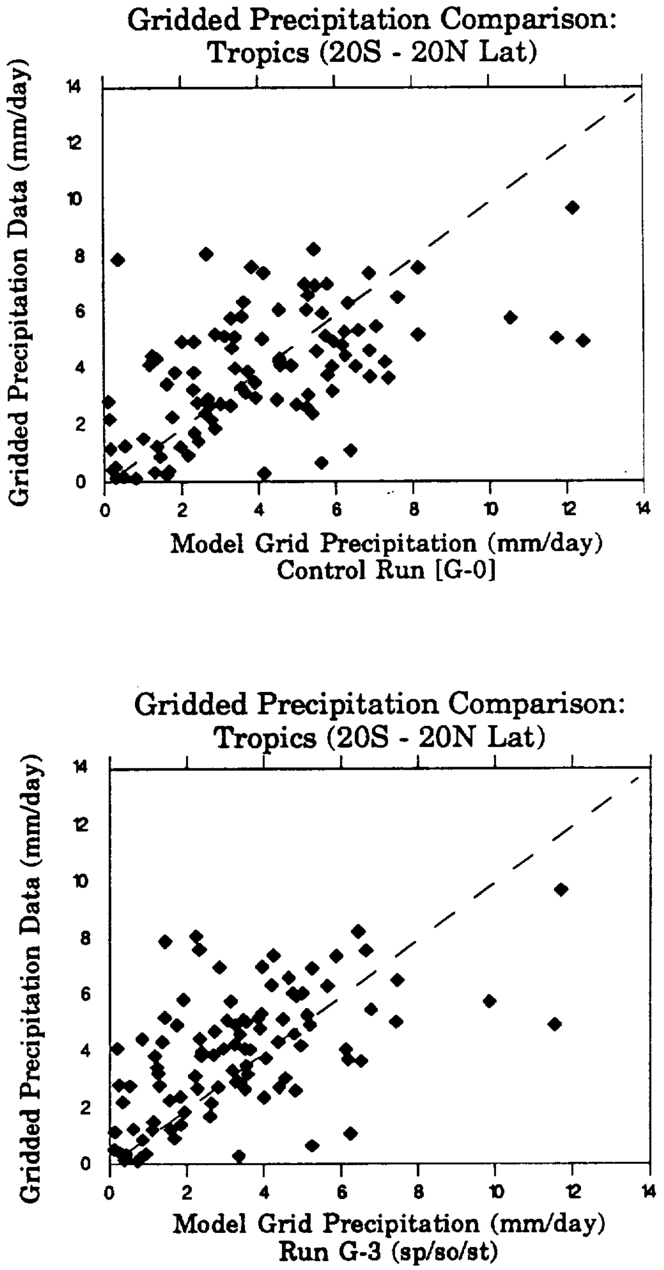

Figure 3.22 Gridded precipitation comparison with observations (NCAR, 1988) over tropics for Control Run G–0 and Run G–3 (space/soil/storm)

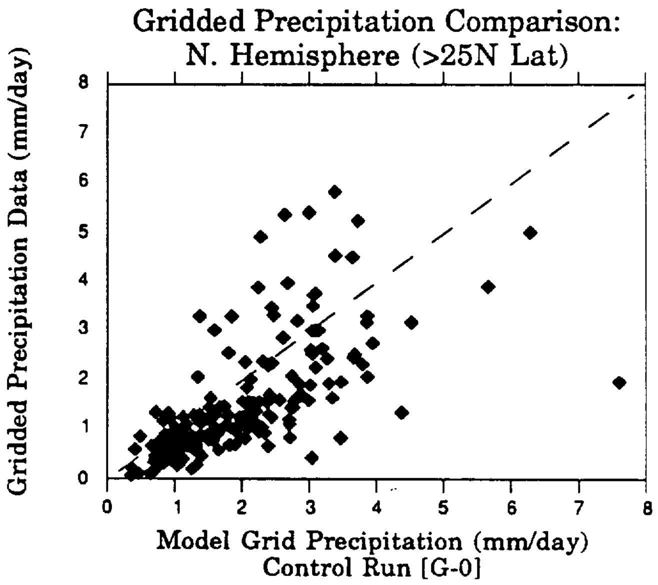

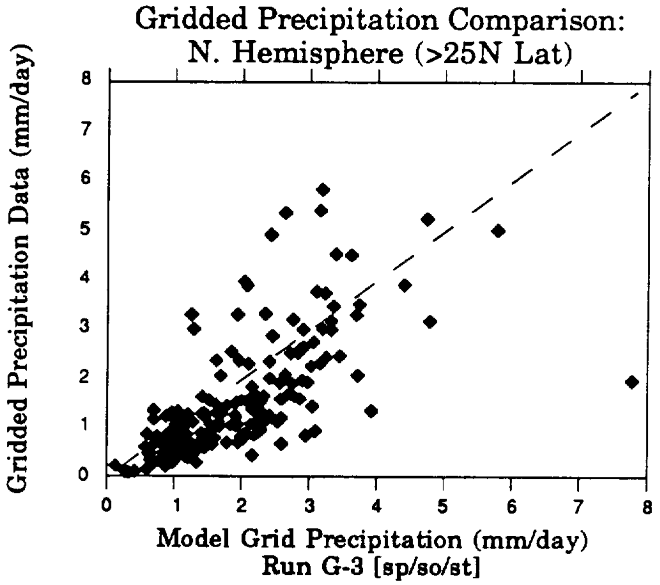

Figure 3.23 Gridded precipitation comparison with observations (NCAR, 1988) over Northern Hemisphere for Control Run G–0 and Run G–3 (space/soil/storm)

spatial extent and intensity of the monsoon circulations in the GISS model are stronger than that which actually exists. The grid resolution and ocean model may be responsible. (Note: Miller and Russell (1990) show that the 4 × 5 degree resolution version of the GISS GCM has considerably better precipitation climatology).

A precipitation data set from the National Center for Atmospheric Research (NCAR) compiled by Spangler and Jenne (1988) was used to compare precipitation on a grid square basis. The data set covers the years 1963 through 1973 and uses more than 3900 different stations over the Globe. The data were gridded to match GISS 8° × 10° grid squares by a simple "nearest–neighbor" averaging technique (Theissen polygons). Fig. 3.22 shows the Control Run and Run G–3 for tropical landsurface grids (20 S to 20 N) and Fig. 3.23 shows the same for the Northern Hemisphere (>20 N). This latitude splitting shows results similar to the zonally averaged precipitation in Fig. 3.13a in the tropics; that is, the mean of the Control Run G–0 is roughly equivalent to the mean of observation. On the other hand, the mean of Run G–3, upon close inspection, can be seen to be slightly lower than the observations. In the Northern Hemisphere, both simulations are slightly higher in their means than observations. Thus two independent data sets reveal the same diagnosis of rainfall in a rough breakdown of zonal mean values. Further, the plots show the severe error of precipitation generation over most grids – generally ±50% or greater from observations.

Finally, we also consider the frequency of rainfall over three selected grid squares. Fig. 3.24 shows a map of three U.S. grid squares for which *hourly* precipitation values were recorded during each of the simulations. We define these grids as "North Central", "Southeast", and "Southwest" even though they cover only part of the areas generally associated with these terms.

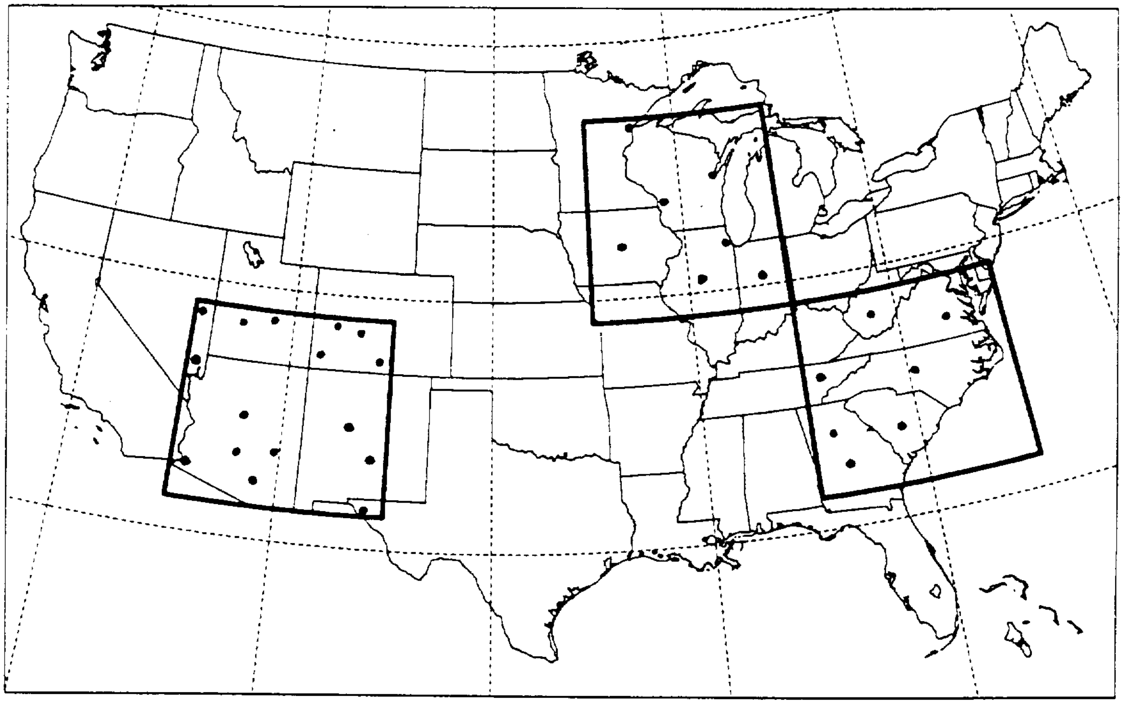

Figure 3.24 Locations of "North Central U.S.", "Southeast U.S.", and "Southwest U.S." grids along with representative stations

A data set of hourly precipitation records (spanning 40 years) for major U.S. cities (Earthinfo, 1989) was used to compare rainfall frequency. The probability of rain in the model is estimated from the frequency of hours for which there is either supersaturation or moist–convective rainfall. Similar statistics are computed for the observed precipitation for three regions corresponding to GISS GCM grids over North America.

Figs. 3.25a–c show the comparison of the selected GISS GCM grid fraction of time with precipitation and the values observed for several measurement stations within the grid region. The differences between these statistics for Runs G–0, G–1, G–2 and G–3 are not tested for statistical significance since the simulations are only for a few years each. Over the three regions, the GISS GCM generally gives between 15 and 20 percent of the hours as hours with precipitation. The observations, based on the average of seven stations over the "Southeast U.S." region, generally give about 7 percent probability of rain in any hour. A value of closer to 6 percent is found for the "North Central U.S." region as depicted in Fig. 3.25b. Over the "Southwest U.S." region where much of the rainfall is due to moist–convective processes, there is a larger range in observed statistic for the five stations

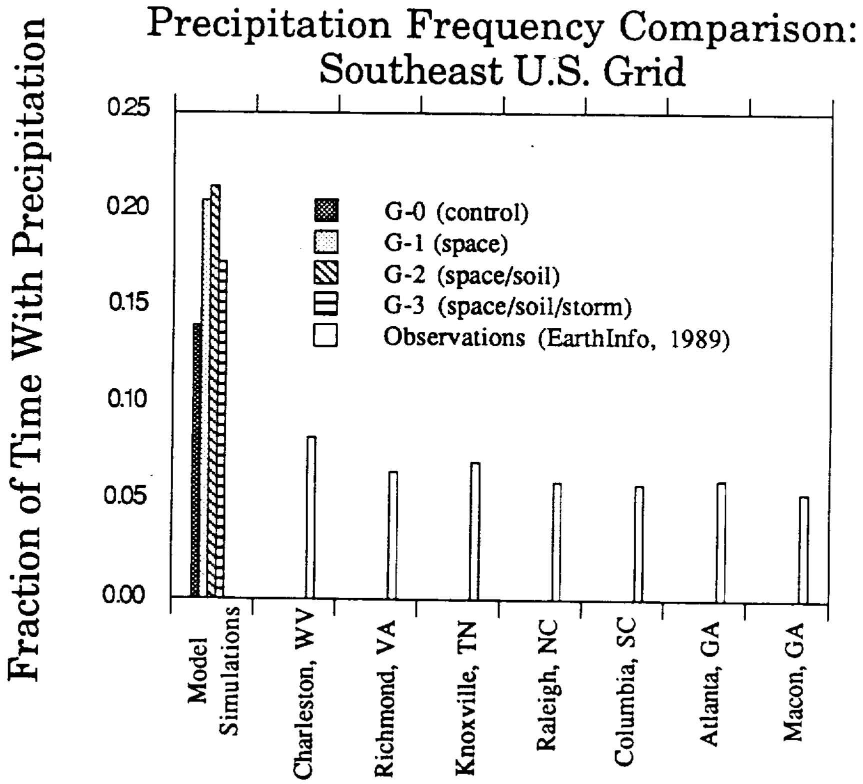

Figure 3.25a Comparison of Southeast U.S. grid precipitation frequency with station data (based on hourly measurements)

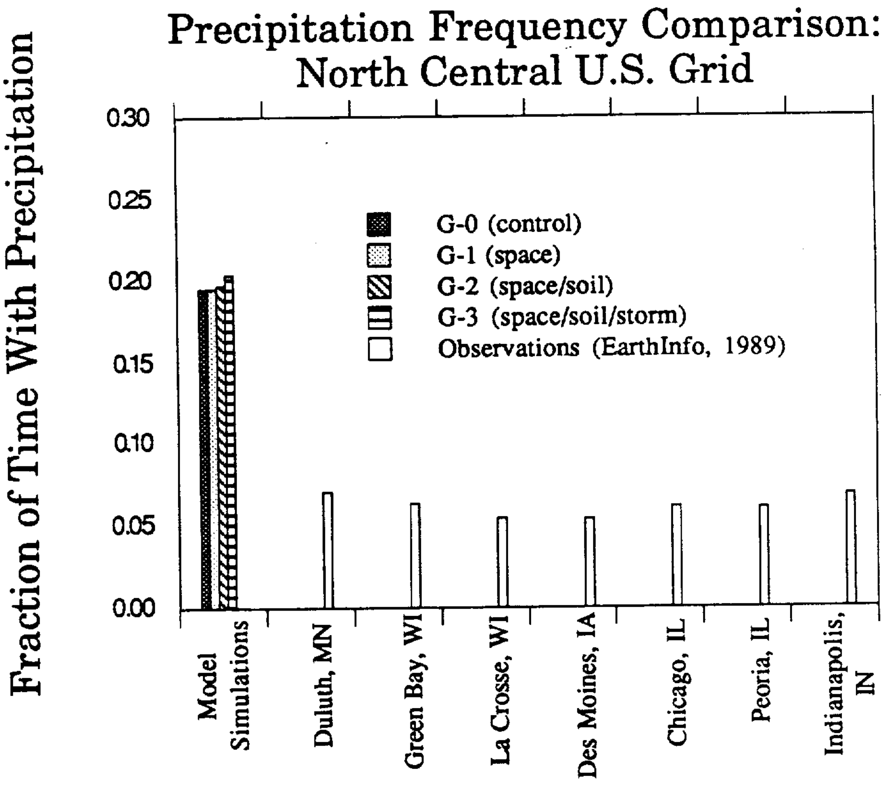

Figure 3.25b Comparison of North Central U.S. grid precipitation frequency with station data (based on hourly measurements)

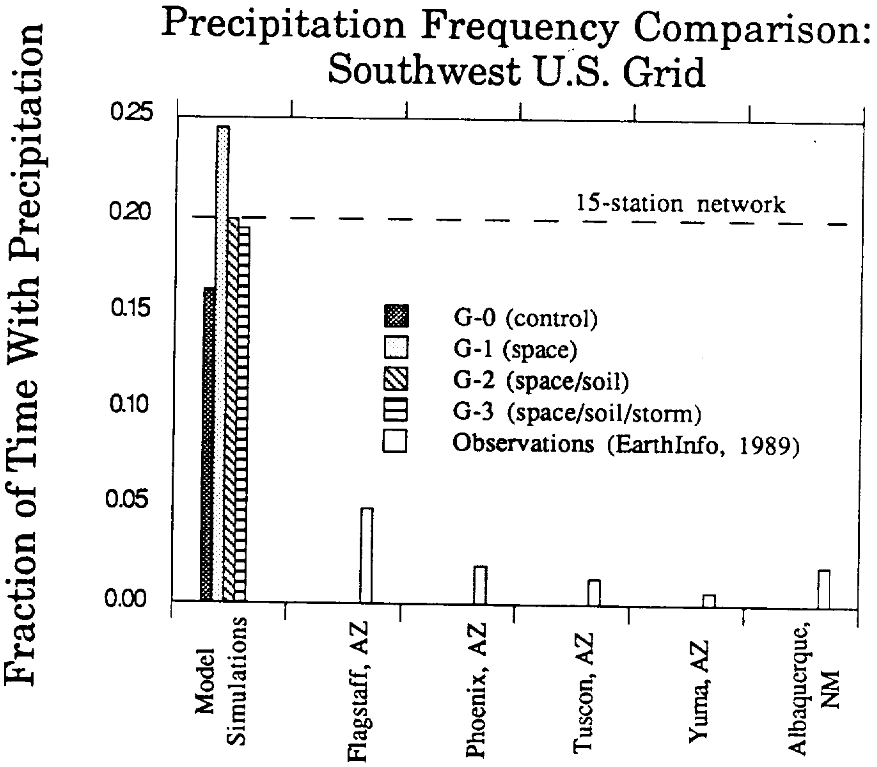

Figure 3.25c Comparison of Southwest U.S. grid precipitation frequency with station data (based on hourly measurements)

listed in Fig. 3.25c. The fraction of time with precipitation for stations enclosed in this region range from 1 percent up to nearly 5 percent. A closer look at this region reveals that, due to the spatially-concentrated form in which moist-convective rainfall is delivered, a better measure of the grid-wide probability of rain is the frequency of hours with precipitation at <u>any</u> one of the stations enclosed within the grid. For regions where rainfall is more spatially uniform and the storm coverage is over areas on the same scale as the GCM grid or larger (e.g., stratiform rainfall over the "Southeast U.S." or "North Central U.S." grids) then the average of precipitation probabilities for many stations will be equal to the probability of precipitation at any of the many included stations. Fig. 3.26 shows that in the "Southwest U.S." region (where rainstorms are of moist-convective origin and are therefore of limited spatial extent when compared with the GCM grid area) the fraction of time with precipitation is going to be different when computed as the average of the statistic for many stations, as opposed to its estimation by considering the frequency of times when there is rain at any one of many stations. In Fig. 3.26 up to fifteen stations are included for this region. The probability of precipitation is computed when groups of 1, 2, 3, ···, 15 stations are considered at a time. The figure shows that the statistic is still growing with fifteen stations but it is reaching an asymptote. The value of the statistic at that asymptote is the true probability of precipitation over the "Southwest U.S." grid and it is this statistic that should be compared with the simulation results from the GISS GCM. Such comparison is made in Fig. 3.25c with the result of considerably improved comparison between the observed and simulated probability of precipitation over the "Southwest U.S." grid.

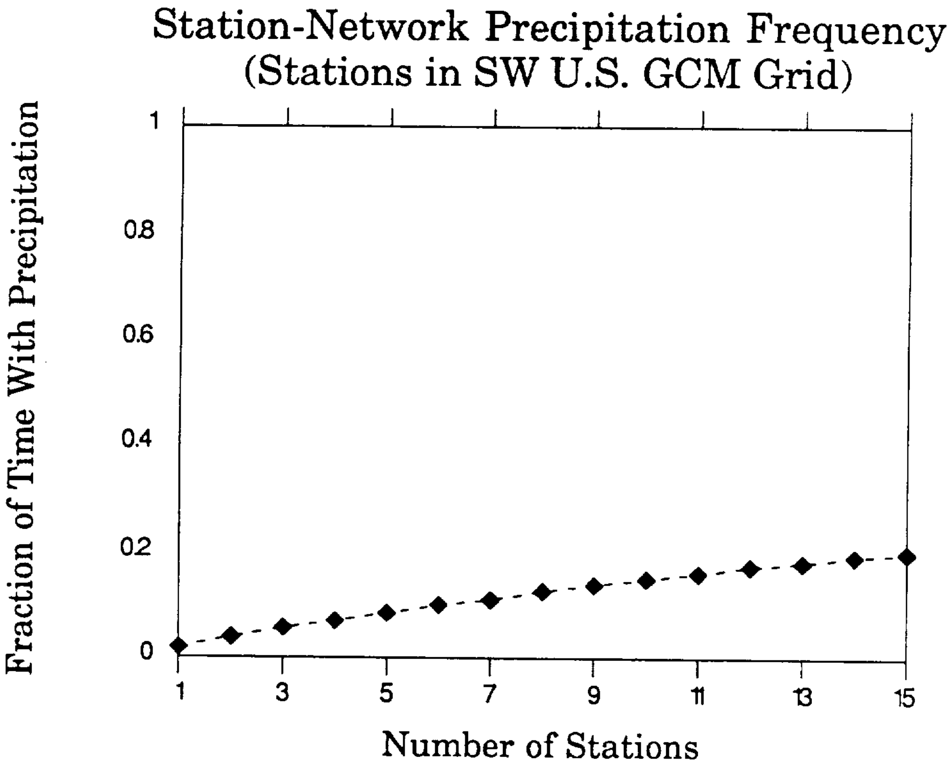

Figure 3.26 Rainfall frequency derived from hourly station data within a Southwest U.S. GCM grid square for various station–network arrays.

(Data from EarthInfo, 1989)

The GCM–simulated values of regional precipitation are not designed to replicate, nor should they be compared with point–measurements. The higher order statistics (such as variance, autocorrelation, etc.) of station precipitation are thus not useful in validating GCMs. Usually the mean precipitation values for grid regions are used in validation studies. As evident in Figs. 3.25a–c and Fig. 3.26, the frequency of time–periods with precipitation is an additional (non–parametric) measure of the precipitation process which may be used to validate models. Fig. 3.26 shows that considerably more stations are needed to define robust statistics. Further study is needed to make use of this measure in validating GCMs.

A final observation of hydrologic significance is that potential evaporation in the GISS GCM is generally very high (see Figs. A.6a–d). Although outside the scope of this work, we direct the reader to Milly (1991) for an analysis of alternate formulations of potential evaporation in GCMs.

D. Discussion

We have implemented the landsurface hydrology parameterization of Entekhabi and Eagleson (1989a) along with the soil moisture diffusion parameterization based on Abramopoulos et al. (1988) into the GISS GCM. The results of three new simulations compared against a Control Run and observations have been presented. The following is a discussion and evaluation of these results.

The first point to be made is that the new parameterizations are both, to a much greater degree than the current GISS II landsurface, physically–based. The general problem encountered when improving the model by incorporating more realistic schemes, however, is a requirement for large amounts of computing time. The times required for our simulations were as follows: The Control Run requires roughly one hour CPU time per month of simulation on the IBM mainframe computer. Run G–1 increased this time by approximately 10%, and Runs G–2 and G–3, with the new soil diffusion scheme, required about 25% more CPU time than the Control Run. The major improvements in the simulations resulted from the inclusion of spatial variability. It must be noted that the spatial variability and soil diffusion algorithms may be further optimized and their numerics improved in the computer code. Thus there is the prospect of much less additional cost if the new algorithms are optimally adapted to the GISS GCM. It has been demonstrated that with a fractional wetting parameter for moist–convective type rainfall, the inclusion of spatial variability results in remarkable improvements of the landsurface hydrology in all of the global, zonal, continental, and large river basin domains.

Another important finding is the strong sensitivity of the correct model hydrologic balance on the runoff generation mechanism. Evaporation is only reduced by a reduction in available soil moisture through increased runoff. In this way, runoff is a major control on actual evaporation in the GISS GCM.

Precipitation has been seen to be rather poorly represented in the 8 × 10 degree resolution of the GISS GCM, as comparisons have been made with many independent data sets. Russell and Miller (1990) show the 4 × 5 degree resolution version of the GISS GCM has considerably improved precipitation climatology.

The extent to which the landsurface parameterization can affect rainfall was seen most clearly in the globally averaged water balance schematics of Fig. 3.12. Roughly a 10% reduction resulted over the landsurface due to the increased runoff in Run G–3. However, this is by no means enough to bring precipitation in its distribution over the earth into agreement with observations. The global average result is good but hides the fact that precipitation is actually too low in the tropics and too high in the northern hemisphere. In most areas, errors in precipitation create errors in the water balance which are impossible to correct with any landsurface parameterization. Both the magnitude and temporal and spatial structure of rainfall generation are in need of improvement in the atmospheric branch before the landsurface water balance will be able to agree with data. Another factor to consider is the interannual variability in the model climate and the representativeness of a limited number of years of simulation.

One key area which is of concern when altering the water balance is the effect on the heat balance. The diagnostic most available for comparison is the surface air temperature. We have seen that in the zonal mean, surface air temperatures have improved over the tropics and have remained unchanged elsewhere in Run G–3. This is a reflection of the improvement in evaporation over the tropics, giving a more accurate latent heat flux.

One last point to consider is the lack of data for the two key spatial variability parameters. These are 1) the coefficient of variation (cv_s) of soil moisture over a grid square, and 2) the fractional wetting of moist–convective and large scale supersaturation type rainfall. For all simulations, the cv_s of soil moisture was set equal to 1.0. Because of constraints on computer time, no GCM simulation tested this sensitivity in the full interactive global case. This needs to be done in the future.

The fractional wetting parameter however was tested since it obviously caused strong sensitivity in off–line analyses. This parameter intuitively ought to have a dependence on convection, topography, vicinity of oceans, climate type, and wind patterns, among other things. We explored only a globally uniform setting of this parameter and found strong sensitivity. Further consideration ought to be given here for both types of rainfall. One further argument in support of a lower value for use in the model is the higher frequency of simulated grid rainfall when compared to station observations. If grid rainfall occurs more frequently than station data indicate, one could reason that the grid precipitation is perhaps accounting for many events each of fractional–grid scale. The fractional wetting κ needs to be related to the fraction (by mass) of the grid air column experiencing convection. This latter fraction is explicitly solved for by Kuo–type moist convection schemes. In the next generation of the GISS GCM, the land surface hydrology including subgrid scale spatial variability may be coupled with the moist convection scheme in this manner. The soil moisture diffusion scheme of Abramopoulos et al. (1988) also needs to be implemented along with the parallel soil heat diffusion algorithm. Global data sets on soils, vegetation canopy, surface topography, roughness, etc. need to be incorporated as well into the improved landsurface hydrology schemes.

Chapter IV

Conclusions and Recommendations for the GISS GCM

A. Summary of Research Results

We have implemented improved landsurface hydrological parameterizations into the GISS GCM and have analyzed their effects on simulated global climate. The statistical–dynamical parameterization of Entekhabi and Eagleson (1989a) is used for its critical advantage over current GCM hydrological schemes due to the inclusion of subgrid scale spatial variability. The soil moisture diffusion parameterization of Abramopoulos et al. (1988) is used to provide more realistic deep soil water storage and moisture diffusion. Descriptions of these parameterizations are given in Chapter I along with a description of an efficient one–dimensional Screening Model with which sensitivities of the parameterizations were evaluated prior to implementation in the full three–dimensional GISS GCM.

The results of sensitivity simulations with a three layer soil column in the Screening Model are presented in Chapter II. These simulations investigate sensitivity to soil storage capacity and heat capacity (i.e., soil layer thicknesses), sensitivity to groundwater percolation from the lowest soil layer, and sensitivity to transpiration extraction from lower soil layers. It is determined that there is strong sensitivity of mean simulated climate to the thickness of the top soil layer. The top soil layer thickness also has a strong effect on amplitudes of the diurnal heat cycle. For the conditions tested here, it is found that increasing the top soil layer thickness created in general, an increasingly drier climate while dampening the diurnal heat cycle. Increasing the *total* soil column thickness, while having only a small effect on mean climate, has a significant effect on the annual *range* of climatic variables. The annual ranges of soil moisture and temperature are dampened as the total soil column depth increases. Based on these results, the top two soil layer thicknesses are held constant over the globe and the lowest soil layer thickness adjusted to preserve field capacities of GISS–II upon implementation of the Abramopoulos et al. (1988) soil moisture diffusion scheme into the GISS GCM.

With regard to groundwater percolation, it is found that for conditions of the Screening Model simulated climate the sensitivity is significant mainly for light textured soils. Simulations with the GISS GCM use a no–flux lower soil boundary condition in the absence of terrain and topography data, and adequate conceptualization of percolation when considering large areas.

The Screening Model simulations testing the effects of transpiration from lower soil layers show strong sensitivity to the distribution of roots in the soil layers. The lower soil layers tend toward excessive drying even with moderate fractions of roots in those layers. Also, mean climate is affected most strongly by transpiration in the setting of a deep soil column. Lacking a firm data base for root distributions in the soil, the choice for distribution used in the GISS GCM is based on the Screening Model results and it is set at 85% of the roots in the upper soil layer, 10% in the middle layer, and 5% in the lowest layer. This distribution produced the most realistic results in the Screening Model.

The preceding discussion now leads to the main focus of this research, which is the effects of new landsurface hydrological parameterization in the GISS GCM. The parameterizations of Entekhabi and Eagleson (1989a) and Abramopoulos et al. (1988) are both physically–based in contrast with the current landsurface hydrological parameterization of the GISS GCM.

Entekhabi and Eagleson (1989a) account for spatial variability in the key parameters of rainfall and soil moisture and incorporate realistic equations of infiltration and exfiltration from the soil. Abramopoulos et al. (1988) give a finite difference approximation to the governing diffusion equation for soil moisture. The additional computation requirements increase the simulation run–time by 25% with inclusion of both parameterizations (10% for the spatial variability parameterization alone). It is important, however, to note that these algorithms may be further optimized in their coding to reduce their cost.

The results shown in Chapter III.C demonstrate the major improvements in the hydrologic balance resulting from the inclusion of spatial variability. Results are compared over a wide range of spatial domains (global, zonal, continental, and river basins) using a number of data sets and improvements are verified on all fronts. Because of the nonlinear response of runoff to soil moisture and precipitation intensity when spatial variability is included, the strongest changes in hydrologic budgets occur over the tropics. Improvement in the hydrologic balance further results in improved heat balance verified most distinctly in comparisons of zonal surface air temperature over landsurface areas. The soil moisture diffusion scheme of Abramopoulos et al. (1988) is necessary for maintaining realistic annual cycles of heat and moisture. However, it has smaller effects on the total global hydrologic budget.

B. The Need for Spatial Variability

A major finding of this research is the remarkable improvement in the landsurface hydrologic balance particularly over the tropics obtained by inclusion of spatial variability (see Figures 3.13a–c). The poor agreement of the current 8° × 10° GISS–II hydrologic balance can be seen to stem mainly from a lack of runoff generation, giving simulated values much lower than those observed over landsurface areas. This allows evaporative fluxes to exceed by a large margin the evaporation values derived from observations. Based on this research, it seems most likely that the lack of runoff generation in the current GISS–II in the tropics is due to the fact that precipitation is currently modeled as being *uniform* over the entire grid square. This results in low average intensities which generate far less runoff (if physically–based infiltration equations are employed) than would be obtained by spatially *heterogeneous* rainfall, having some areas of concentrated rainfall producing larger amounts of runoff and some areas of lesser rainfall intensity producing less runoff. This coupled with spatial variability in soil moisture in the formulation of Entekhabi and Eagleson (1989a) has been shown here to produce results in better agreement with observations. Regardless of the levels of detail which may be pursued in modeling landsurface hydrology, without the element of spatial variability it seems unlikely that the global hydrologic balance will be represented adequately in GCMs.

C. Future Research

In order to further improve the landsurface hydrological parameterization of GCMs several avenues of research need to be explored. First, it is determined that there is very strong sensitivity in the spatial variability parameterization to the rainfall fractional wetting parameter κ. As mentioned, this parameter ought to have a dependence on the air column convection, topography, seasonality, and prevailing climate among other factors. While simulations here simply used one value of κ for moist–convective rainfall and one for supersaturation rainfall, alternate formulations need to be investigated. The same is true for the coefficient of variation of soil moisture cv_S.

Groundwater percolation is treated only in a very simple fashion in this work. In nature, groundwater percolation can be a major component in the hydrologic cycle and as such it needs to be investigated and its influence quantified in the context of GCMs.

In the sensitivity experiments with the One–Dimensional Screening Model, it is found that the top soil layer and the total soil depth determine the mean climate and the amplitude of its diurnal and seasonal cycles. There is a critical need to clarify this sensitivity further and develop objective methods by which the soil column may be discretized. There is also the need to search sources of data for defining this important lower boundary.

The simulations performed in the GISS GCM here have been only of a relatively short duration (maximum of five years), using fixed sea surface temperatures. Longer duration simulations may reveal trends and statistical measures by which the model could be further analyzed. An interactive ocean component ought to be used as well.

In Chapter III, a new measure is defined to be used in validating the precipitation process of the GCM model climate. Since the second–order properties (variance, covariance) of GCM–produced rainfall cannot be compared with that resulting from weather at an observation point, the new statistic defined here will be especially useful since it measures the structure of variability of the modeled rainfall without relying on second–order statistics. Together with the mean, the probability of regional precipitation may be estimated from observed data and employed in validating the precipitation climatology of GCM model climates.

Finally, because of their strong impact on the landsurface hydrologic budget, the GCM generated rainfall distributions and potential evaporation mechanism require a more thorough examination. Without the proper potential evaporation forcing and rainfall generation, the landsurface will not be able to partition these forcings accurately in order to represent the hydrologic balance.

References

Abramopoulos, F., C. Rosenzweig, and B. Choudhury, 1988: Improved ground hydrology calculations for GCMs--Soil water movement and evapotranspiration, *Journal of Climate*, *1*(*9*), 921–941.

Baumgartner, A. and E. Reichel, 1975: *The World Water Balance*, R. Oldenbourg, Munich, 179 pages.

Bell, K. R., B. J. Blanchard, T. J. Schmugge, and M. W. Witczk, 1980: Analysis of surface moisture variations within large–field sites, *Water Resour. Res.*, *16*(*4*), 796–810.

Brooks, R. H. and A. T. Corey, 1966: Properties of porous media affecting fluid flow, *Journal Irrig. Drain. American Soc. Civil Eng.*, *IR2*, 61–88.

Brubaker, K. L., D. Entekhabi, and P. S. Eagleson, 1991: Atmospheric water vapor transport: estimation of continental precipitation recycling and parameterization of a simple climate model, *MIT Department of Civil Engineering, Ralph M. Parsons Laboratory Report No. 333*, 166 pages.

Budyko, M. I. (ed.), 1963: *Atlas of the Heat Balance of the Globe*, Moscow, 69 pages.

Budyko, M. I., 1978: The heat balance of the earth, in *Climatic Change*, edited by J. Briggin, Cambridge University Pres, Cambridge, pp. 85–113.

Dickinson, R. E., A. Henderson–Sellers, P. J. Kennedy, and M. F. Wilson, 1986: *Biosphere–Atmosphere Transfer Scheme* (*BATS*) *for the NCAR Community Climate Model*, NCAR Technical Note TN–275STR, 69 pages.

Eagleson, P. S. and Q. Wang, 1985: Moments of catchment storm area, *Water Resour. Res.*, *21*(*8*), 1185–1194.

EarthInfo NCDC (National Climate Data Center) hourly precipitation records, 1989: (updated annually), EarthInfo, Boulder, CO.

Entekhabi, D. and P. S. Eagleson, 1989a: Landsurface hydrology parameterization for atmospheric general circulation models including subgrid scale spatial variability, *Journal of Climate* *2*(*8*), 816–831.

Entekhabi, D. and P. S. Eagleson, 1989b: Landsurface hydrology parameterization for atmospheric general circulation models: inclusion of subgrid scale spatial variability and screening with a simple climate model, *MIT Department of Civil Engineering, Ralph M. Parsons Laboratory Report No. 325*, 195 pages.

Epstein, E., 1973: Roots, *Scientific American*, *228*(*5*), 48–58.

Hansen, J., G. Russell, D. Rind, P. Stone, A. Lacis, S. Lebedeff, R. Ruedy and L. Travis, 1983: Efficient three–dimensional global models for climate studies: models I and II, *Monthly Weather Review*, *111*(*4*), 609–662.

Henderson–Sellers, A. and K. McGuffie, 1987: *A Climate Modelling Primer*, J. Wiley and Sons, New York, 217 pages.

Henning, D., 1989: *Atlas of the Surface Heat Balance of the Continents*, Gebruder Borntraeger, Berlin, 402 pages.

Hoffman, R. N., 1981: A computer program which calculates radiative fluxes and heating rates in model atmospheres, *Scientific Report No. 4, Project for the Study of Climatic Fluctuations, Volcanic Aerosols, and Carbon Dioxide Changes,* Department of Meteorology and Physical Oceanography, Massachusetts Institute of Technology, 124 pages.

Koster, R. D., P. S. Eagleson, and W. S. Broeker, 1988: Tracer water transport and subgrid precipitation variation within atmospheric general circulation models, *MIT Department of Civil Engineering, Ralph M. Parsons Laboratory Report No. 317*, 124 pages.

Legates, D. R. and C. J. Willmott, 1990: Mean seasonal and spatial variability in global surface air temperature, *Theoretical nd Applied Climatology, 41*, 11–21.

Manabe, S., 1969: Climate and the ocean circulation: I. The atmospheric circulation and the hydrology of the earth's surface, *Monthly Weather Review, 97*, 739–774.

Matthews, E., 1983: Global vegetation and land use: new high resolution data bases for climate studies, *J. Clim. Appl. Met.*, *22*, 474–487.

Milly, P. C. D., 1991: Personal communication.

Owe, M., E. B. Jones, and T. J. Schmugge, 1982: Soil moisture variation patterns observed in Hand County, South Dakota, *Water Resour. Bull.*, *18*(*6*), 949–954.

Parlange, J.–Y., M. Vauclin, R. Haverkamp, and I. Lisle, 1985: Note: The relation between desorptivity and soil–water diffusivity, *Soil Science, 139*, 458–461.

Philip, J. R., 1957a: The theory of infiltration: 1. The infiltration equation and its solution, *Soil Science, 83*, 345–357.

Philip, J. R., 1957b: The theory of infiltration: 4. Sorptivity and algebraic infiltration equations, *Soil Science, 84*, 257–264.

Russell, G. L. and J. R. Miller, 1990: Global river runoff calculated from a global atmospheric general circulation model, *J. of Hydrology, 117*, 241–254.

Schutz, C. and W. Gates, 1971: Global climatic data for surface, 800 mb, 400 mb, Reports R–915–ARPA, R–915/1–ARPA, R–1029–ARPA, Rand Corp., Santa Monica.

Sellers, P. J., Y. Mintz, Y. C. Sud, and A. Delcher, 1986: A simple biosphere model (SiB) for use within General Circulation Models, *J. Atmos. Sci.*, *43*(*6*), 505–531.

Spangler, W., and Jenne, 1988: World monthly surface station climatology (and associated datasets), NCAR, Boulder, CO.

Stone, P. H. and J. S. Risbey, 1990: On the limitations of General Circulation Climate Models, *Center for Global Change Science Report #2*, Massachusetts Institute of Technology, 12 pages.

Warrilow, D. A., A. B. Sangster, and A. Slingo, 1986: Modelling of land surface processes and their influence on European climate, U. K. Meteorological Office, DCTN 38, 94 pages, available from the U. K. Meteorological Office.

Washington, W. M., and G. A. Meehl, 1984: Seasonal cycle experiment on the climate sensitivity due to a doubling of CO_2 with an Atmospheric General Circulation Model coupled to a simple mixed–layer ocean model, *J. Geophys. Res.*, 89, 9475–9503.

Washington, W. M. and C. L. Parkinson, 1986: An Introduction to Three–Dimensional Climate Modeling, University Science Books, Mill Valley, CA, 422 pages.

Zobler, L. and T. K. Cary, 1986: A World soil file for global climate modeling, *NASA Technical Memorandum #87802,* New York.

Zubenok, L. I., 1970: Improved scheme of the water balance of continents, in *Heat Balance*, edited by T. G. Berlyand, Hydrometeorological Press, Leningrad.

Appendix

A. Seasonal Fields of Simulated Hydrologic Diagnostics

The following figures (A.1.a through A.6.d) show the seasonal fields of simulated precipitation, evaporation, surface runoff, relative surface soil saturation, surface air temperature, and potential evaporation for the simulations G–0 through G–3 (simulations with the GISS GCM). The presentation format gives the Control Run (G–0) first in *actual* diagnostic values followed by fields of the *differences* between each of the simulations G–1 through G–3 and the Control Run.

B. List of Appendix Figures

Precipitation Fields

Evaporation Fields

Runoff Fields

Soil Saturation Fields

Figure A.4.a	Seasonal relative surface soil moisture fields (%) of Control Run (G–0)
Figure A.4.b	Seasonal relative surface soil moisture fields (%) of Run G–1 (presented as [(G–1)– Control])
Figure A.4.c	Seasonal relative surface soil moisture fields (%) of Run G–2 (presented as [(G–2)– Control])
Figure A.4.d	Seasonal relative surface soil moisture fields (%) of Run G–3 (presented as [(G–3)– Control])

Surface Air Temperature Fields

Figure A.5.a	Seasonal surface air temperature fields (C) of Control Run (G–0)
Figure A.5.b	Seasonal surface air temperature fields (C) of Run G–1 (presented as [(G–1) – Control])
Figure A.5.c	Seasonal surface air temperature fields (C) of Run G–2 (presented as [(G–2) – Control])
Figure A.5.d	Seasonal surface air temperature fields (C) of Run G–3 (presented as [(G–3) – Control])

Potential Evaporation Fields

Figure A.6.a	Seasonal potential evaporation fields (mm/day) of Control Run (G–0)
Figure A.6.b	Seasonal potential evaporation fields (mm/day) of Run G–1 (presented as [(G–1) – Control])
Figure A.6.c	Seasonal potential evaporation fields (mm/day) of Run G–2 (presented as [(G–2) – Control])
Figure A.6.d	Seasonal potential evaporation fields (mm/day) of Run G–3 (presented as [(G–3) – Control])

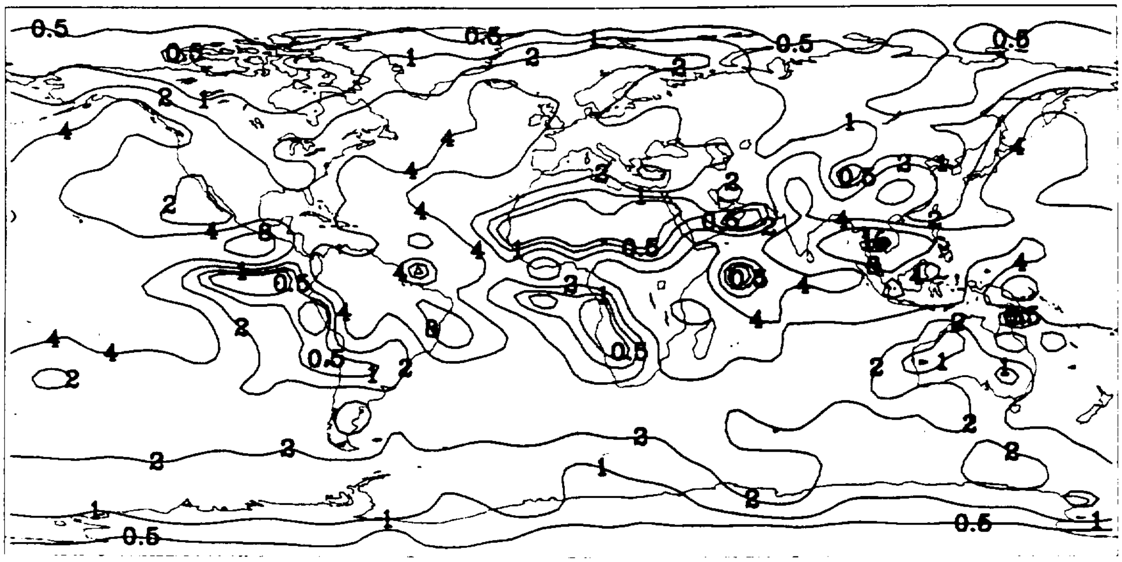
CONTROL (G–0) DJF PRECIPITATION (MM/DAY)

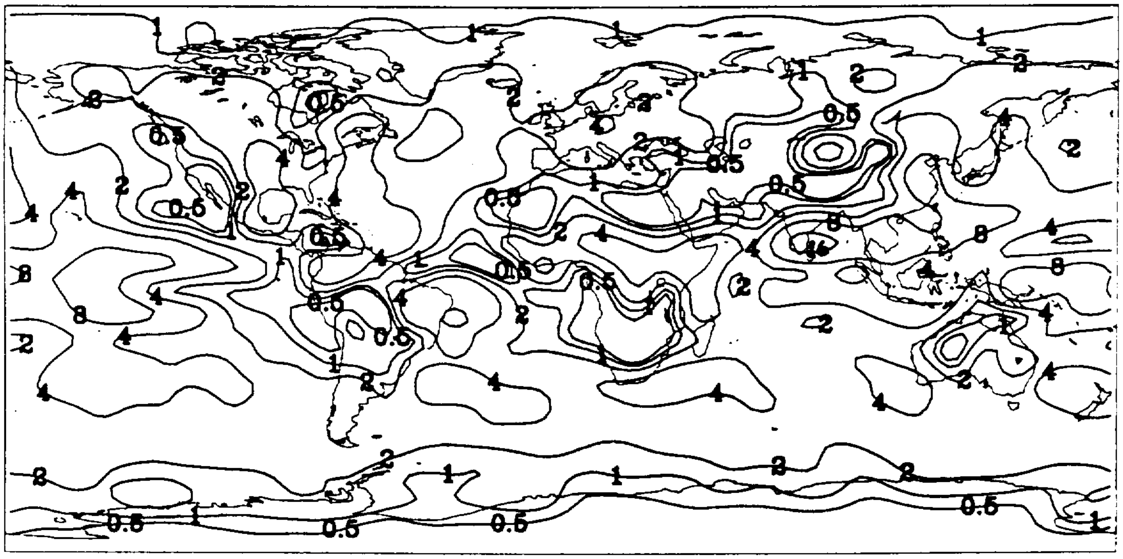
CONTROL (G–0) JJA PRECIPITATION (MM/DAY)

Figure A.1.a Seasonal precipitation fields (mm/day) of Control Run (G–0)

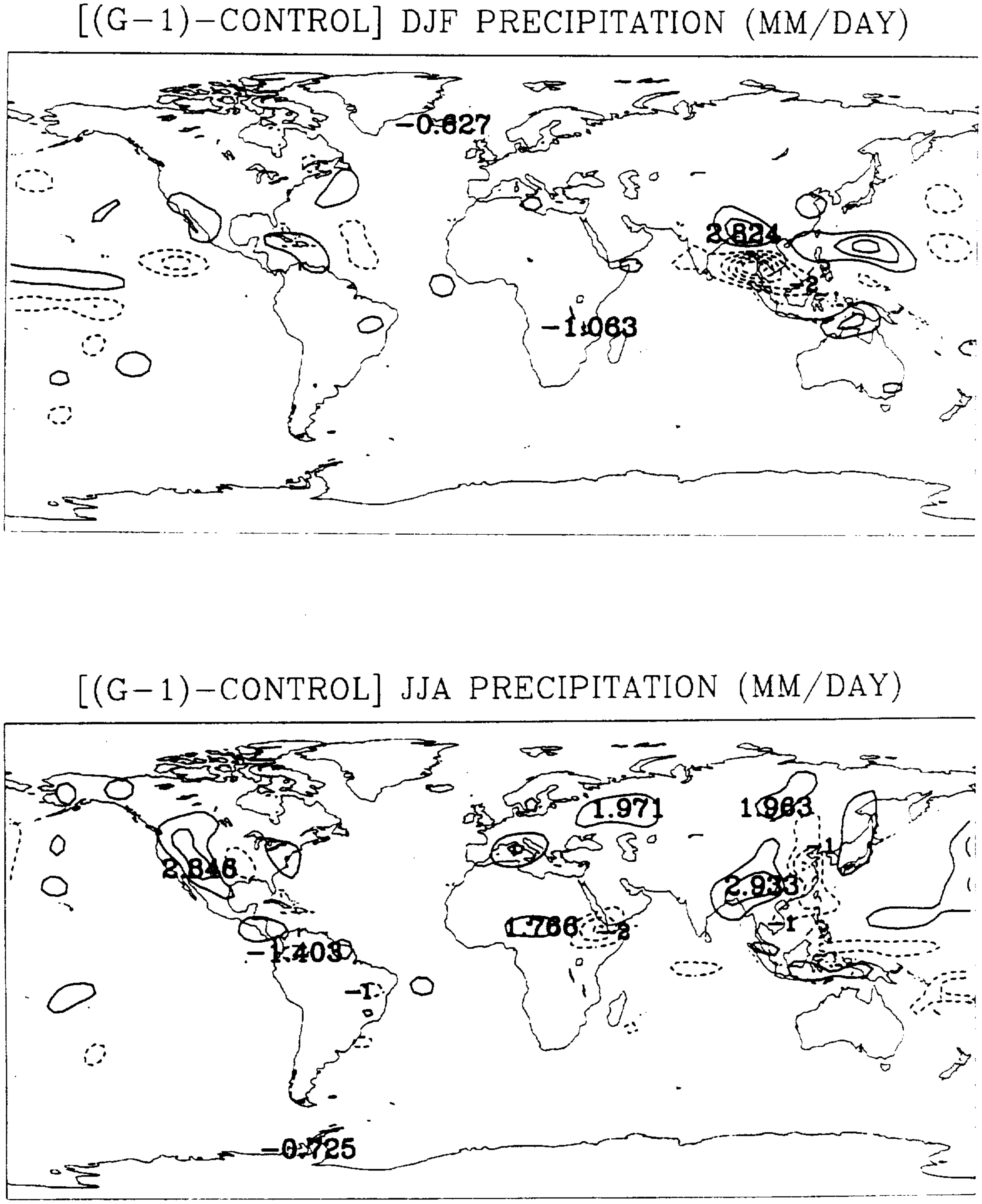

Figure A.1.b Seasonal precipitation fields (mm/day) of G–1 (presented as [(G–1) – Control])

[(G-2)-CONTROL] DJF PRECIPITATION (MM/DAY)

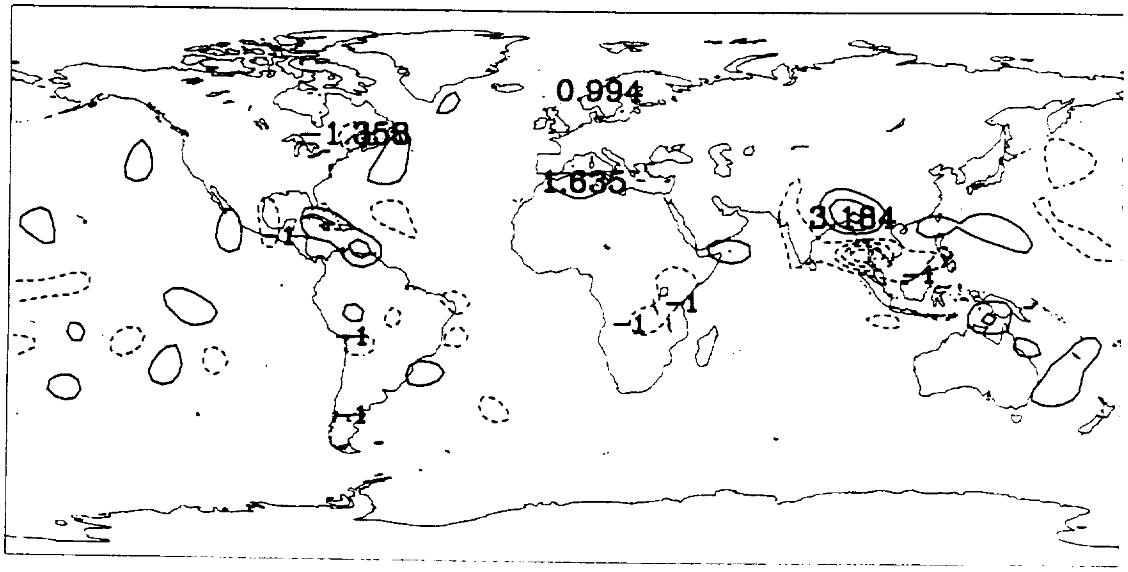

[(G-2)-CONTROL] JJA PRECIPITATION (MM/DAY)

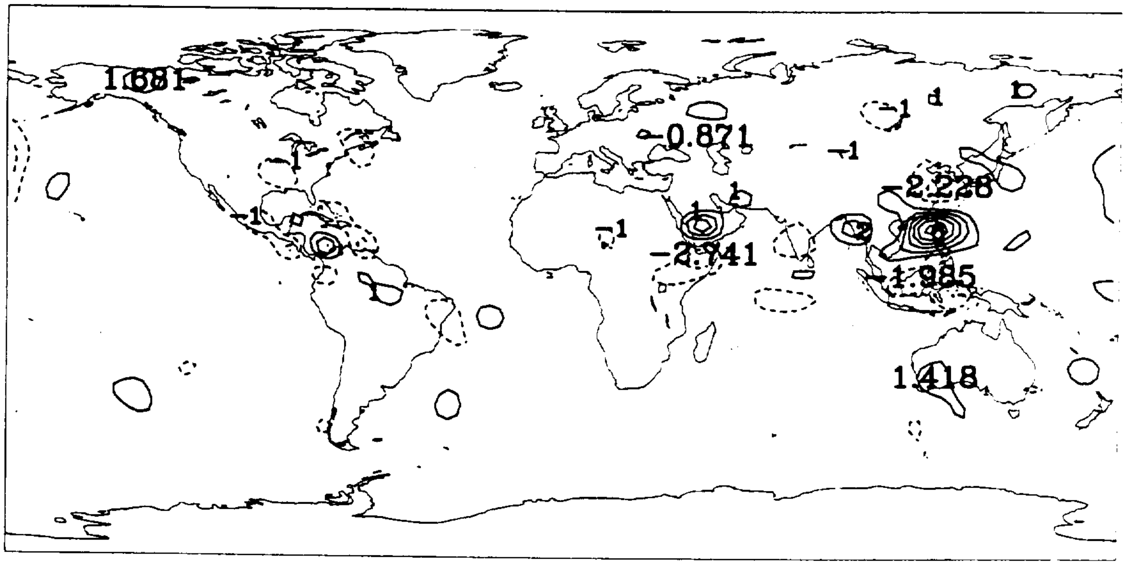

Figure A.1.c Seasonal precipitation fields (mm/day) of Run G-2 (presented as [(G-2) - Control])

[(G−3)−CONTROL] DJF PRECIPITATION (MM/DAY)

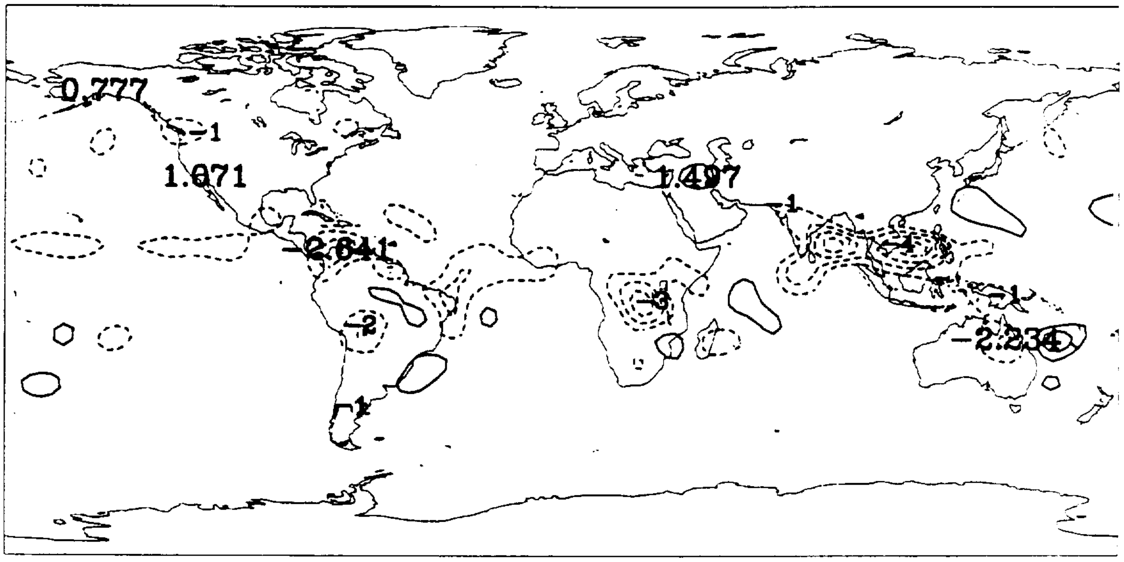

[(G−3)−CONTROL] JJA PRECIPITATION (MM/DAY)

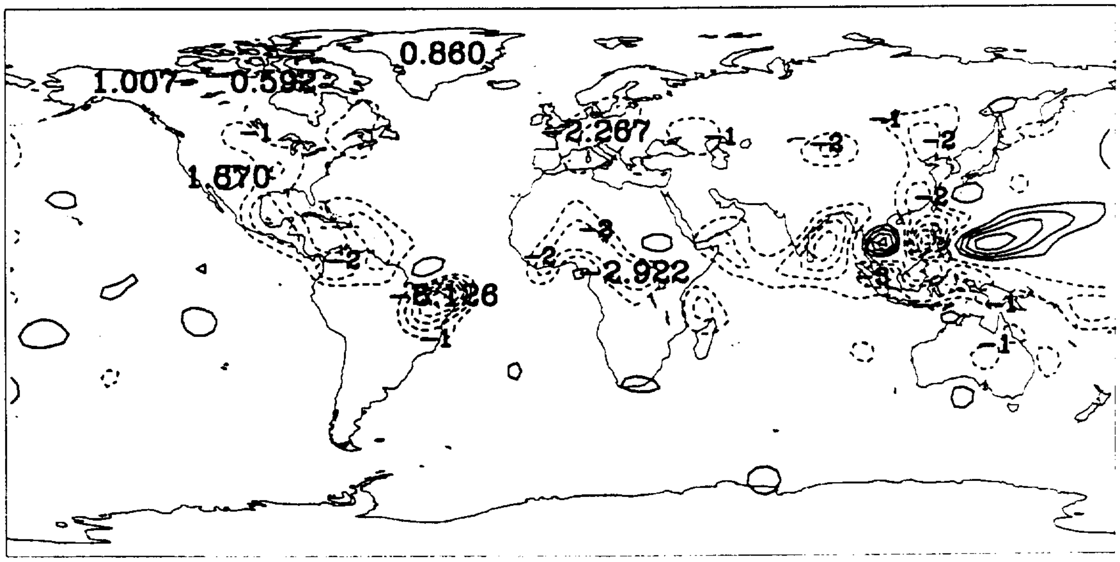

Figure A.1.d Seasonal precipitation fields (mm/day) of Run G−3 (presented as [(G−3) − Control])

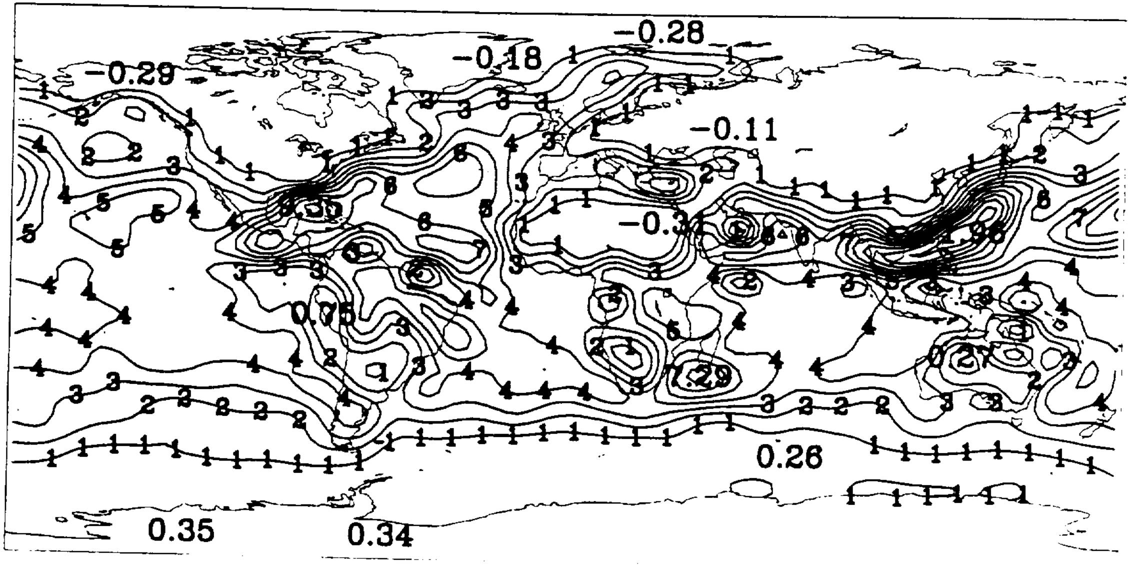

CONTROL DJF EVAPORATION (MM/DAY)

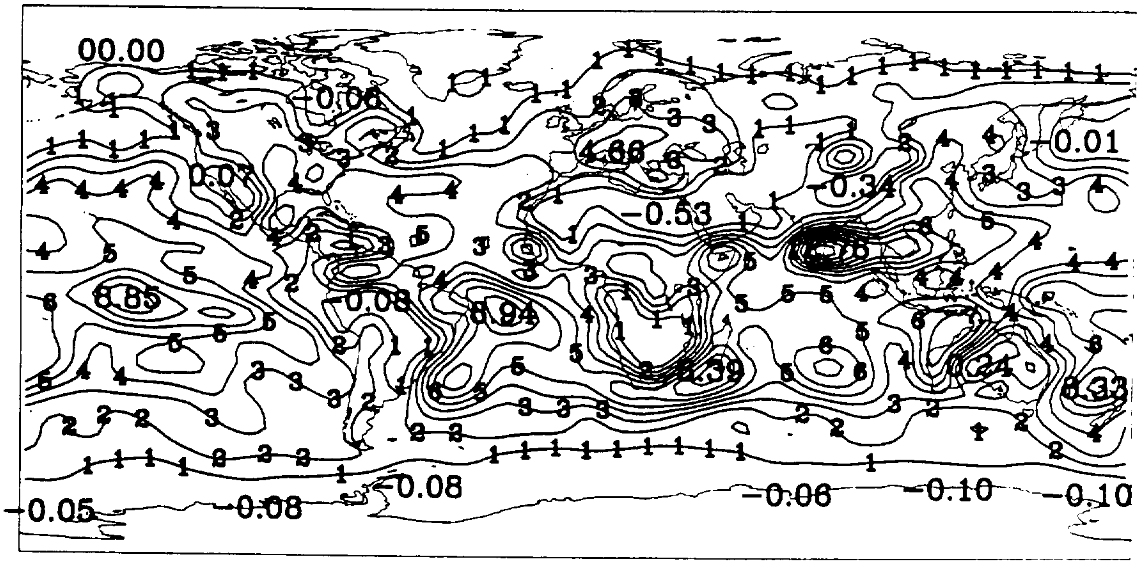

CONTROL JJA EVAPORATION (MM/DAY)

Figure A.2.a Seasonal evaporation fields (mm/day) of Control Run (G–0)

[(G-1)-CONTROL] DJF EVAPORATION (MM/DAY)

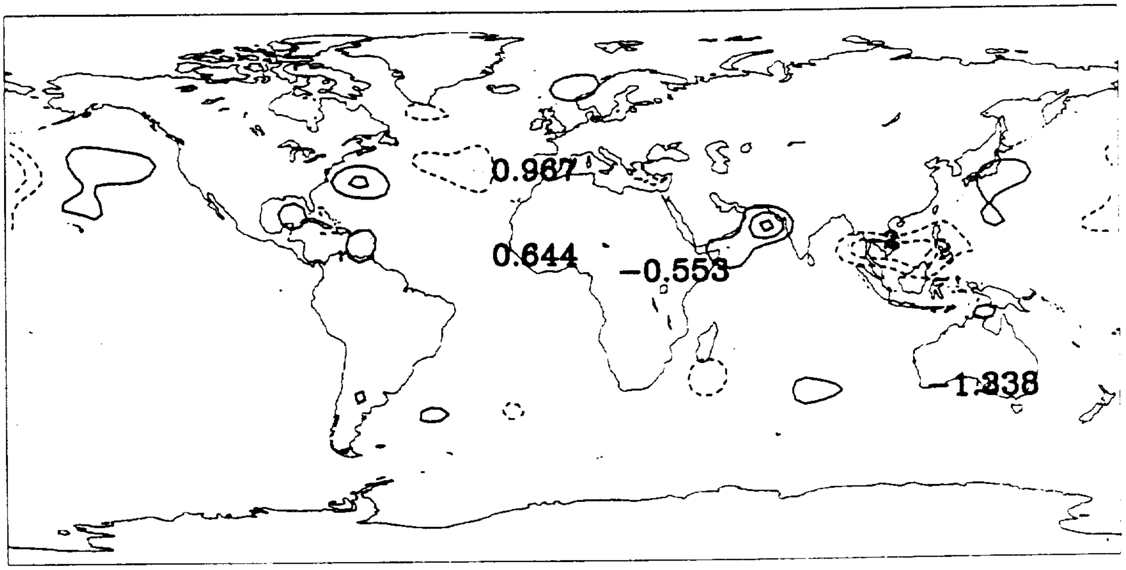

[(G-1)-CONTROL] JJA EVAPORATION (MM/DAY)

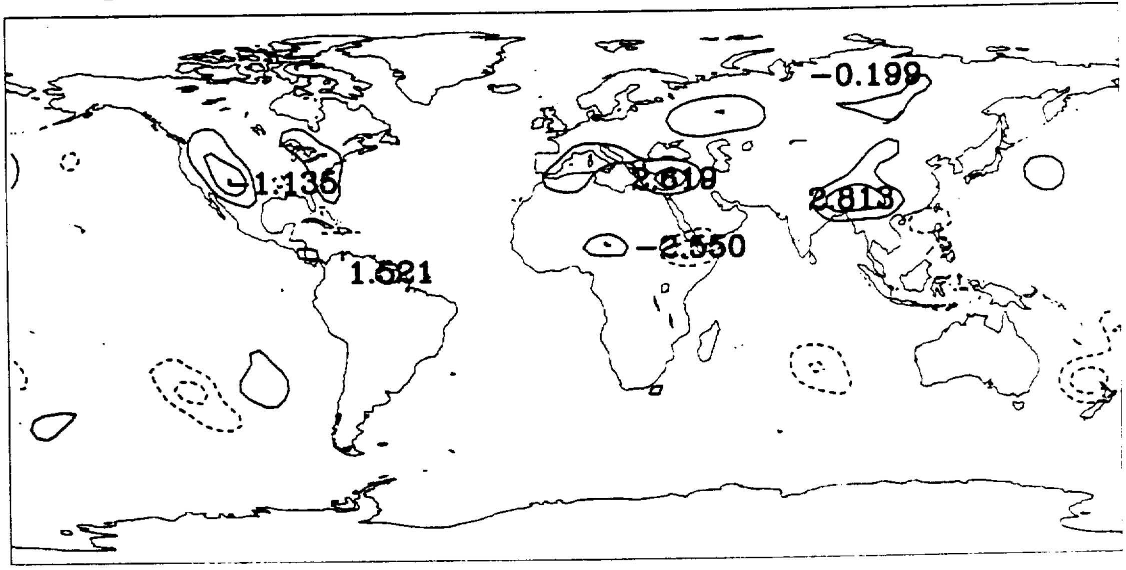

Figure A.2.b Seasonal evaporation fields (mm/day) of Run G-1 (presented as [(G-1) - Control])

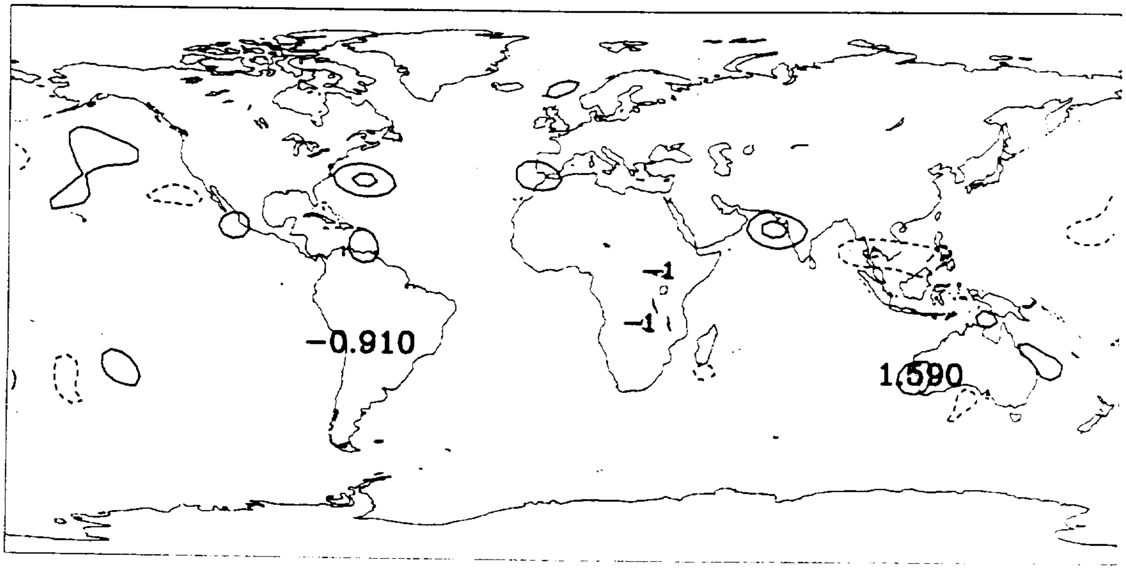

[(G-2)-CONTROL] DJF EVAPORATION (MM/DAY)

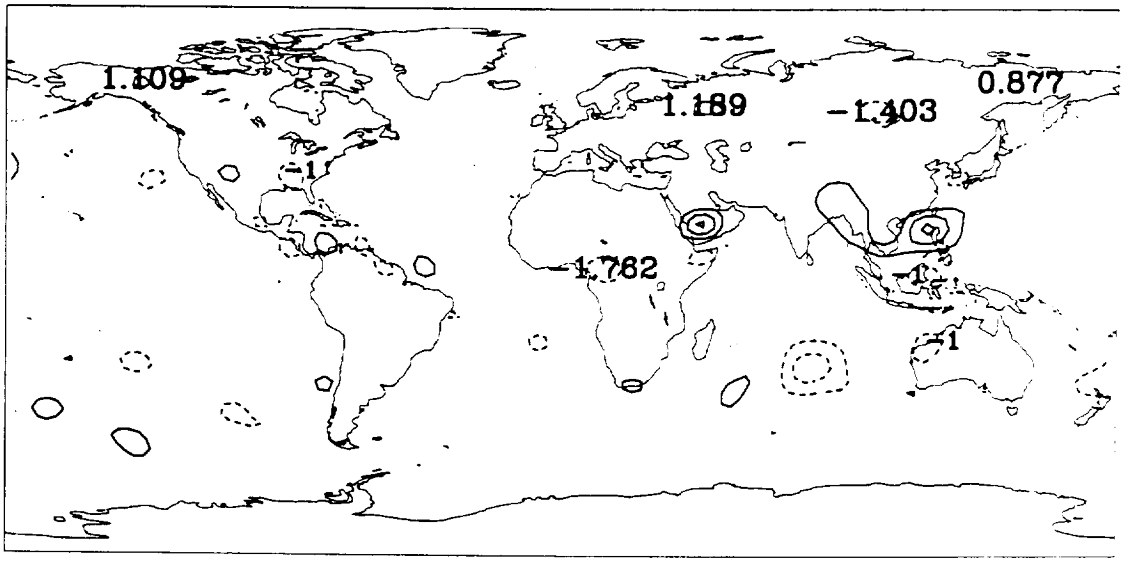

[(G-2)-CONTROL] JJA EVAPORATION (MM/DAY)

Figure A.2.c Seasonal evaporation fields (mm/day) of Run G-2 (presented as [(G-2) - Control])

[(G−3)−CONTROL] DJF EVAPORATION (MM/DAY)

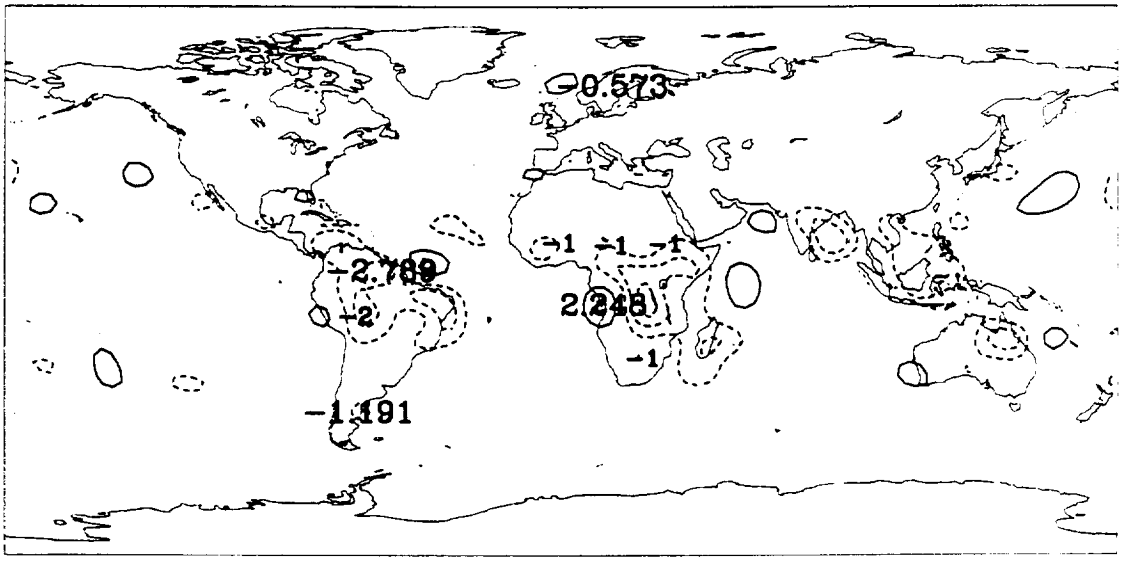

[(G−3)−CONTROL] JJA EVAPORATION (MM/DAY)

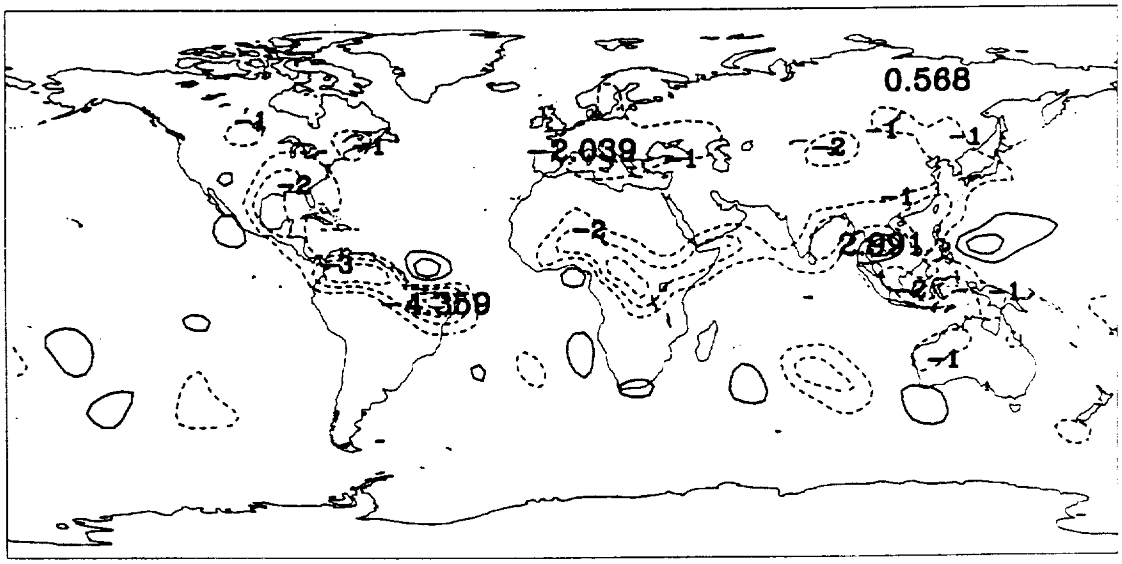

Figure A.2.d Seasonal evaporation fields (mm/day) of Run G–3 (presented as [(G–3) – Control])

CONTROL DJF SURFACE RUNOFF (MM/DAY)

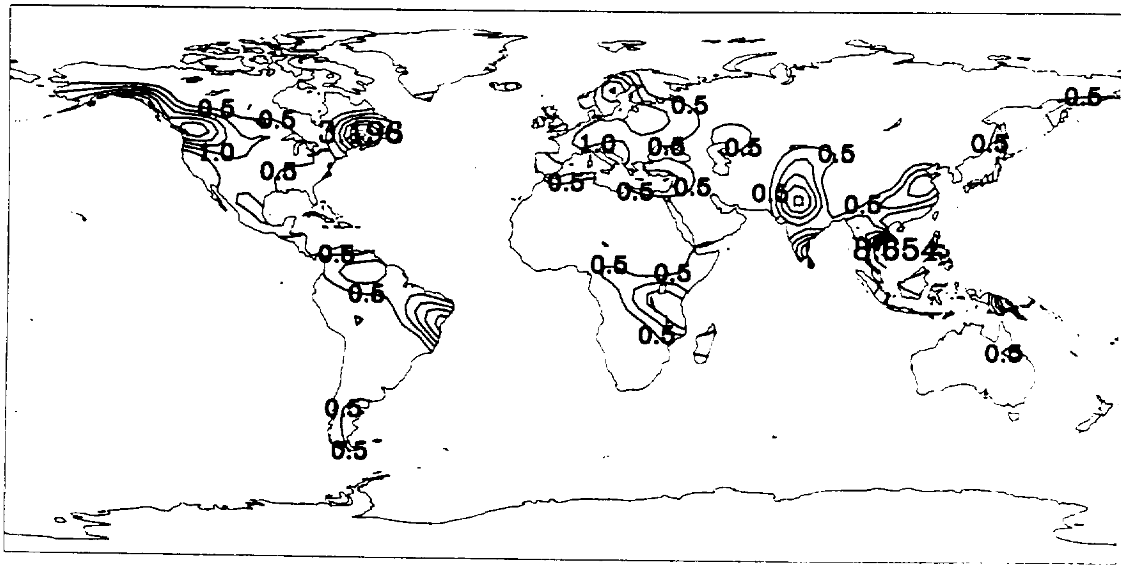

CONTROL JJA SURFACE RUNOFF (MM/DAY)

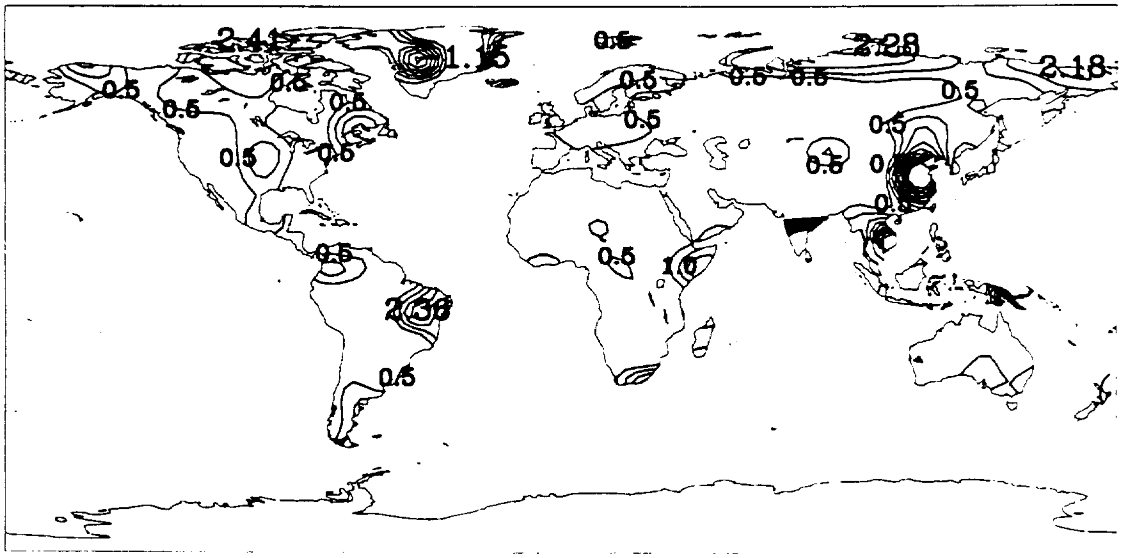

Figure A.3.a Seasonal runoff fields (mm/day) of Control Run (G–0)

[(G-1)-CONTROL] DJF RUNOFF (MM/DAY)

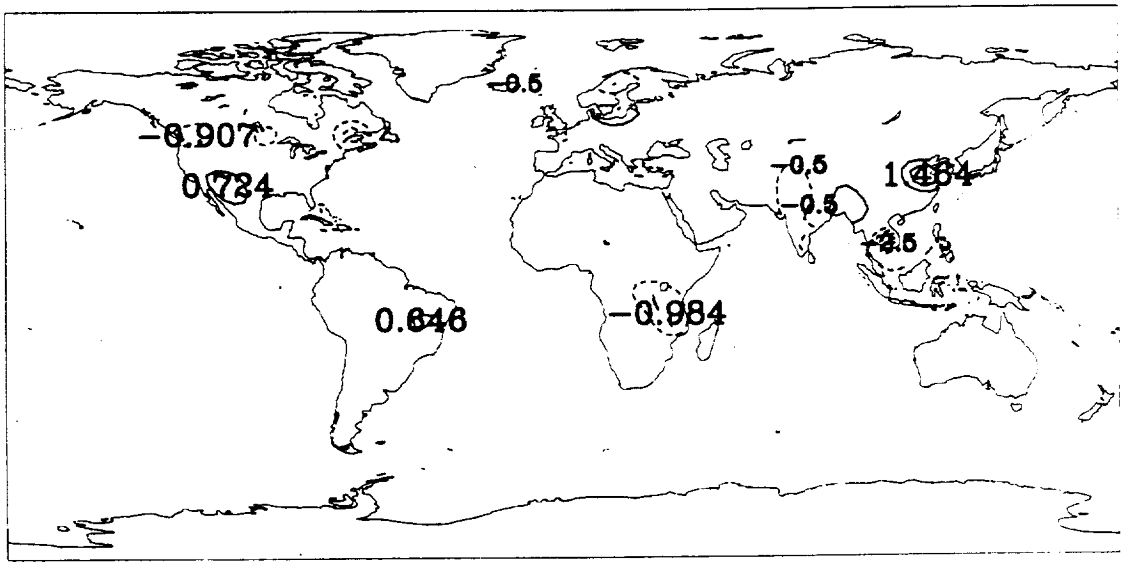

[(G-1)-CONTROL] JJA RUNOFF (MM/DAY)

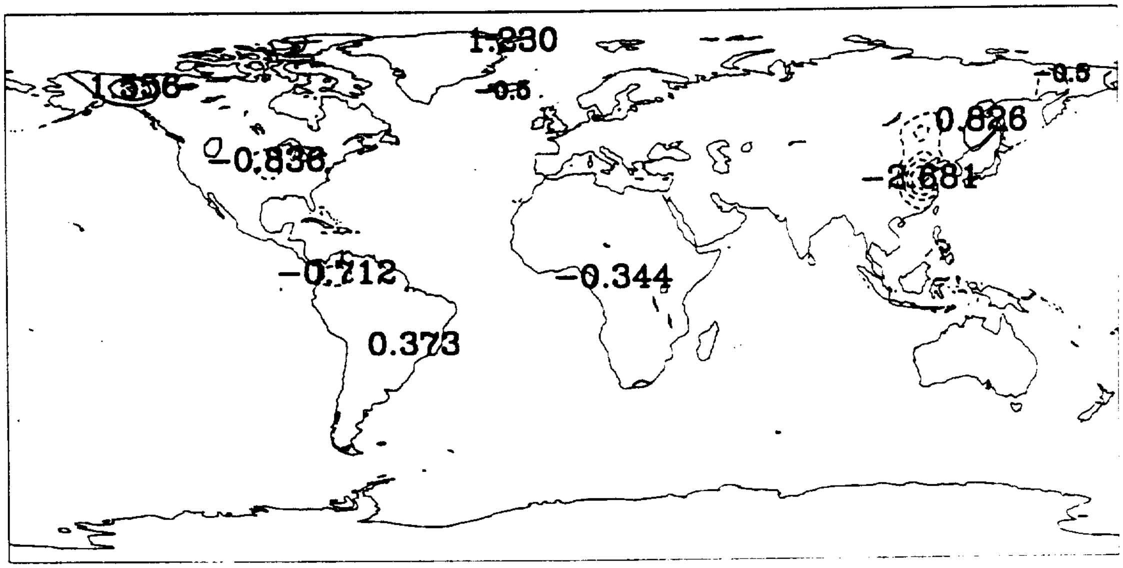

Figure A.3.b Seasonal runoff fields (mm/day) of Run G-1 (presented as [(G-1) - Control])

[(G-2)-CONTROL] DJF RUNOFF (MM/DAY)

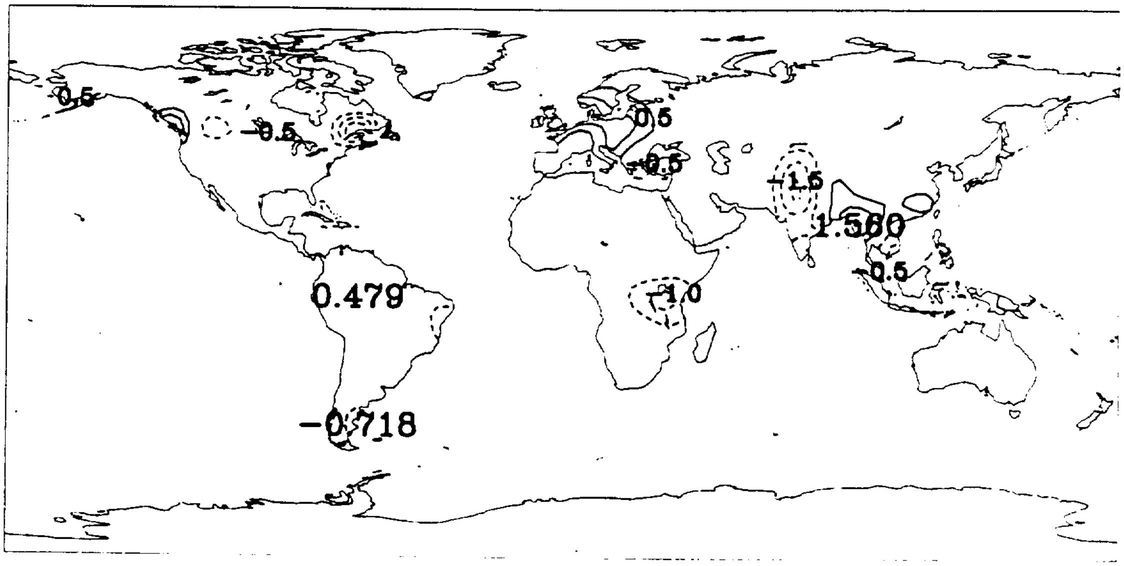

[(G-2)-CONTROL] JJA RUNOFF (MM/DAY)

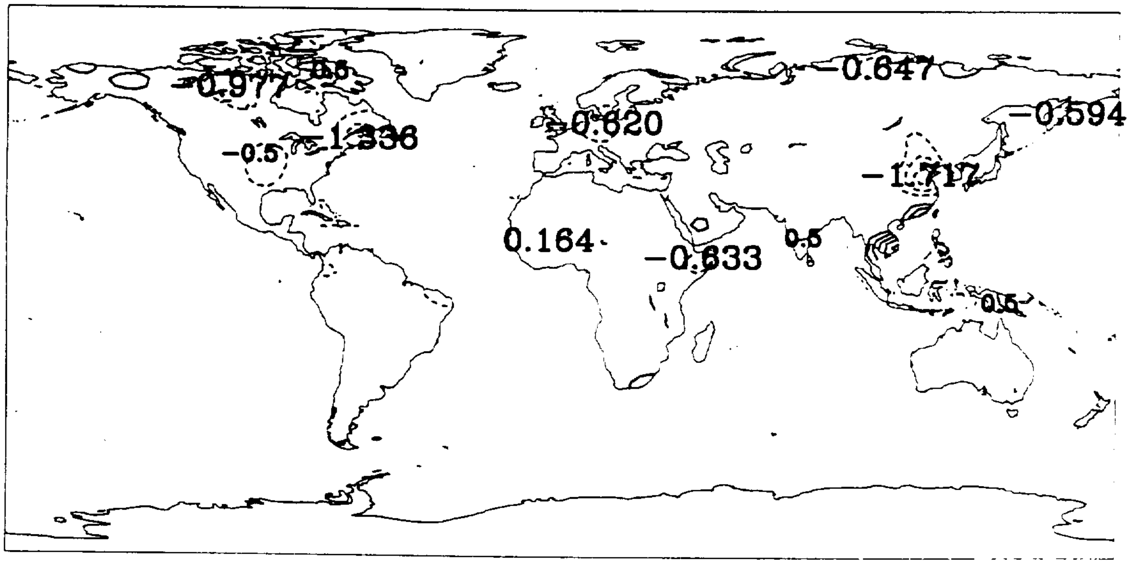

Figure A.3.c Seasonal runoff fields (mm/day) of Run G–2 (presented as [(G–2) – Control])

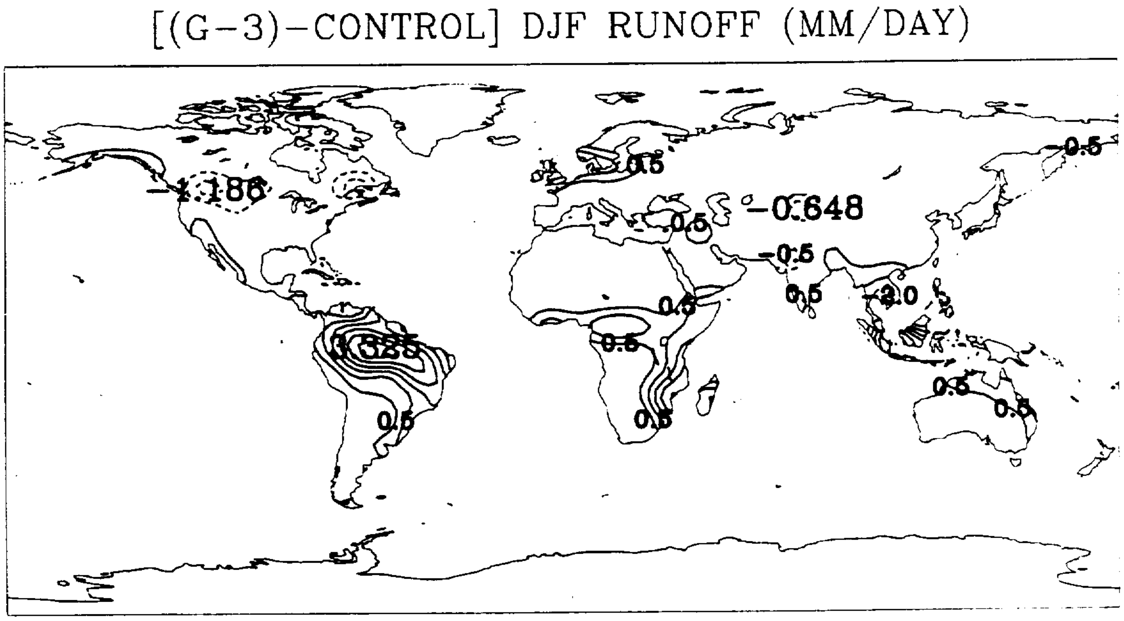

[(G−3)−CONTROL] DJF RUNOFF (MM/DAY)

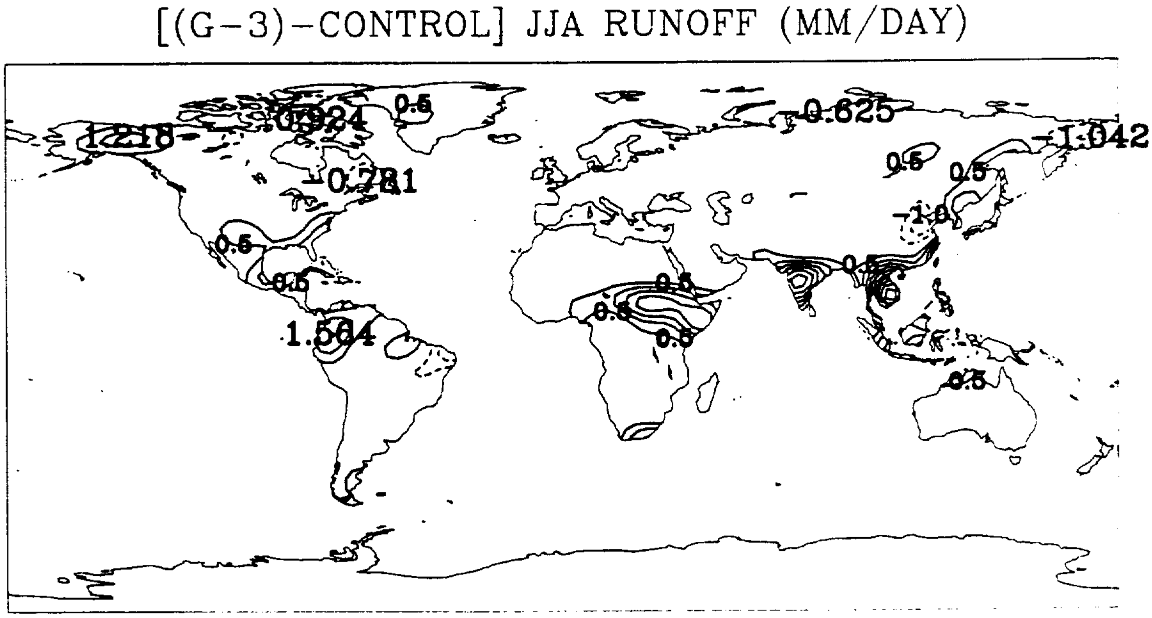

[(G−3)−CONTROL] JJA RUNOFF (MM/DAY)

Figure A.3.d Seasonal runoff fields (mm/day) of Run G–3 (presented as [(G–3) – Control])

CONTROL DJF RELATIVE SURF SOIL MOISTURE (%)

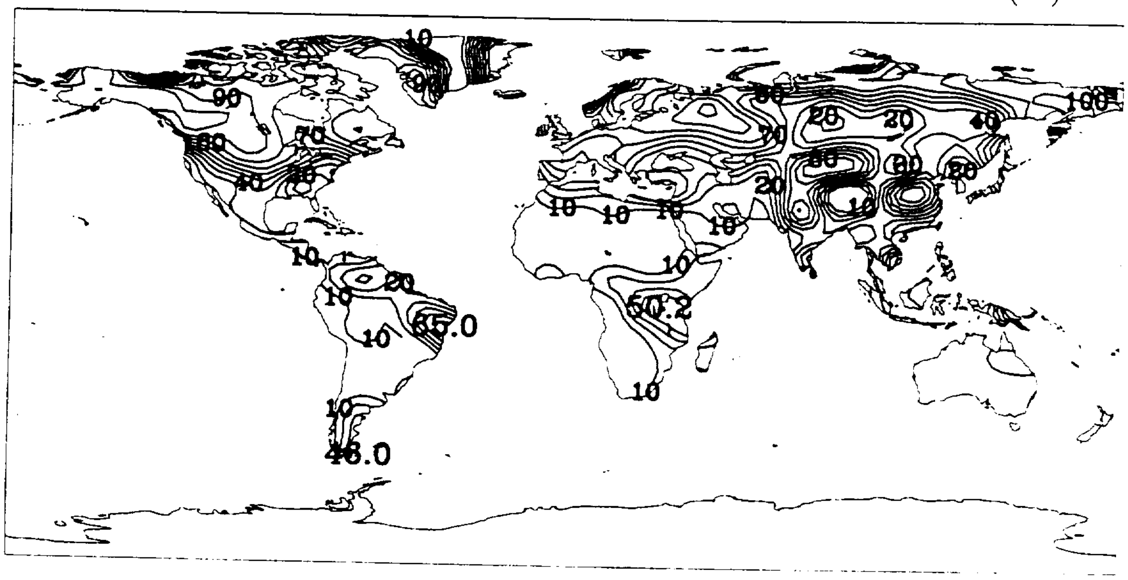

CONTROL JJA RELATIVE SURF SOIL MOISTURE (%)

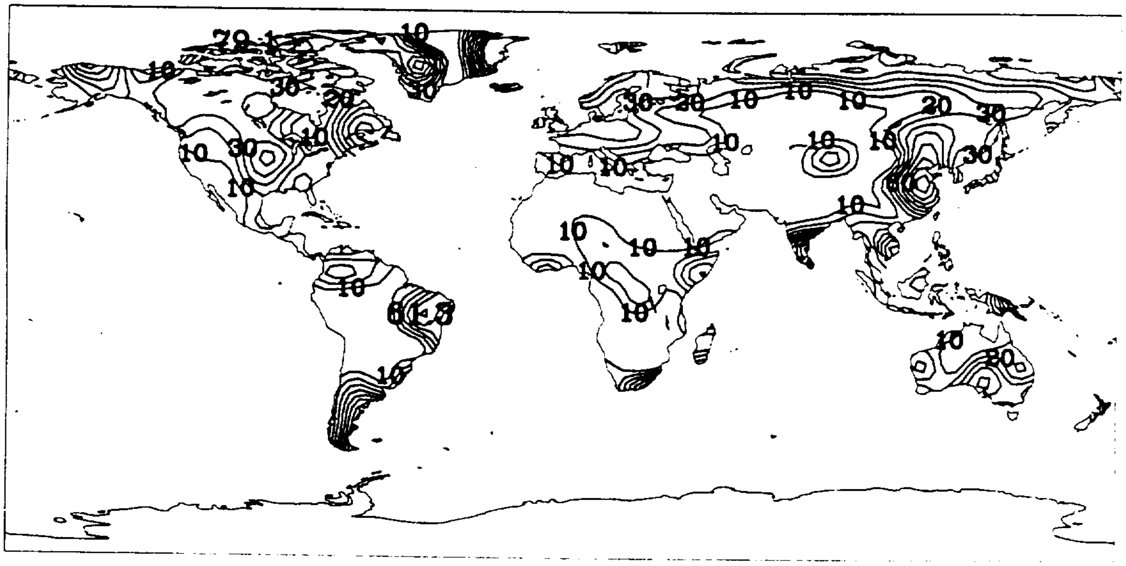

Figure A.4.a Seasonal relative surface soil moisture fields (%) of Control Run (G–0)

[(G-1)-CONTROL] DJF SOIL MOISTURE (%)

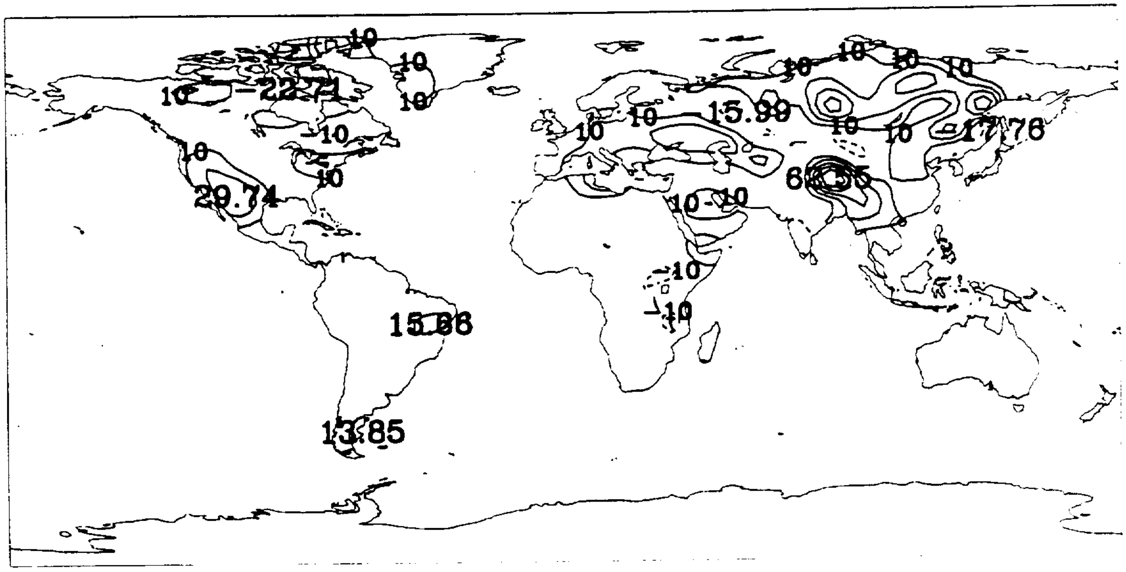

[(G-1)-CONTROL] JJA SOIL MOISTURE (%)

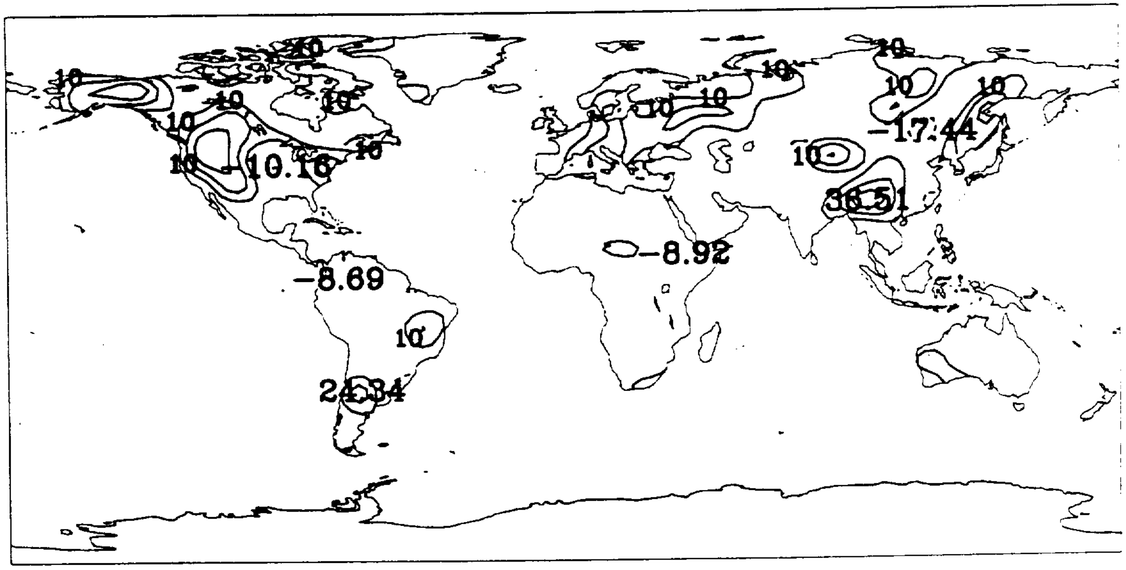

Figure A.4.b Seasonal relative surface soil moisture fields (%) of Run G-1 (presented as [(G-1)- Control])

[(G-2)-CONTROL] DJF SOIL MOISTURE (%)

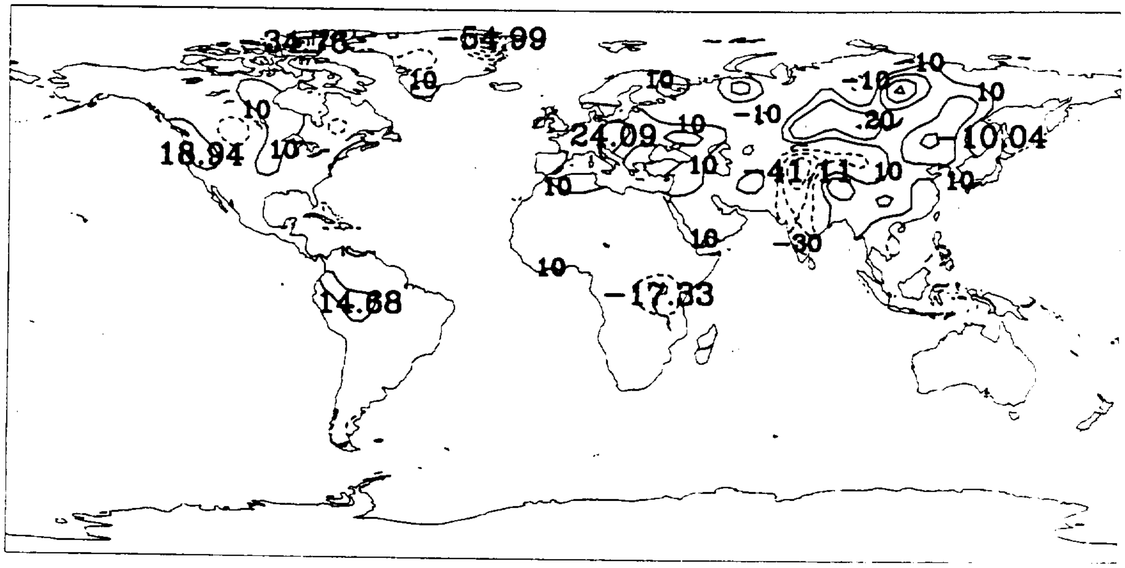

[(G-2)-CONTROL] JJA SOIL MOISTURE (%)

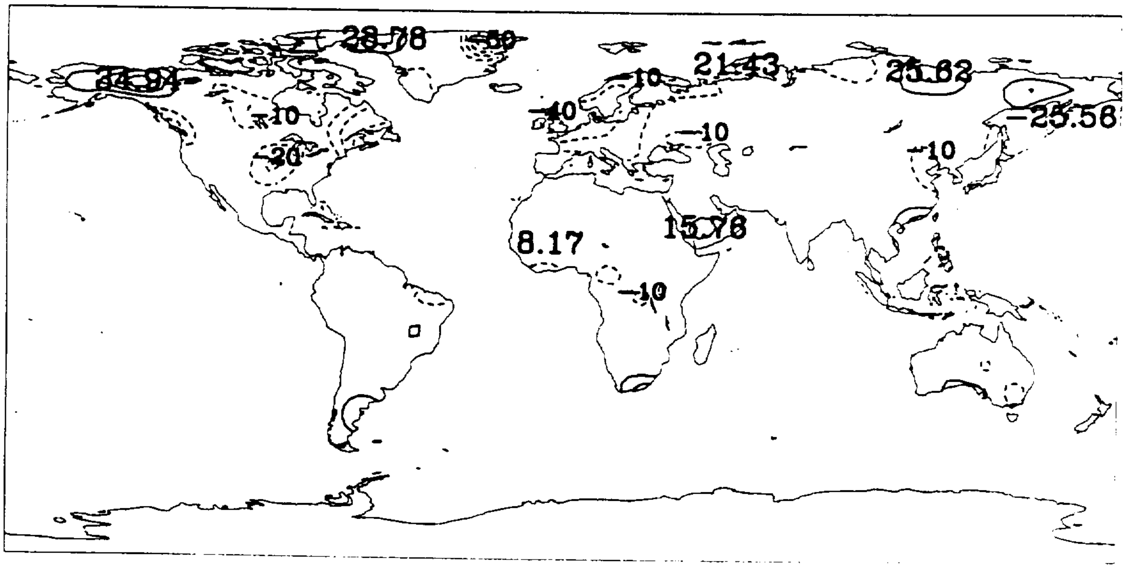

Figure A.4.c Seasonal relative surface soil moisture fields (%) of Run G–2 (presented as [(G–2)– Control])

[(G-3)-CONTROL] DJF SOIL MOISTURE (%)

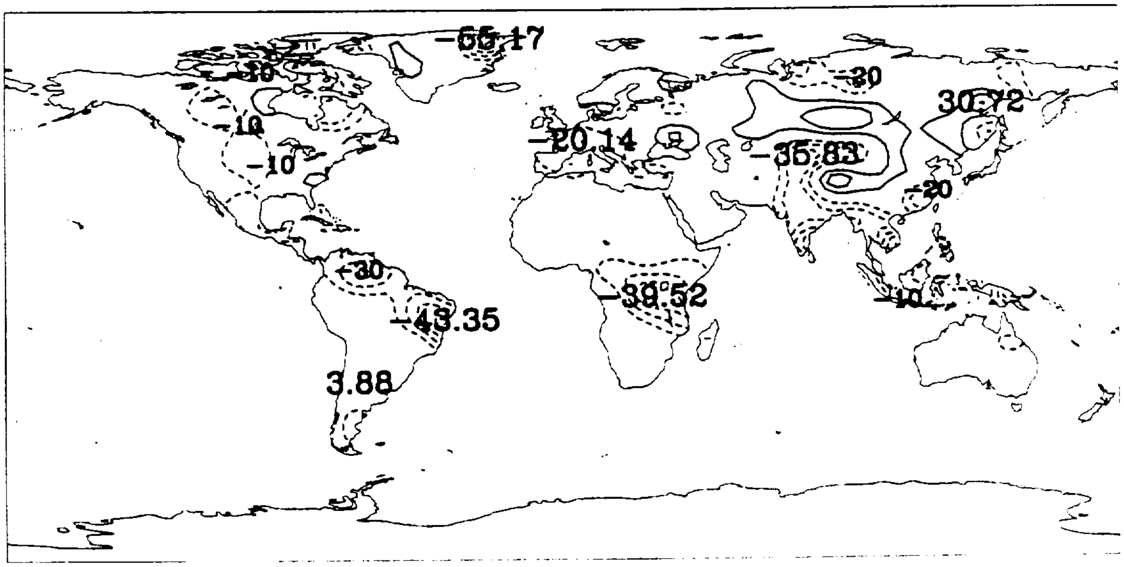

[(G-3)-CONTROL] JJA SOIL MOISTURE (%)

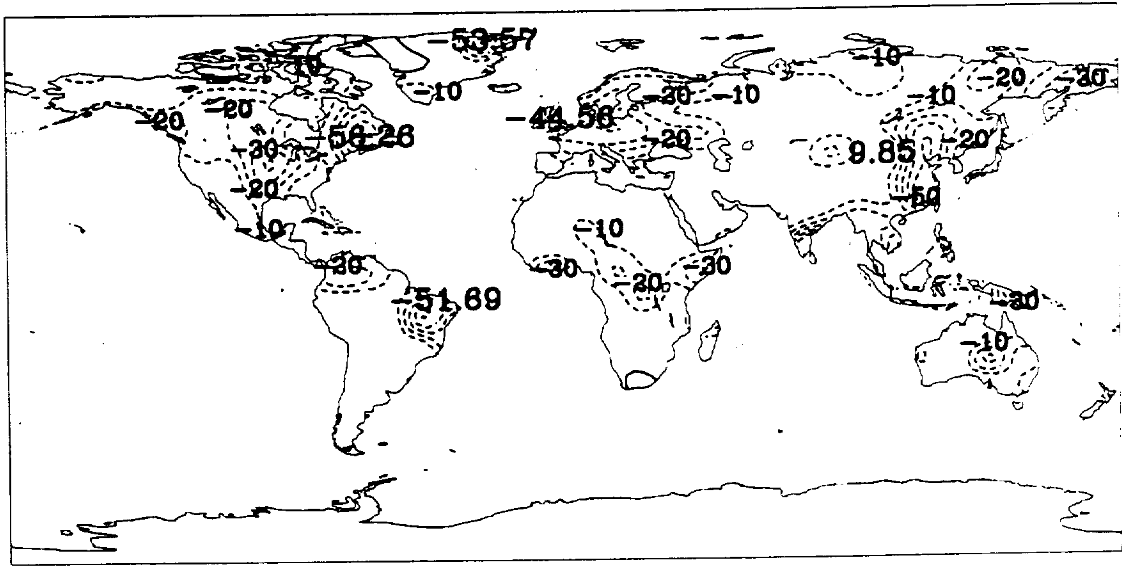

Figure A.4.d Seasonal relative surface soil moisture fields (%) of Run G–3 (presented as [(G–3)– Control])

CONTROL DJF SURFACE AIR TEMP (C)

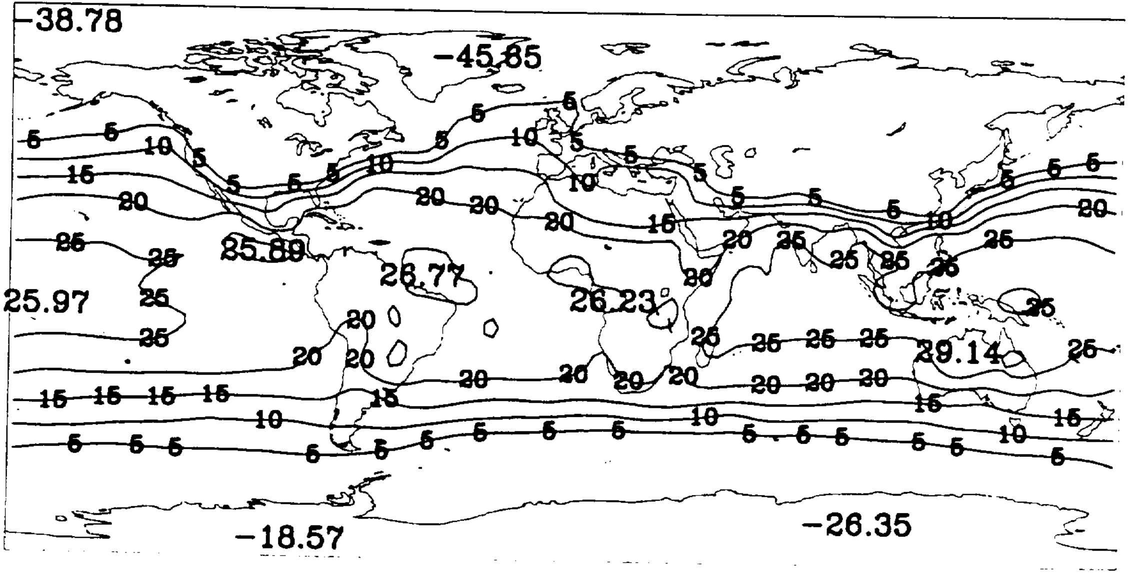

CONTROL JJA SURFACE AIR TEMP (C)

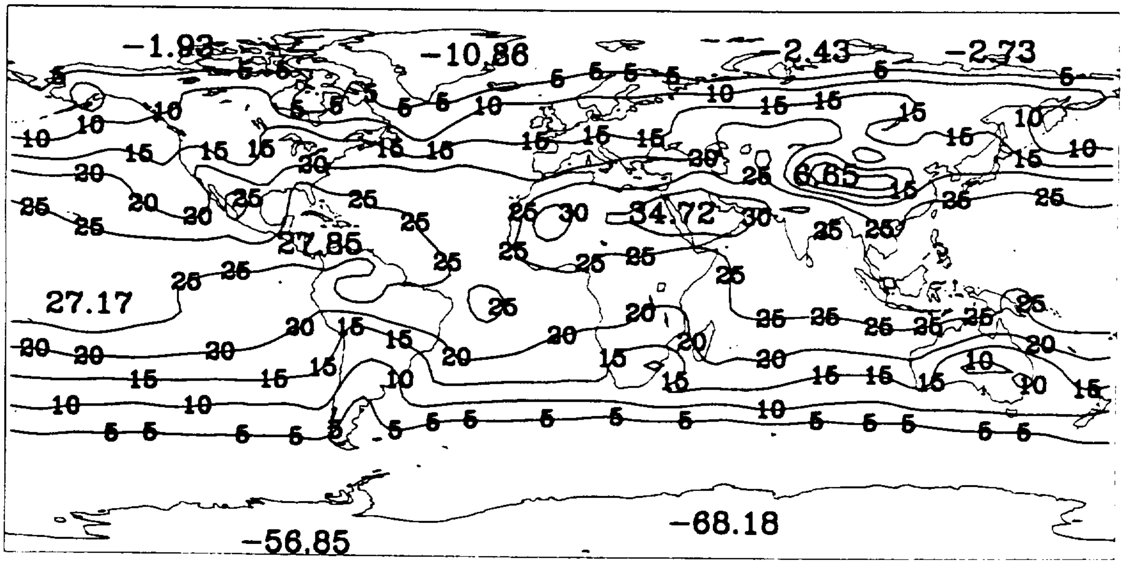

Figure A.5.a Seasonal surface air temperature fields (C) of Control Run (G–0)

[(G−1)−CONTROL] DJF SURFACE AIR TEMP (C)

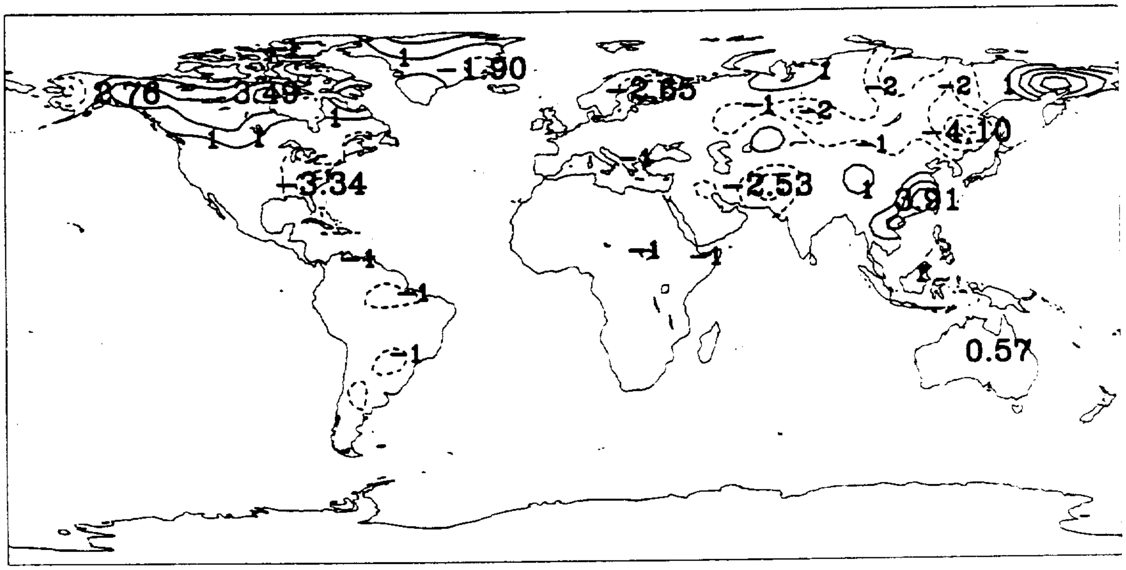

[(G−1)−CONTROL] JJA SURFACE AIR TEMP (C)

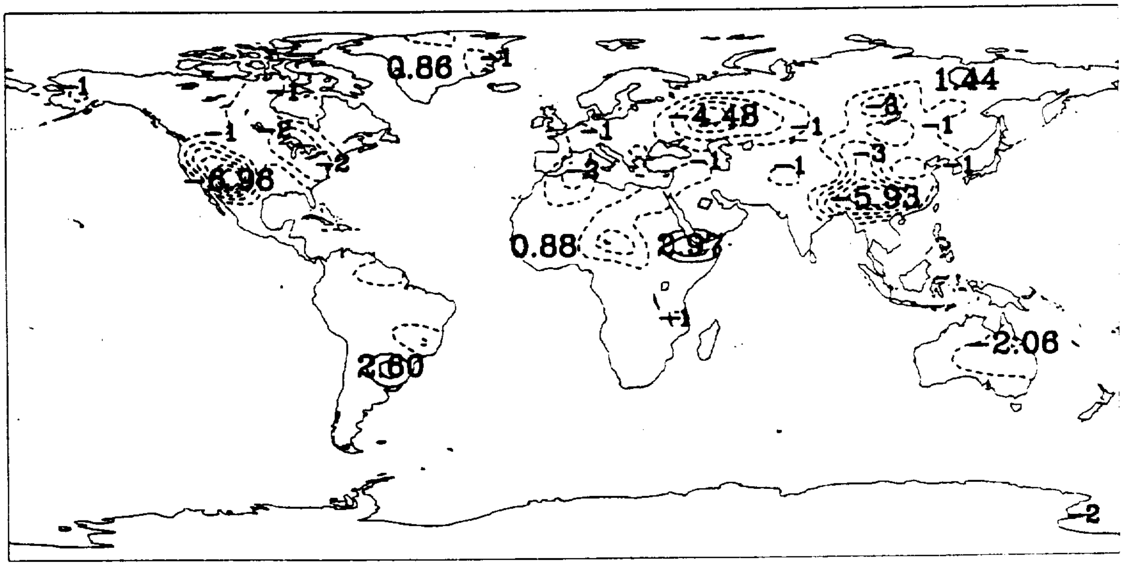

Figure A.5.b Seasonal surface air temperature fields (C) of Run G–1 (presented as [(G–1) – Control])

[(G−2)−CONTROL] DJF SURFACE AIR TEMP (C)

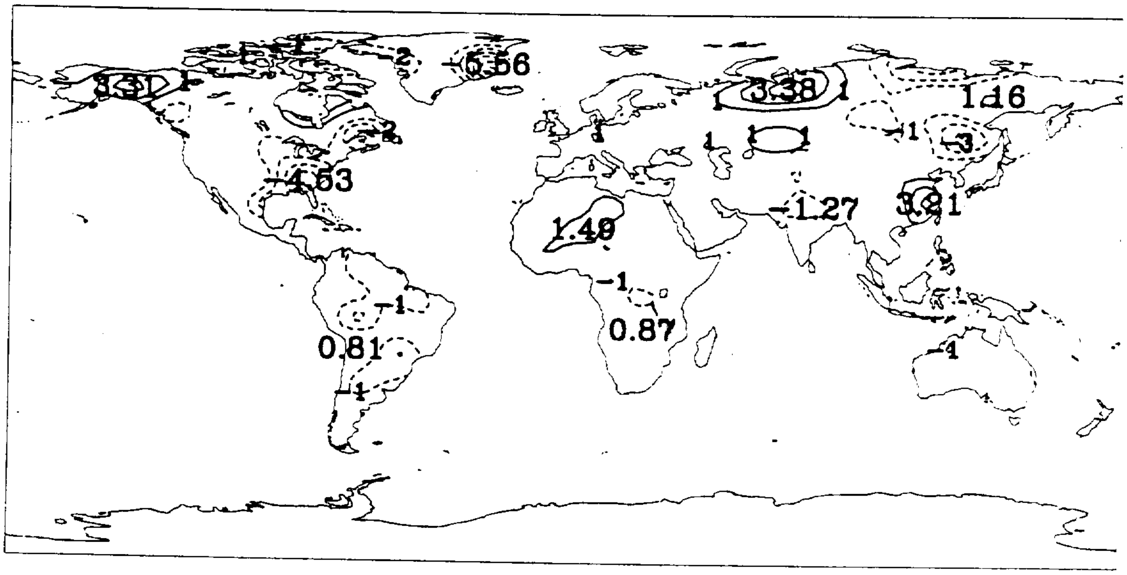

[(G−2)−CONTROL] JJA SURFACE AIR TEMP (C)

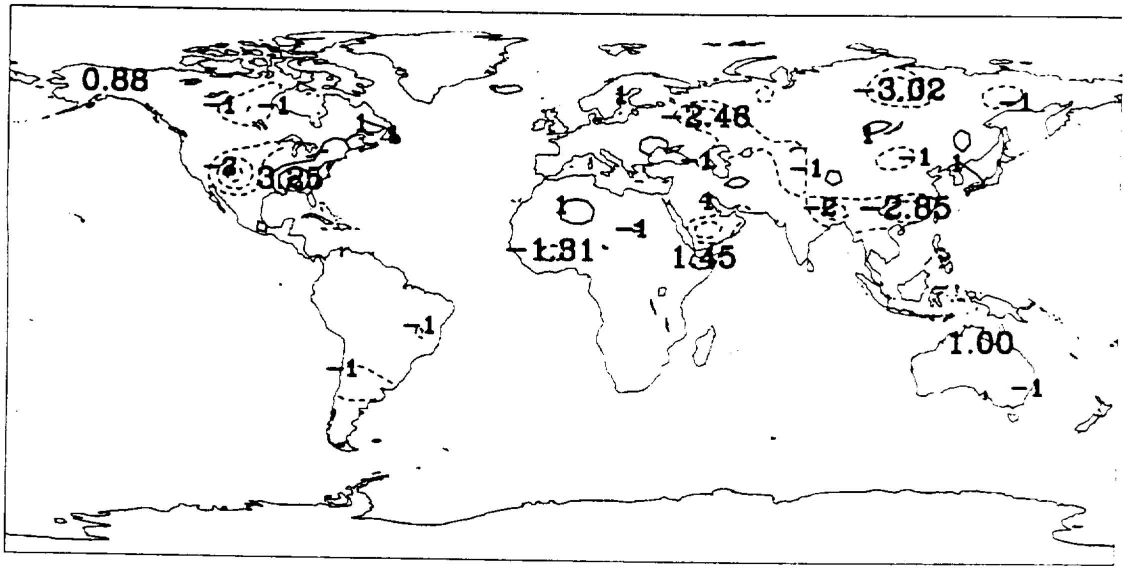

Figure A.5.c Seasonal surface air temperature fields (C) of Run G–2 (presented as [(G–2) – Control])

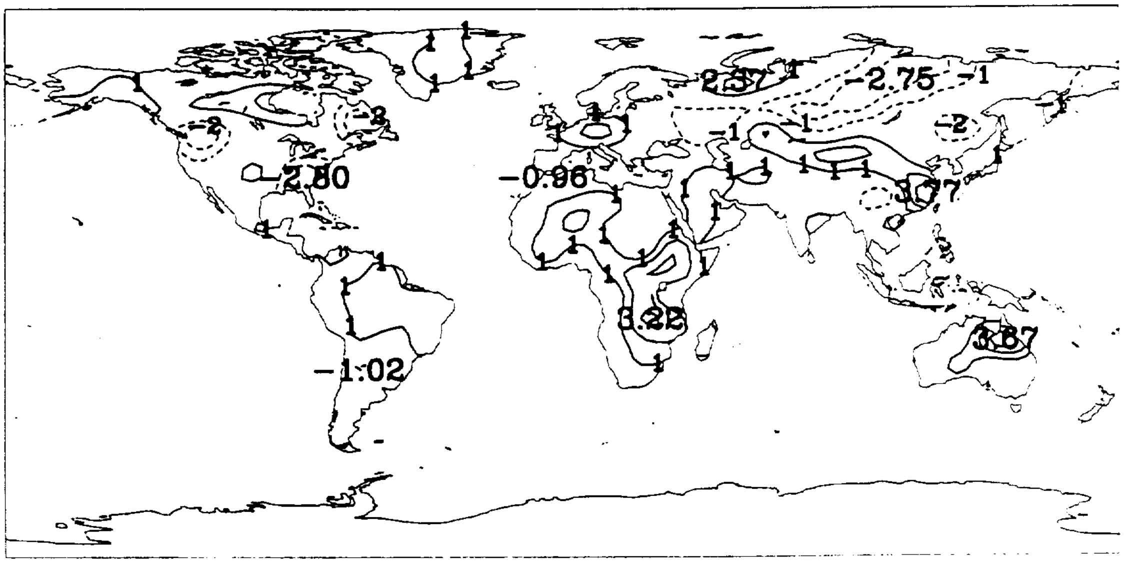
[(G-3)-CONTROL] DJF SURFACE AIR TEMP (C)

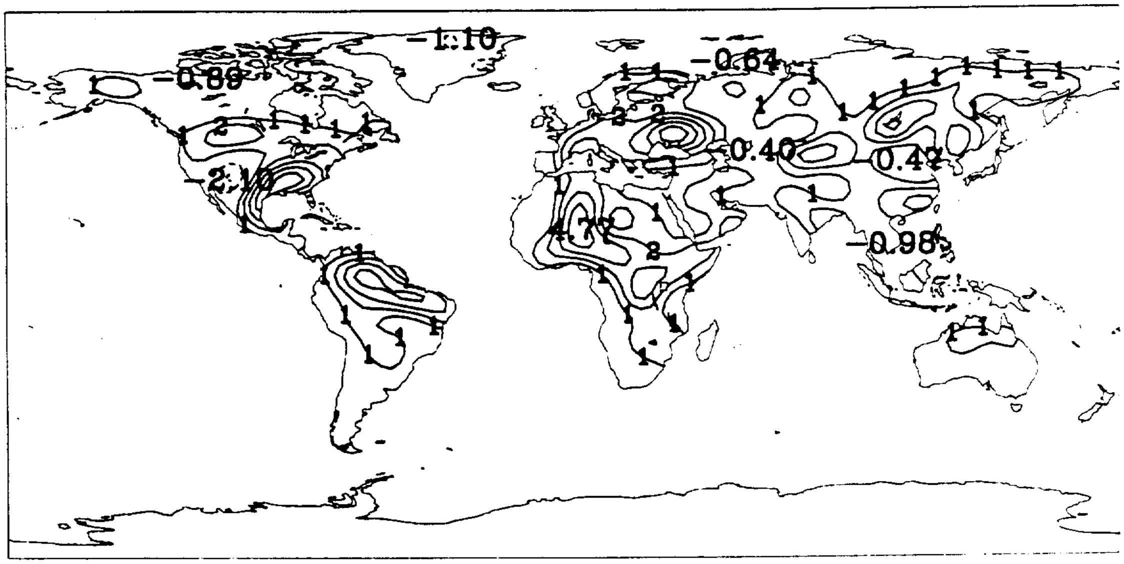
[(G-3)-CONTROL] JJA SURFACE AIR TEMP (C)

Figure A.5.d Seasonal surface air temperature fields (C) of Run G-3 (presented as [(G-3) - Control])

CONTROL DJF POTENTIAL EVAP (MM/DAY)

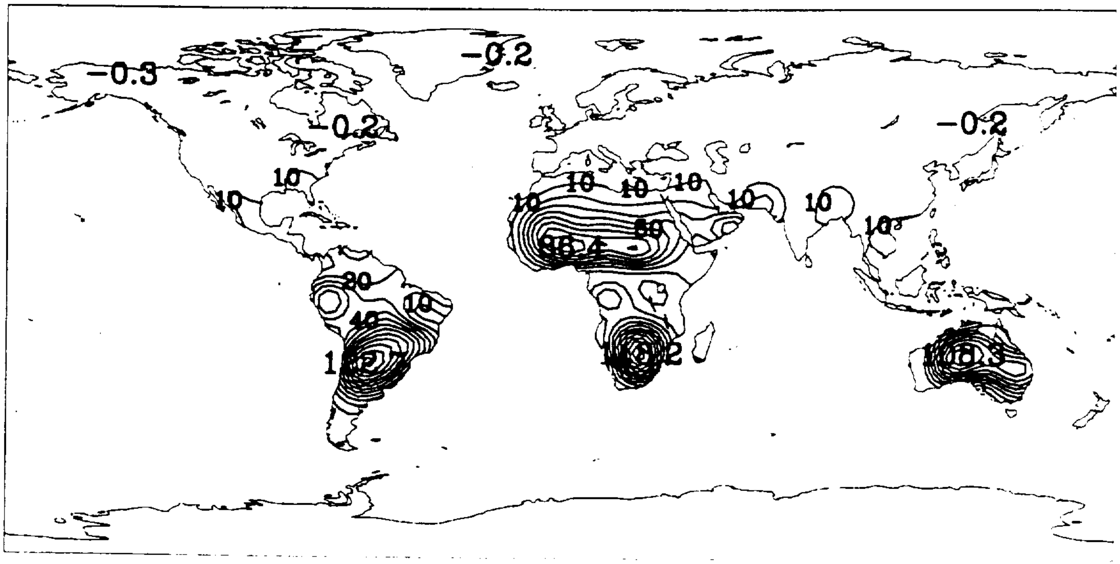

CONTROL JJA POTENTIAL EVAP (MM/DAY)

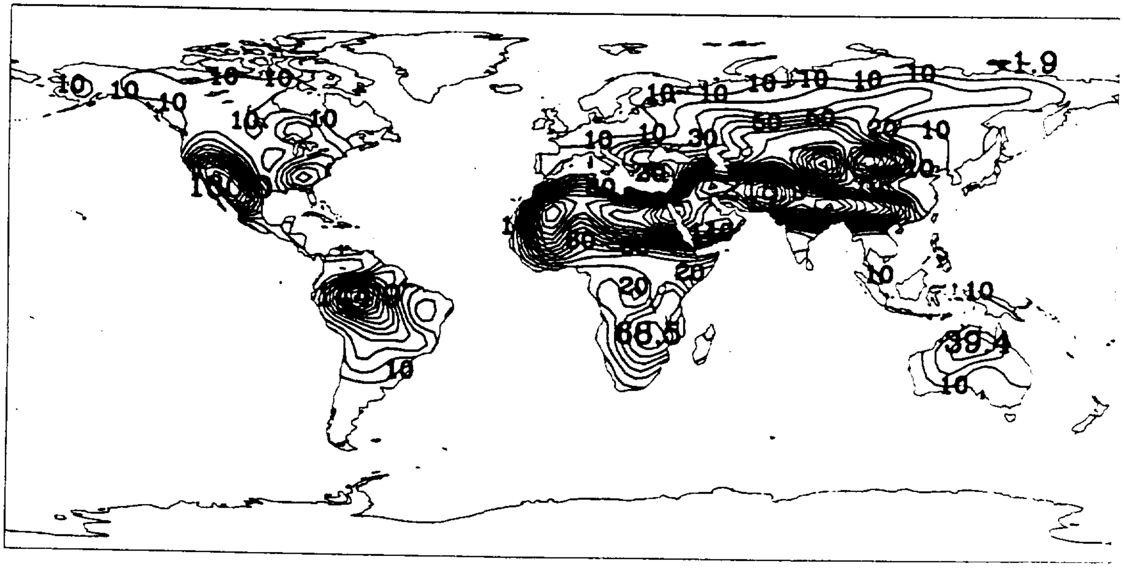

Figure A.6.a Seasonal potential evaporation fields (mm/day) of Control Run (G–0)

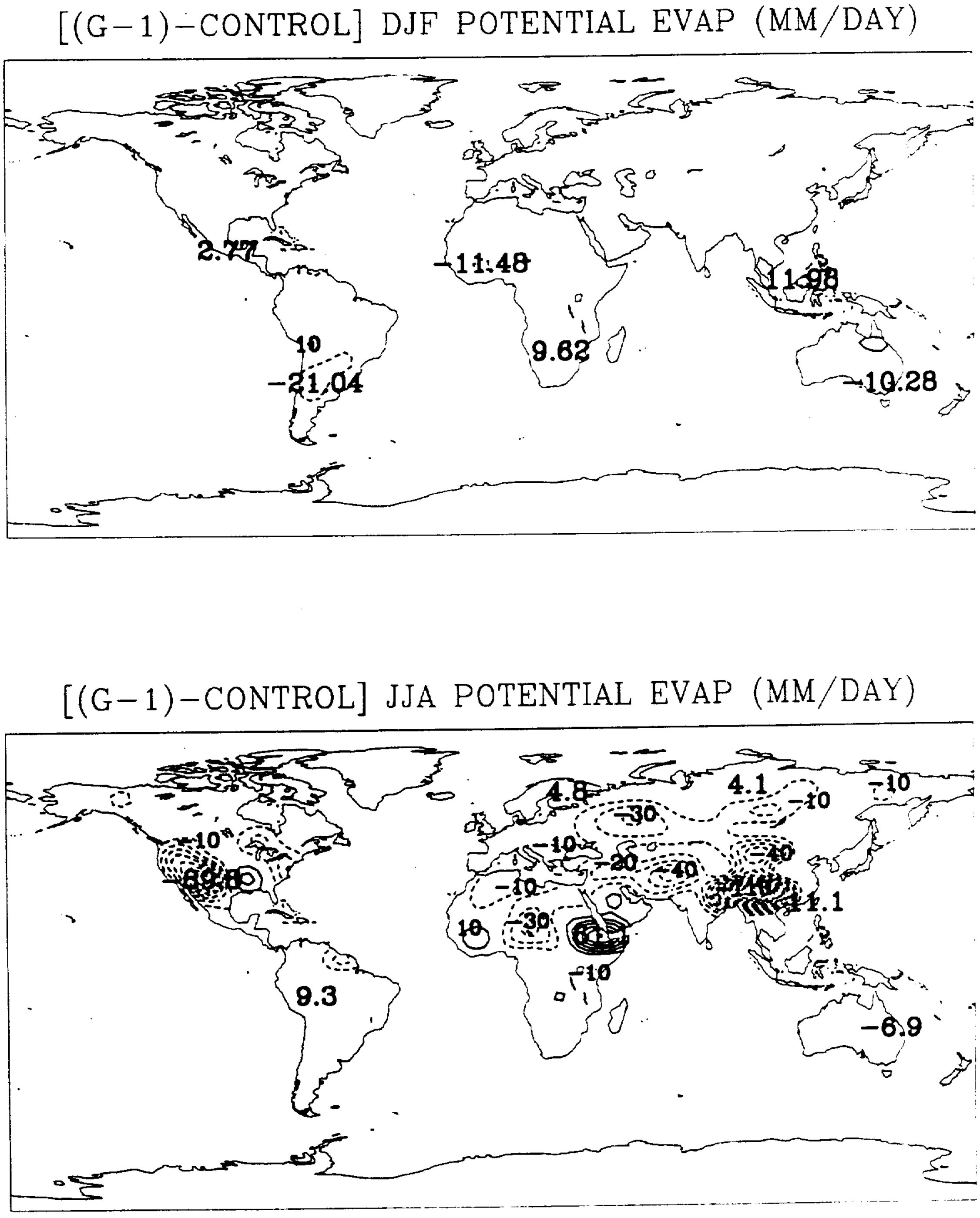
[(G−1)−CONTROL] DJF POTENTIAL EVAP (MM/DAY)

[(G−1)−CONTROL] JJA POTENTIAL EVAP (MM/DAY)

Figure A.6.b Seasonal potential evaporation fields (mm/day) of Run G–1 (presented as [(G–1) – Control])

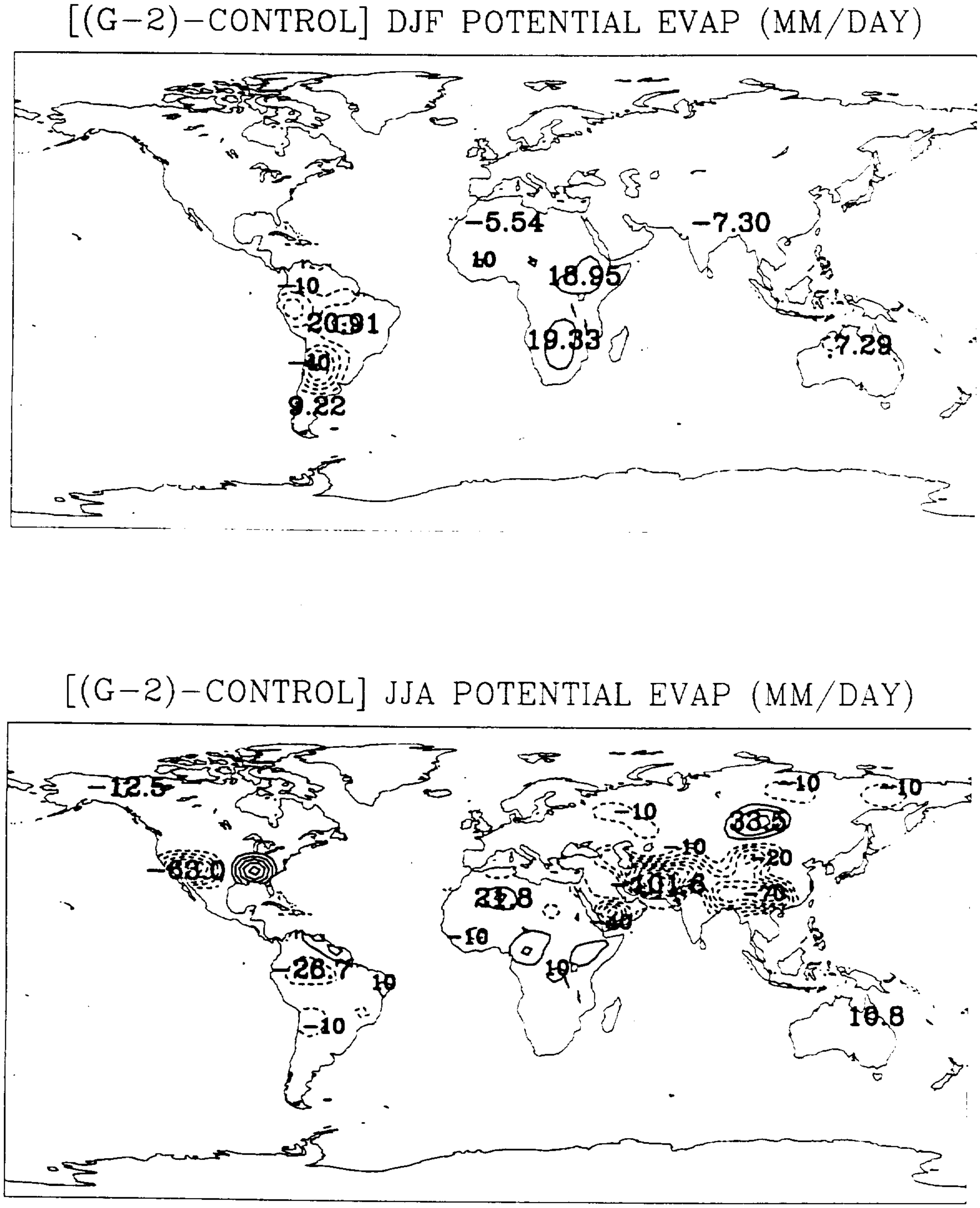

Figure A.6.c Seasonal potential evaporation fields (mm/day) of Run G–2 (presented as [(G–2) – Control])

[(G-3)-CONTROL] DJF POTENTIAL EVAP (MM/DAY)

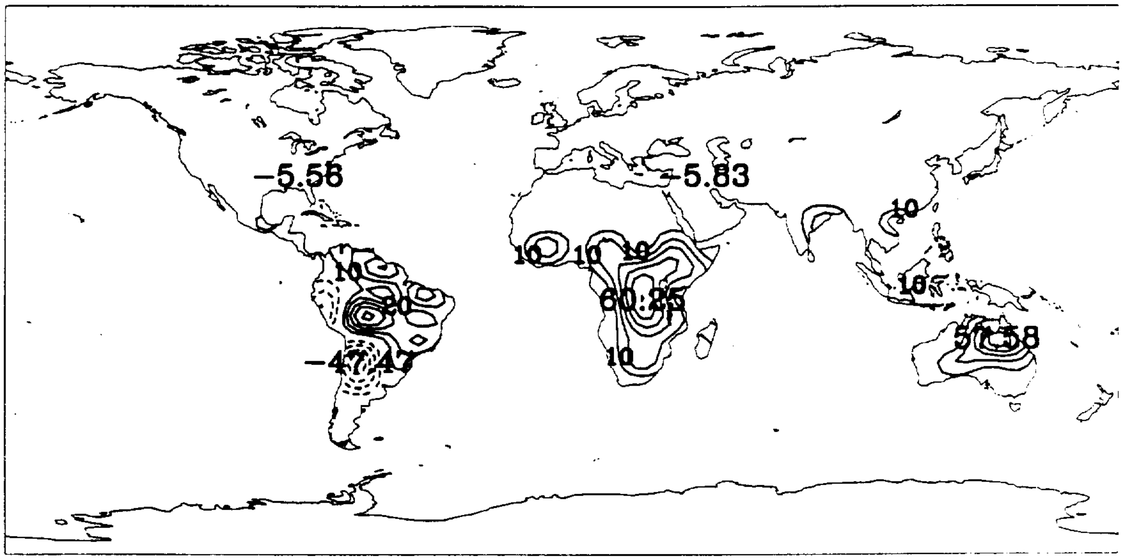

[(G-3)-CONTROL] JJA POTENTIAL EVAP (MM/DAY)

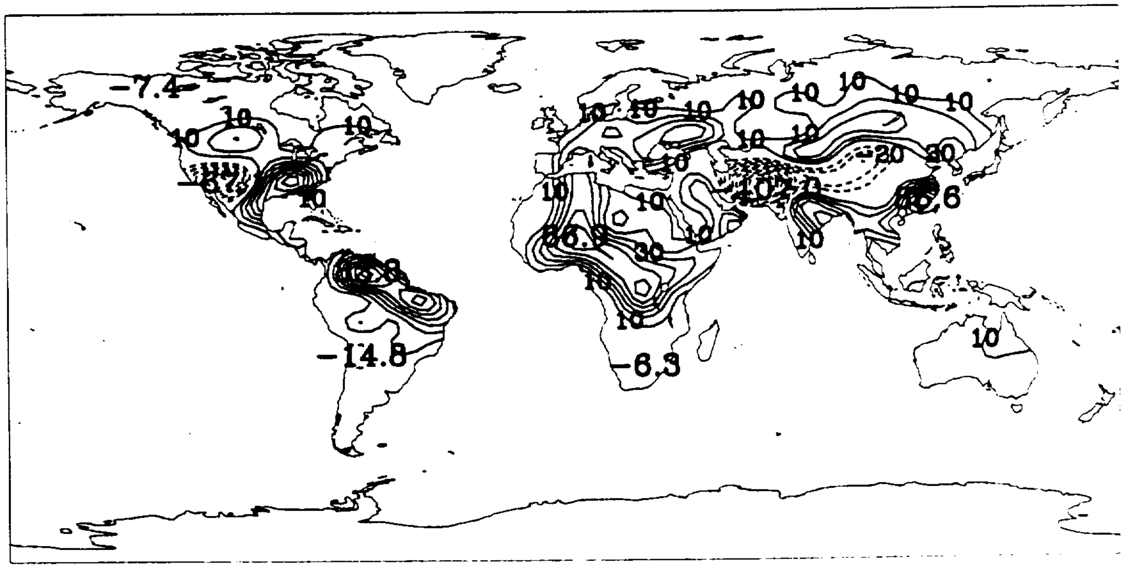

Figure A.6.d Seasonal potential evaporation fields (mm/day) of Run G-3 (presented as [(G-3) - Control])